Inaugural dissertation

for

obtaining the doctoral degree

of the

Combined Faculty of Mathematics, Engineering and Natural Sciences

of the

Ruprecht - Karls - University

Heidelberg

Presented by

M.Sc. Mirian Concepción Fernández Vaquero

born in: Ibiza, Spain 31st of August 1994

Oral examination: 29th of June 2023

Deciphering the role of mutant-*IDH1* in liver cancer development and the tumor immune microenvironment

Referees: Prof. Dr. Peter Angel
Prof. Dr. Mathias Heikenwälder

Table of contents

1 Abbreviations

2D	Two-dimensional
2-HG	2-Hydroxyglutarate
3D	Three.dimensional
ALP	Alkaline Phosphatase
ALT	Alanine aminotransferase
AML	Acute myeloid leukemia
APC	Antigen-presenting cells
ARID	AT-rich interactive domain-containing protein
AST	Aspartate Transaminase
ATM	Ataxia telangiectasia mutated
BAP1	BRCA1 associated protein-1
BECs	Biliary epithelial cells
BiTE	Bispecific T cell engager
BRCA1	Breast cancer gene 1
BRCA2	Breast cancer gene 2
CAFs	Cancer associated fibroblasts
CCA	Cholangiocarcinoma
CCl_4	Carbon tetrachloride
CCND1	Cyclin D1
CD	Cluster of differentiation
CDKN2A	Cyclin-dependent kinase inhibitor 2A
CK18	Cytokeratin 18
CK19	Cytokeratin 19
CO_2	Carbon dioxide
CTCF	Connective tissue growth factor
CTL	Cytotoxic T lymphocytes
CTLA-4	Cytotoxic T-lymphocyte-associated antigen 4
CTNNB1	Catenin beta-1
CXCL12	C-X-C motif chemokine 12

CXCL2	Chemokine (C-X-C motif) ligand 2
DAPI	4′,6-diamidino-2-phenylindole
dCCA	Distal cholangiocarcinoma
DCs	Dendritic cells
DDR	DNA damage response
DEN	Diethylnitrosamine
DMN	Dimethylnitrosamine
DNA	Deoxyribonucleic acid
eCCA	Extrahepatic cholangiocarcinoma
EMT	Epithelial-mesenchymal transition
ECM	Extracellular matrix
EGFR	Epidermal growth factor receptor
FDA	Food and Drug Administration
FGFR2	Fibroblast growth factor receptor 2
GEMMs	Genetically engineered mouse models
GFP	Green Fluorescent Protein
GSH	Glutathion
HA	Hemagglutinin
HBV	Hepatitis B Virus
HCC	Hepatocellular carcinoma
HCV	Hepatitis C Virus
HDACs	Histone deacetylases
H&E	Hematoxylin and eosin
HIF-1α	Hypoxia-inducible factor 1-alpha
HNF4α	Hepatocyte nuclear factor 4 alpha
HSCs	Hepatic stellate cells
HTVi	Hydrodynamic tail vein injection
iCCA	Intrahepatic cholangiocarcinoma
IDH	Isocitrate dehydrogenase
IG	Intraductal growing
IL	Interleukin

INF	Interferon
IRES	Internal Ribosome entry site
JAK-STAT3	Janus kinase-signal transducer and activator of transcription
KRAS	Kirsten Rat Sarcoma virus
LIP	Lipase
LSEC	Liver sinusoidal endothelial cell
MDSC	Myeloid-derived suppressor cell
MF	Mass-forming
MHCII	Major histocompatibility complex class II
miRNA	Micro-RNA
MMPs	Matrix metalloproteases
MYC	Myelocytomatosis proto-oncogene
myr-AKT	Myristoylated AKT
$NADP^+$	Nicotinamide adenine dinucleotide phosphate-oxidized
NADPH	Nicotinamide adenine dinucleotide phosphate-reduced
NICD1	Notch1 Intracellular Domain
NK	Natural killer
NRAS	Neuroblastoma RAS viral oncogene homolog
O_2	Oxygen
OS	Overall survival
OVA	Ovalbumin
PBRM1	Polybromo 1
PCA	Principal component analysis
pCCA	Perihilar cholangiocarcinoma
PCR	Polymerase chain reaction
PD-1	Programmed cell death protein 1
PD-L1	Programmed cell death-ligand 1
PI	Periductal infiltrating
PIK3CA	Phosphatidylinositol-4,5-biphosphate 3-kinase catalytic subunit alpha
PLC	Primary liver cancer
PSC	Primary sclerosing cholangitis

PTEN	Phosphatase and tensin homolog deleted
RNA	Ribonucleic acid
ROBO1	Roundabout homolog 1
ROBO2	Roundabout homolog 2
ROS	Reactive oxygen species
SB	Sleeping Beauty
SEM	Standard error of the mean
sgRNA	single guide RNA
SIRPα	Signal regulatory protein-α
SMAD4	Suppressor of mothers against decapentaplegic 4
SOCS-3	Suppressor of cytokine signaling 3
SPCS1	Signal peptidase complex subunit 1
TAA	Thioacetamine
TAM	Tumor-associated macrophage
TAN	Tumor-associated neutrophils
TCA	Tricarboxylic acid cycle
TERT	Telomerase reverse transcriptase
TES	Targeted-exome sequencing
TET	Ten-eleven translocation
TGF-β1	Transforming growth factor β1
TIL	Tumor-infiltrating lymphocytes
TIME	Tumor immune microenvironment
TNF	Tumor necrosis factor
TP53	Tumor suppressor p53
T_{reg}	Regulatory T cell
UMAP	Uniform Manifold Approximation and Projection
UPLC-MS	Ultra performance liquid chromatrography-mass spectometry
VEGF	Vascular endothelial growth factor
WES	Whole-exome sequencing
YAP	Yes-associated protein
α-KG	alpha-ketoglutarate

2 Summary

Primary liver cancer (PLC) is among the five deadliest cancers worldwide, which represents a clinical challenge to the global health system[1]. Anatomically arising from a regenerative organ with high capacity for plasticity as the liver, hepatocellular carcinoma (HCC) and intrahepatic cholangiocarcinoma (iCCA) are the most frequent types of PLC. Although iCCA represents just 10-20% of liver tumors, the rise in its incidence in the past decades urges to develop new strategies that facilitate patient stratification and offer the best particular therapies and outcomes[2]. Due to the limited treatment options and the considerable heterogeneity that this malignancy displays on distinct levels, integrative analyses have been key to identify targetable alterations that may improve the clinical management of this disease. Notably, gain-of-function mutations in the *IDH1* gene, which lead to the accumulation of the oncometabolite 2-HG, have been commonly reported in 15-20% of iCCA cases[3]. Mutant-*IDH1* plays a pivotal role in the deregulation of homeostatic processes, strongly affecting the tumor immune microenvironment (TIME) and promoting cancer development. Nevertheless, further research is needed to decipher the intra-tumor heterogeneity and the molecular underpinnings by which mutant-*IDH1* enhances cholangiocarcinogenesis.

To investigate the role of mutant-*IDH1* in the liver microenvironment, I established an *in vivo* mouse model for liver cancer based on the hydrodynamic tail vein injection (HTVi) of DNA vectors. This model recapitulated the biological function of mutant-*IDH1* and led to an increase in liver 2-HG content. Next, I investigated the molecular heterogeneity of iCCA by delivering mutant-*IDH1* in combination with single genetic alterations frequently found in iCCA. I determined that by using this method, mutant-*IDH1* is not a driver but rather an enhancer of tumor initiation. In addition, to define the impact of *IDH1* mutations in the iCCA tumor immune microenvironment (TIME), I combined it with established iCCA-drivers. By using transcriptomic analysis, immunohistochemistry and multiparametric spectral flow cytometry analysis, I determined that *IDH1 R132C* in particular, accelerates tumor initiation, promotes metastatic invasion to extrahepatic tissue and remodels the iCCA TIME in the context of *KRAS/p53*. Moreover, co-culture systems revealed that *IDH1 R132C* plays a pivotal role by recruiting myeloid cells with immunosuppressive features, affecting T cell polarization and thereby potentially contributing to tumor progression. Further, I identified SIRPα, considered an immune checkpoint molecule, expressed on myeloid cells which infiltration is significantly increased in the *KRAS/p53/IDH1 R132C* TIME. Despite the need for further research to define the molecular underpinnings, my data suggests SIRPα as a novel target for the treatment of mutant-*IDH1* iCCA.

3 Zusammenfassung

Das primäre Leberzellkarzinom gehört zu den 5 tödlichsten Arten von Krebs weltweit und stellt eine klinische Herausforderung für das globale Gesundheitssystem dar. Durch ihre Enstehung in der Leber, welches als regeneratives und hochplastisches Organ gilt, sind das hepatozelluläre Karzinom (HCC) und das intrahepatische Cholangiokarzinom (iCCA) die häufigsten Formen des primären Leberzellkarzinoms. Obwohl das iCCA nur 10-20% von Lebertumoren ausmacht, drängt die gestiegene Inzidenz in den vergangenen Jahrzenten zu einer Entwicklung neuer Strategien, welche die Patienten Stratifizierung erleichtern und die Belastung vermindern. Aufgrund limitierter Behandlungsoptionen und ausgeprägter Heterogenität, die diese Krankheit auf vielfältige Weise aufweist, waren integrative Analysen maßgeblich entscheidend um Veränderungen zu identifizieren, welche als Behandlungsziel gelten können, und so die Klinische Behandlung verbessern. Gain-of-function Mutationen im *IDH1* Gen, die zur Anreicherung des Onkometabolits 2-HG führen, wurden in 15-20% von iCCA Patienten berichtet. Ein mutiertes *IDH1*-Gen spielt eine wichtige Rolle in der Deregulierung von homeostatischen Prozessen, welche das immunologische Tumormikromilieu beeinflusst und die Krebsentstehung vorantreibt. Nichtsdestotrotz ist eine tiefergehende Erforschung der Heterogenität innerhalb von Tumoren und der molekularen Grundlagen nötig, um zu verstehen wie ein mutiertes *IDH1*-Gen die Cholangiokarzinogenese verstärkt.

Um die Rolle des mutierten IDH1-Gens innerhalb des Lebermikromilieus zu untersuchen, habe ich in-vivo Mausmodelle etabliert, welche auf der hydrodynamischen Schwanzveneninjektion von DNA-Vektoren basieren. Trotz einiger Limitationen dieses Ansatzes, rekapitulierte dieses Versuchsmodell die biologische Funktion des mutierten *IDH1*-Gens und führte zu einer Erhöhung der 2-HG Konzentration in der Leber. Als nächstes untersuchte ich die molekulare Heterogenität des iCCA, indem ich das mutierte *IDH1*- Gen in Kombination mit zusätzlichen genetischen Veränderungen applizierte, welche häufig im iCCA gefunden werden. Durch diesen Ansatz habe ich festgestellt, dass ein mutiertes *IDH1*-Gen nicht der Treiber, sondern vielmehr ein Verstärker der Tumorentstehung ist. Außerdem kombinierte ich etablierte Treiber-Mutationen des iCCAs, um den Einfluss von *IDH1* Mutationen auf das immunologische Tumormikromilieu zu bestimmen. Durch Transkriptionsanalysen, Immunhistochemie und hochparametrische spektrale Durchflusszytometrie stellte ich fest, dass *IDH1 R132C* die Tumorentstehung beschleunigt, die Invasion in extrahepatisches Gewebe fördert und das immunologische Tumormikromilieu des iCCAs im Kontext von *KRAS/p53* umgestaltet. Ko-Kultursysteme zeigten, dass *IDH1 R132C*

dabei eine zentrale Rolle spielt, indem es myeloide Zellen mit immunsuppressiven Eigenschaften rekrutiert, die T-Zell-Polarisation beeinflusst und so möglicherweise zur Tumorprogression beitragen kann. Darüber hinaus identifizierte ich SIRPα als ein Immun-Checkpoint-Molekül, das auf myeloiden Zellen exprimiert wird, deren Infiltration innerhalb der immunologischen Mikroumgebung im Kontext von *KRAS/p53/IDH1 R132Cs* signifikant erhöht ist. Obwohl weitere Forschung notwendig ist, um die molekularen Mechanismen zu bestimmen, deuten meine Daten darauf hin, dass SIRPα ein neuartiges Ziel für die Behandlung von mutiertem-*IDH1* bei iCCA darstellen könnte.

4 Introduction

4.1 The liver

The liver is the largest solid, internal organ of the human body that together with the pancreas, gallbladder and gastrointestinal tract, comprises the digestive system. It is considered the master regulator of homeostatic and metabolic processes, including carbohydrate (glycolysis and gluconeogenesis), protein (transformation of ammonium into urea) and fat metabolism (lipolysis and lipoprotein synthesis). Responsible for bile secretion, involved in the absorption and digestion of lipids, the liver also increases the solubility of drugs and harmful substances by filtering them and inactivating them[4].

The liver exhibits an intricate but finely organized network of various cell types that structured in lobules as a functional unit, interact to drive and sustain liver functions. With a highly vascularized architecture, the liver lobules display a hexagonal structure that includes the portal triad (comprising artery, vein and bile duct) and the central vein[5]. This particular spatial organization in the different so-called “zones” is in accordance to the diverse cellular functionality, which correlates with key pathways depending on oxygen and nutrient levels, a phenomenon known as metabolic zonation. Here, the portal space shows the highest level of oxygen which decreases progressively until the central vein[6, 7].

Furthermore, principal parenchymal cells include the hepatocytes that, accounting for 80% of the total liver cells, are considered the major players in metabolic functions and bile secretion, while the cholangiocytes (5% of total hepatic cells), the bile duct epithelial cells, are responsible for transporting bile along the biliary tree to the small intestine. Markedly, both cell types arise from the same bi-potent progenitor cells, the hepatoblasts, that share markers for both hepatocytes (HNF-4α and CK18) and cholangiocytes (CK19)[8]. The regenerative potential of the liver is a key feature that is in part explained by the cellular plasticity of these cells, which are able to transdifferentiate into one another in order to keep under control the tissue homeostasis[9].

In addition, the non-parenchymal component encompasses the liver sinusoidal endothelial cells (LSECs) as well as hepatic stellate cells (HSCs), that when activated, are responsible for collagen production, becoming of special importance in the liver damage response[10]. Also, Kupffer cells are the resident macrophages that localize in the liver sinusoids and are part of the innate immune cells which counteract bacterial infections. Together with other resident and infiltrating immune cells (e.g. lymphocytes including T cells, B cells or natural killer (NK) cells, and myeloid cells such

as monocytes, dendritic cells (DCs) and myeloid derived suppressor cells (MDSCs)), the liver is able to orchestrate an immunological response that can rapidly identify any potential damaging agent such as tumor cells or pathogens[4, 11]. Therefore, although conventionally considered as a tolerant organ on an immunological level, the liver is not only an essential metabolic organ, but it is also key in influencing the immunological microenvironment (Figure 1)[7].

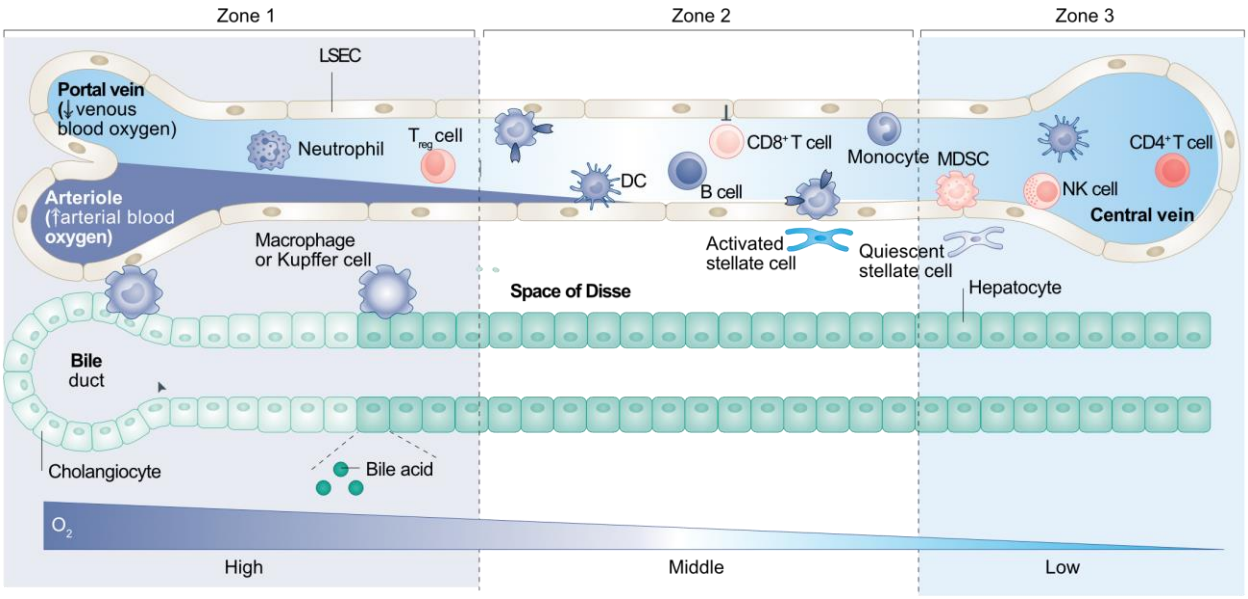

Figure 1. Hepatic spatial distribution and cellular composition. Liver parenchymal cells, including hepatocytes and cholangiocytes, display different functions depending on their location and the microenvironmental cues they are exposed to. The so-called portal triad includes the portal vein, the hepatic artery and the bile duct, which considered as Zone 1, exhibits the highest levels of O_2 (oxygen) and allows most of the metabolic processes to occur. In contrast, Zone 3 with the lowest level of O_2 is rather dedicated to support functions that demand lower energy. In addition, non-parenchymal cells involved in maintaining homeostatic processes, such as LSECs, stellate cells and a broad variety of immune cells also show zonation. This spatial distribution allows the activation of defined signaling pathways that finely regulates homeostatic processes and enables the orchestration of a rapid response against stress conditions such as infections or cancer. Adapted from Li *et al.* 2021[7]

4.2 Primary liver cancer

The liver is continuously exposed to environmental factors (i.e. pathogens or dietary regimens) that have the potential to deregulate homeostatic processes. Consequently, the presence of damaging agents that affect this organ on a chronic manner may ultimately induce the development of liver disease.

According to the GLOBOCAN 2020 database, primary liver cancer (PLC) was among the five most common causes of cancer death globally in 2020, accounting for 8.3% of total number of deaths including both sexes and all ages[1]. Even though more than 75% of liver cancer cases derive from the chronic infection with HBV and HCV, additional risk factors also include aging and sex (males are more prone to develop liver cancer), and external threats such as sedentary lifestyle and unhealthy habits (diet, tobacco and alcohol consumption). Alarmingly, the liver cancer burden is estimated to increase by more than 50% worldwide in the next two decades[12]. This fact threatens the healthcare system and urges for the implementation of control policies that would enhance the prevention of cancer incidence, as well as an understanding of the malignancy that allows the development of precise strategies to tackle such a social hurdle.

In terms of disease stratification, PLC comprises different pathological entities that, although arise from the same organ, diverge not only on a histological but also a prognostic level. The most common tumor type in adults accounting for 80-90% of all cases is hepatocellular carcinoma (HCC). For more than a decade, sorafenib, a multi-kinase inhibitor, was the sole first-line therapy for advanced stages. Recently, identification of key mutational drivers of the disease (i.e. *MYC, TERT, CTNNB1*) as well as the detrimental effect that chronic inflammation plays on the hepatic microenvironment, prompted to combine systemic therapies with immunotherapy, leading to promising results[13, 14]. Despite the increasing efforts in understanding such a complex disease, limited response or resistance mechanisms to current therapies limits HCC patients to a 5-year overall survival (OS) rate of less than 20%[13].

HCC is followed by 10-20% of PLC cases represented by cholangiocarcinoma (CCA), also known as bile duct cancer, which is the focus of the present work and will be discussed in detail. In addition to HCC and CCA, a small percentage of PLC cases comprise rare cancers: combined HCC-CCA tumors (cHCC-CCA), angiosarcoma and hemangiosarcoma, which are mostly derived from the exposure to toxic agents, and hepatoblastoma, the most prevalent type of cancer affecting children[15, 16].

4.3 Cholangiocarcinoma

4.3.1 A clinical challenge

CCA includes a diverse group of neoplasms characterized by their biliary differentiation patterns. Important to note is that gallbladder cancer, although also affecting part of the biliary system, is considered a completely different entity from CCA in terms of clinical presentation and management[17]. Given that the biliary tree connects the liver to the intestine through intra- and extrahepatic bile ducts, the anatomic location is also applied to CCA classification. Consequently, intrahepatic CCA (iCCA) includes the small bile ducts within the liver (hepatic and proximal bile ducts), while the extrahepatic CCA (eCCA) can be sub-divided into perihilar CCA (pCCA), comprising those bile ducts entering the liver, and distal CCA (dCCA) affecting the common bile duct (Figure 2.A)[18]. The most prevalent cancer with 50-60% of the cases is pCCA, followed by dCCA, which accounts for 30-40%. This leaves iCCA as the rarest type with just 10-20% of the cases[2].

CCA is a rare cancer as it presents a global incidence ranging only from 0.3-6 per 100,000 inhabitants. This varies widely across geographies, with the highest burden in East Asia (more than 6 per 100,000 cases) correlating with a higher exposure of infection with liver flukes[2]. Notably, the induction of chronic inflammation of the hepatobiliary system remains as a common feature that promotes CCA development. Frequently, both types of CCA (iCCA and eCCA) can derive under stressed conditions like primary sclerosing cholangitis (PSC) and liver flukes[19]. In contrast, chronic liver diseases in Western countries (viral hepatitis, alcohol intake and non-alcoholic fatty liver disease) predominantly leads to iCCA, rather than eCCA. This, in addition to a considerable improvement in diagnostic and stratification methods, might explain the noticeable epidemiological changes in the last decades, with an alarming rise of iCCA cases, and a tendency for eCCA to decrease worldwide[20-22]. Asymptomatic in the first stages of the disease, CCA is mostly diagnosed when the tumor has already reached an advanced stage. Besides this, as a result of its aggressive nature, lymph node invasion and distant metastasis are frequently detected at late diagnosis. This limits the therapeutic strategies available, narrowing down to just 30% of CCA cases eligible for surgical resection or liver transplant, which is considered the only effective treatment. Chemotherapy, that is the combination of gemcitabine and cisplatin, is indicated as the standard of care for unresectable disease[23]. Nevertheless, the low response rate to treatment and the high recurrence displayed by these tumors leads to a limited survival benefit that results in an unfortunate 5-year OS of 7-20%[24].

4.3.2 Biological diversity

CCA is not only a heterogeneous malignancy in terms of anatomical location, but also on a morphological and histological level. Indeed, up to three different growth patterns have been described in iCCA. The most common type accounting for 65% of iCCA cases, arises from the hepatic parenchyma as a mass and is known as the mass-forming (MF) pattern. The periductal infiltrating (PI), characterized by a progressive growth that affects the wall of the large bile ducts only represents 6% of iCCAs. 4% are intraductal growing (IG) type and mainly grow in the duct lumina. On a macroscopic level, pCCA and dCCA present similar features with a poorly differentiated pattern, as a result from a mix of both IG and PI type (Figure 2.A)[25, 26].

According to their histopathological presentation, pCCA and dCCA are mainly adenocarcinomas or papillary tumors with mucinous features. In contrast, iCCA manifests as adenocarcinomas with glandular growth patterns surrounded by a highly desmoplastic stroma, and tends to invade the liver parenchyma. In addition, the level and size of the lesion are parameters used for further stratification. As a result, tumors with a small tubular architecture named as *small bile duct type iCCA* show a tubular architecture with a MF pattern where production of mucin is barely present. In contrast, *large bile duct type iCCA* exhibits more IG and PI growth patterns affecting large ducts with a papillary structure (Figure 2.B)[26].

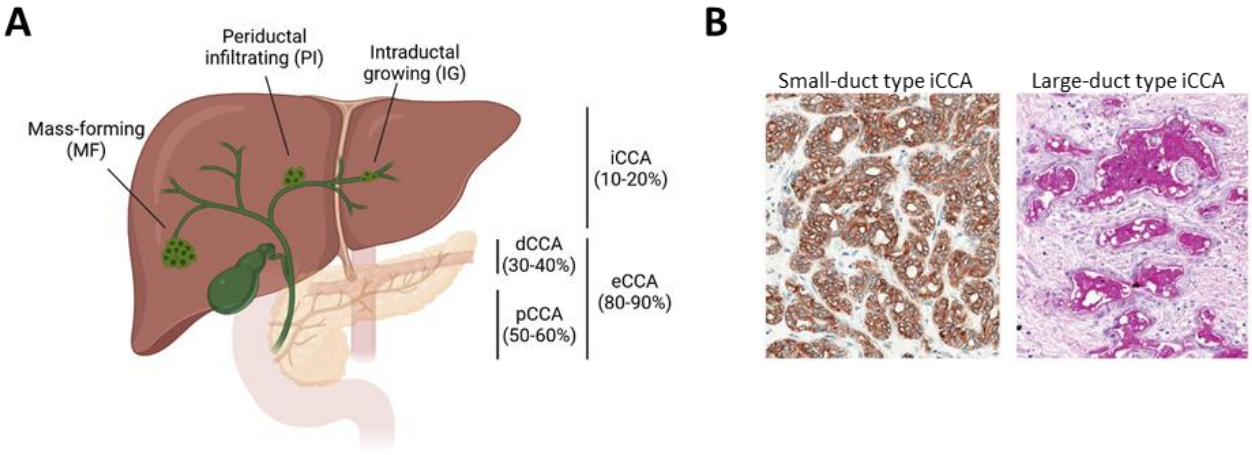

Figure 2. CCA is a heterogeneous disease at multiple levels. (A) Classification of CCA according to anatomical location and morphological features. (B) Representative histology of variants of CCA according to size and growth patterns. Adapted from Banales *et al.* 2020[2].

Furthermore, additional subtypes with mixed features as in the case of HCC-iCCA rare cancers, prompted the discussion of the cell of origin as an additional factor contributing to the heterogeneity of this disease. Within the liver, iCCA was proposed to initiate from the pathological transformation of bi-potent hepatic progenitor cells or cholangiocytes (Figure 3)[16]. However, recent studies have shown that also hepatocytes -which are the source for HCC- can lead to iCCA[27]. This is mainly explained by the highly plastic and transforming capacity of hepatocytes, which is missing in the case of cholangiocytes. In line with this, inflammation-driven and genetic and epigenetic reprogramming of hepatocytes (aberrant Notch signalling, activation of *AKT* pathway or *IDH1* mutations) lead to the induction of cellular differentiation and initiation of tumors[16, 27-30].

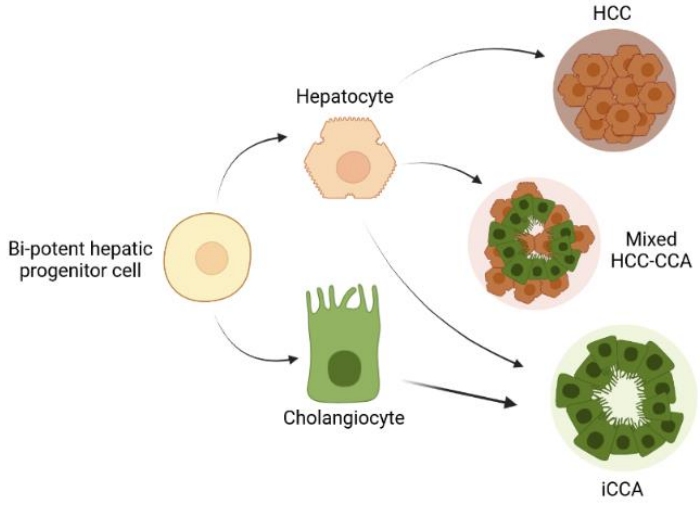

Figure 3. PLC may originate from multiple cell types. Hepatocytes and cholangiocytes have their origin from bi-potent hepatic progenitor cells. In turn, pathological transformation of mature hepatocytes and cholangiocytes lead to HCC and iCCA, respectively. Moreover, hepatocyte reprogramming can develop in both de-differentiated mixed HCC-CCA and iCCA[16].

4.3.3 Drivers of cholangiocarcinogenesis

Cholangiocarcinogenesis is a multi-step process that combines several mechanisms driving the initiation and progression of this disease (Figure 4). This includes the deregulation of not only intracellular signalling pathways controlling cellular proliferation and differentiation, but also extracellular processes that shape the tumor microenvironment and enhance further tumor growth and migration[2]. In the past decades, increasing efforts have been made on the characterization

of molecular targets of CCA, with the aim of generating insights to improve patient stratification and subsequently optimizing CCA clinical management.

Recent integrative genomic and epigenomic analyses of human samples have identified key drivers in the pathogenesis of CCA. Even though the molecular profiles of both iCCA and eCCA slightly differ and vary according to etiology and location[31], there are frequent common targets that contribute to cholangiocarcinogenesis. Among these factors, several studies sympathize in the deregulation of the EGFR downstream signaling pathway, which is involved in cell proliferation and migration processes[32]. These genetic alterations correlate with a denominated "proliferation class", denoting oncogenic signaling pathways[33], including the gain-of-function mutations in *KRAS*, described in 8-54% of CCA cases, as well as aberrant activation of *PIK3CA* (9-32%)[34]. Also, *MYC* amplification, greatly associated with the initiation of HCC pathogenesis[35], was described to play a role as an oncogenic driver of CCA proliferation and differentiation. In addition, mutations were identified in signaling pathways linked with cell cycle control and DNA damage response (DDR) (*TP53, CDKN2A, SMAD4, CCND1, ATM, ROBO1, ROBO2, BRCA1 and BRCA2*)[31]. Immune impairment (JAK-STAT3 and TNF signaling) and Notch signaling, Hippo and WNT-CTNNB1 (*APC*) pathways, have also been found to drive the initiation and progression of this malignancy[36].

Notably, genetic aberrations which seem to be recurrent and specific for iCCA are *FGFR2* fusions and *IDH* mutations. In particular, *FGFR2* fusions with other genes enable kinase activation which consequently results in increased cell proliferation[37]. In the same way, hotspot mutations in *IDH1* and *IDH2* genes are considered one of the most common genetic alterations in CCA, tightly associated with epigenetic rewiring[3, 38]. These molecular mechanisms have become of special interest in recent years because of their great potential as therapeutic targets[39, 40].

Furthermore, CCA has been profiled as a tumor rich in epigenetic aberrations, including DNA methylation, histone modifications and dysregulation of non-coding RNAs, which ultimately impair gene expression. Several studies have acknowledged the presence of remarkable hypermethylation signatures affecting the promoter regions of tumor suppressors, which translates into genetic silencing and inhibition of the homeostatic functions[41]. Genes affected by this phenomenon would include cell cycle control genes (*p16^{INK4a}/CDKN2A*, *p14^{ARF}*) and chromatin remodeling genes (*PBRM1, BAP1, ARID1* and *ARID2*), as well as genes involved in inflammatory response such as *SOCS-3*, which downregulation leads to the overexpression of IL-6, a key cytokine that plays an oncogenic role in the malignant transformation of CCA[2]. In regards to histone modifications, upregulated histone deacetylases (HDACs) have been

described to promote cell proliferation in CCA. In line with this observation, the use of HDAC inhibitors has been associated with a reduction of oncogenic capacity of CCA *in vitro.* Comparatively, micro-RNAs (miRNAs) have been described to modify the expression of tumor suppressors and oncogenes involved in the regulation of several processes ranging from inflammation to chemoresistance. In particular, miRNAs have opposing dual effects by either promoting or inhibiting cholangiocarcinogenesis[28].

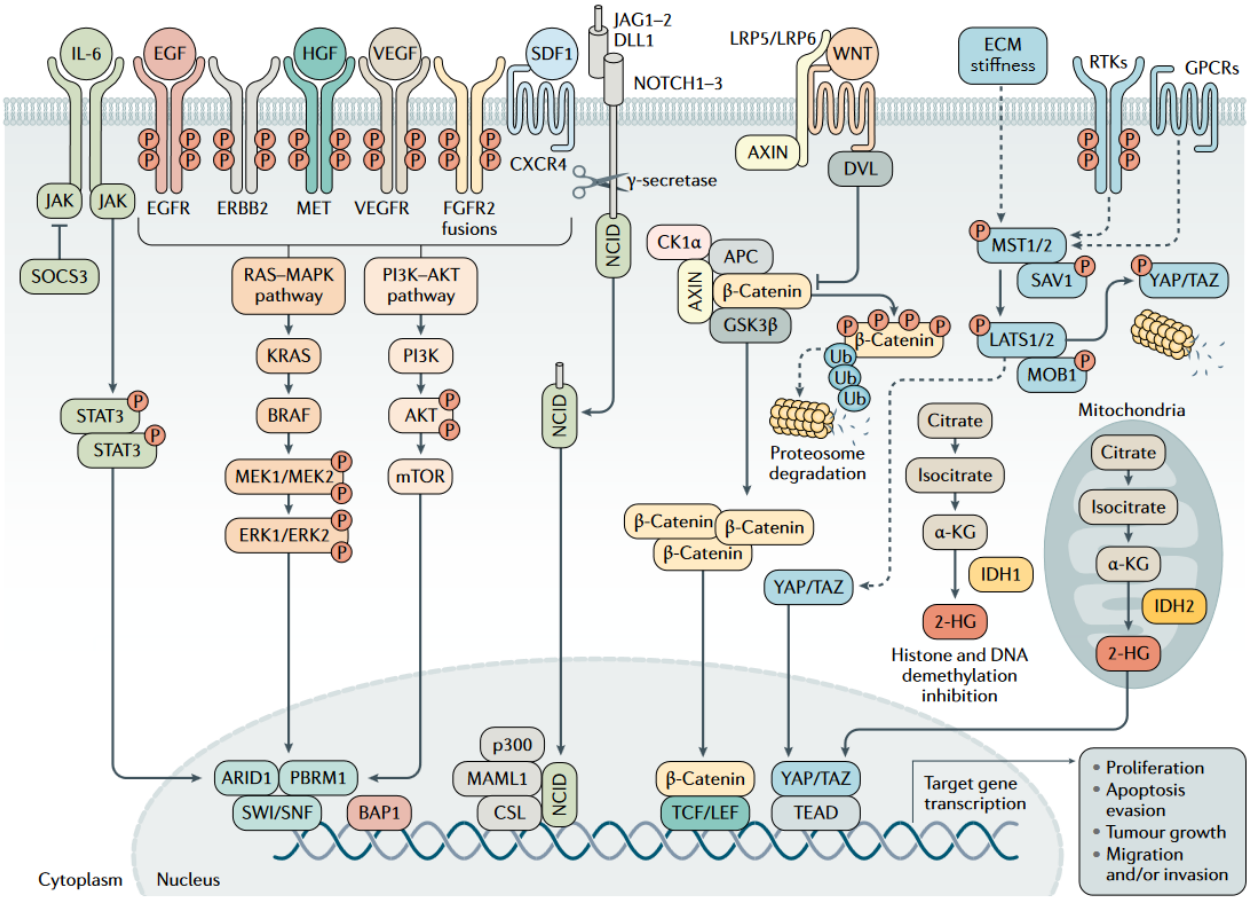

Figure 4. Molecular heterogeneity in CCA. The malignant transformation and tumor progression results from the abnormal expression of factors regulating homeostatic processes involved in cellular proliferation and differentiation. This aberrant molecular network cooperates with a disturbed microenvironment that ultimately leads to CCA. Adapted from Banales *et al.* 2020[2].

4.3.4 Tumor microenvironment in cholangiocarcinoma

The molecular mechanisms driving cholangiocarcinogenesis involve the interaction of the tumor cells with a rich microenvironment that includes various cell types that interact with each other. CCA is characterized by a highly desmoplastic microenvironment that results from the activity of cancer associated fibroblasts (CAFs)[42]. Different types of CAFs have been divided into subclasses conforming to their transcriptomic signatures, associated with their role on tumor progression by driving inflammation, angiogenesis and invasiveness[43]. Interestingly, these cells release various paracrine factors that provide the scaffold for tumor development. Among these, there are fibrogenic factors as TGF-β1, CTCF, extracellular matrix (ECM) components, periostin, tenascin-C and osteopontin, and matrix metalloproteases (MMPs) like MMP1, MMP2, MMP3 and MMP9[44]. Certainly, the crosstalk between CAFs and several immune cells is evident through the release of cytokines (IL-6, IL-33), chemokines (CXCL2 and CXCL12) and ECM factors as hyaluronic acid[45]. Consequently, CCA displays an abundant tumor immune microenvironment (TIME), that can potentially be targeted by combining immunotherapy with immune checkpoint inhibitors. In particular, myeloid cells, including MDSCs – defined as $CD45^+CD11c^-CD11b^+F4/80^-GR1^+$- and tumor-associated macrophages (TAM) expressing programmed death-ligand 1 (PD-L1) – that is $CD45^+CD11b^+F4/80^{int}CD206^+PD\text{-}L1^+$ macrophages- have been described to exhibit an immunosuppressive role by impairing T cell response, enhancing proliferation and invasion of iCCA[46-48]. Additional immune cells driving this immune evasion are regulatory T cells (T_{regs}) defined as $FoxP3^+CD4^+$ tumor-infiltrating lymphocytes (TILs) that Konishi and colleagues described to functionally inhibit the cytotoxic function of $CD8^+$TILs, associated with little prognosis and metastasis in iCCA[49]. Furthermore, tumor-associated neutrophils (TANs) -$CD66b^+$ neutrophils- have been shown to positively correlate with T_{regs}, as opposed to $CD8^+$T cells[50]. Thus, increasing studies suggest that the recruitment of different cell types to the tumor site orchestrates an immunosuppressive environment that, although challenging in terms of immunotherapy efficacy, has potential to be exploited therapeutically.

Surely, several clinical and preclinical studies have focused on evaluating new strategies to target specific immune cells as therapies for CCA. Among these approaches, chimeric antigen receptor (CAR)-T cells were tested in CCA patients and in preclinical models, PD-L1-CD3 bispecific T cell engager (BiTE) enabled T cell cytotoxicy against tumor cells[51, 52]. In addition, although limited response (5.8%) to monotherapy with pembrolizumab (PD1 inhibitory monoclonal antibody, blocking PD-1-PD-L1/PD-L2 axis) was addressed in the phase II KEYNOTE-158 clinical trial, the application of agents like nivolumab (anti-PD-1) or durvalumab (anti-PD-L1) increased to 3-11%

in smaller phase II clinical trials[53-55]. Further, combination of immune checkpoint inhibitors with other agents such as chemotherapy and immune-based therapies targeting immunosuppressive cells have resulted in better responses and prolonged OS. Certainly, results from the TOPAZ-1 trial, which assesses the combination of gemcitabine plus cisplatin with durvalumab, as well as tremelimumab (CTLA-4 inhibitor), has completely revolutionized the standard practice and accentuate the therapeutic potential of these approaches[56].

4.3.5 Tools for cholangiocarcinoma research

The complex molecular pathogenesis of CCA urges to develop appropriate tools to study such a disease. The development of pre-clinical models that contemplates the heterogeneity displayed by CCA is challenging, but also critical to understand the biological processes underlying this malignancy and also serve as an approach to develop new therapeutic strategies to tackle this disease[57].

Hence, the establishment of immortalized 2D cultures derived from normal cholangiocytes or tissue specimens from patients has been thoroughly explored *in vitro*. Thus far, more than 50 CCA-derived cell lines are available and have been very valuable to broaden our understanding on genetic aberrations and biochemical processes[58]. However, it is widely known that these models present several limitations. Apart from the fact that continuous passages can be detrimental and lead to an increased mutational load, highly differing from the original source, monocultures do not recapitulate fully the CCA tumor microenvironment and studying the interplay between different cell types remains a challenge. For that, 3D *in vitro* culture (i.e. spheroids and organoids) have been introduced as model systems in which the cancer cells can grow in a multicellular microenvironment and maintain the histopathological features of the original CCA tissue[59]. To address *in vitro* limitations, subcutaneous or orthotopic xenograft models are used as they provide an *in vivo* microenvironment and enhance the analysis of tumor growth and evolution. Some of these models lack the inflammatory and stromal response, therefore preventing the study of mechanisms resulting from the interplay between tumor and immune cells. This can be solved by employing syngeneic models, that is, material is transferred within the same species[60].

In essence, a complete CCA animal model would result in the malignant transformation of cells with a biliary phenotype that arise in an immunocompetent host and would maintain the anatomical, histopathological and molecular characteristics of the human CCA. With that purpose,

on top of transplantation models of liver-derived organoids and administration of hepatocarcinogens that can lead to CCA, also genetically engineered mouse models (GEMMs) and transposon-based models have been developed to model the molecular heterogeneity that defines CCA, and test the potential of novel therapeutic targets[60, 61] (Table 1).

Table 1. Selected *in vivo* models for CCA research

Genetic strategy	Model features	Histopathology	Ref.
Transplantation models			
Cholangiocytes or liver organoids from *Kras$^{LSL-G12D}$;Tp53$^{f/f}$*	Orthotopic implantation in the liver, tumor latency 6-8 weeks	iCCA exclusive, highly enriched in stromal compartment	62, 63
Carcinogen-based CCA animal models			
TAA administration in *CK19-Cre^{ERT};Rosa26$^{LSL-YFP}$* or *Alb-Cre^{ERT};Rosa26$^{LSL-LacZ}$*	100% incidence at 30 weeks	Pure iCCA	64-66
Alb-Cre^{ERT};Hnf4a$^{f/f}$, *Phd2$^{+/-}$ or Alb-Cre;Jnk1$^{f/f}$;Jnk2$^{-/-}$* treated with DEN/DMN	Presence of inflammatory response with long latency	Not established CCA, cholangioma-like structures	67, 68
Furan	Chronic inflammation, variable latency according to dose	Cholangiofibrosis and CCA development	69
Tp53$^{-/-}$ and *Tp53$^{+/-}$* treated with CCl_4	50% penetrance, chronic inflammation and biliary fibrosis	Exclusive iCCA	70
Cre-*loxP* GEMMs			
Alb-Cre;Tp53$^{f/f}$	Long latency (14-20months)	Mixed HCC-CCA	71
Alb-Cre;Kras$^{LSL-G12D}$;Idh1$^{LSL-R132}$	100% penetrance, latency 27-54 weeks	Multifocal iCCA with distant metastasis	72
Alb-Cre; Kras$^{LSL-G12D/+}$;Pten$^{f/f}$	Full penetrance after 7 weeks	Pure iCCA with abundant desmoplatic stroma	73, 74
Alb-Cre;Smad4$^{f/f}$;Pten$^{f/f}$	100% penetrance, 4-5 months	Multistep iCCA development including different cancer stages	75
Alb-Cre;Kras$^{LSL-G12D/+}$;Tp53$^{f/f}$	9-19 weeks	iCCA in 80% (includes mixed HCC-iCCA and HCC phenotype)	76

Alb-Cre;NICD;Tp53$^{f/f}$	100% penetrance with long tumor latency (8-9 months)	iCCA with rich stromal and inflammatory microenvironment	77
Sox9-Cre^{ERT};Kras$^{LSL-G12D/+}$; Tp53$^{f/f}$	Full penetrance with 30 weeks average latency	iCCA exclusive, cholangiocytes as cell of origin	78
Sleeping beauty-based models			
myr-AKT;NICD	Lesions appear after 1.5 weeks, leads to 100% incidence after 7-8 weeks	Cystic iCCA differentiation	79
myr-AKT;YAP^{S127A}	Endpoint 5-7 weeks	Small type duct iCCA	80
myr-AKT;NRAS^{G12V}	Endpoint 3-4 weeks	HCC and iCCA	81
KRAS^{G12D};p53	Endpoint 5 weeks	Mixed feature of HCC-iCCA	82
KRAS^{G12D};p19^{ARF}	Endpoint 4-5 weeks	iCCA	43

TAA:Thioacetamine; DEN:Dimethylnitrosamine;DMN: Diethylnitrosamine; CCl_4: Carbon tetrachloride; BECs: biliary epithelial cells; NICD: Notch intracellular domain.

4.4 Isocitrate dehydrogenases mutations

A molecular breakthrough in the field of cholangiocarcinoma has been the identification of hotspot mutations in the isocitrate dehydrogenase (IDH) gene[83]. *IDH* is a homodimeric enzyme that takes part in the cellular metabolism. In detail, it is responsible for the oxidative decarboxylation of isocitrate into α-ketoglutarate (α-KG) which is part of the tricarboxylic acid (TCA) cycle, concomitantly converting the cofactor NADP+ to NADPH and also leading to CO_2 production. These products support physiological cellular mechanisms as NADPH protects the cells against toxic effects from reactive oxygen species (ROS), and α-KG acts as the substrate for cytoplasmic and nuclear α-KG-dependent dioxygenases[84]. *IDH* encodes three isoforms that although share the same catalytic activity, are located in different cellular locations: *IDH1* is located in the cytoplasm, while *IDH2* and *IDH3* are located in the mitochondria[85].

4.4.1 Mutant-*IDH* leads to the oncometabolite 2-HG

Recurrent missense mutations have been associated with different tumor types. These modifications mostly affect the arginine amino acid in position 132 (R132) in the *IDH1* catalytic site. Analogously, arginine 140 (R140) or 172 (R172) are affected in *IDH2*[86]. As a result of the altered substrate specificity, *IDH* mutations lead to a new enzymatic activity that favors the NADPH-dependent reduction of α-KG to 2-hydroxyglutarate (2-HG), which in turn competitively inhibits pathways dependent on α-KG as a substrate[87] (Figure 5).

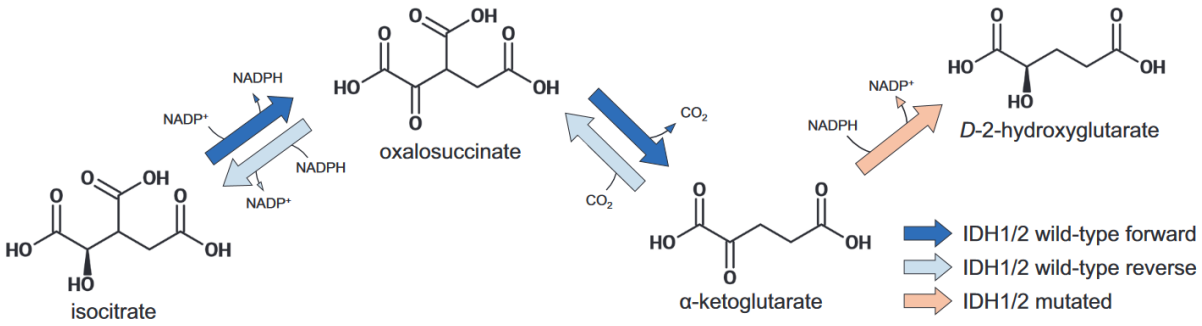

Figure 5. Neomorphic activity of mutant-*IDH1/2* leads to 2-HG accumulation. *IDH1/2* wild-type catalyzes the reversible reaction from isocitrate to α-KG, a two-step reaction that involves oxalosuccinate as the unstable intermediate. In contrast, when mutated, IDH1/2 acquire a new catalytic activity that converts α-KG into the oncometabolite 2-HG. Adapted from Molenaar *et al.* 2018[88].

Collectively, gain-of-function amino acid substitutions in *IDH* gene lead to an excessive accumulation of the oncometabolite 2-HG that impairs normal cellular processes, promoting malignant transformation and tumor development through several aberrant mechanisms[83]. This involves epigenetic remodeling by inhibiting the TET family of DNA demethylases and histone demethylases of the Jumanji class, leading to an association of *IDH*-mutated cancers with hypermethylated states that lead to dysregulated cellular differentiation and it is also linked to the DDR[89-92]. In addition, increased 2-HG level stabilizes hypoxia-inducible factor 1-alpha (HIF-1α) which in turn stimulates the transcription of the vascular endothelial growth factor (VEGF), that promotes angiogenesis, critical for tumor growth[93, 94]. Further, *IDH*-mutant cells result in a deregulated NADP+/NADPH ratio, that highly impacts the metabolic landscape. Due to the reduction in NADPH production, redox homeostasis as well as biosynthesis of nucleotides and lipids are affected by increasing ROS and decreasing level of reduced glutathione (GSH), which is the most abundant antioxidant[84]. Moreover, *IDH1* mutations have also been associated with an

upregulation of mTOR signaling, master regulator of intracellular metabolism, controlling cell proliferation and growth[95]. Beyond these α-KG-dependent mechanisms, 2-HG can also influence lysine and proline hydroxylases activity, detrimental for the collagen maturation and ultimately affecting the extracellular matrix (ECM) formation[86].

Due to the widespread effects of mutant-*IDH* affect various homeostatic processes, increasing studies have focused on developing new small-molecule inhibitors[96]. With the aim of restoring normal enzymatic activities, although several compounds have been proposed and are undergoing clinical trials, only two have been FDA-approved: Ivosidenib (AG-120) and Enasidenib (AG-221)[97]. Ivosidenib (TIBSOVO®) is the first oral, targeted therapy against *IDH1* mutation, developed by Agios Pharmaceuticals, Inc. It is indicated by the FDA for newly diagnosed AML since 2019 (evaluated in the registered clinical trial on ClinicalTrials.gov, NCT03173248)[98], relapsed or refractory AML since 2021 (NCT02074839)[99], and for locally advanced or metastatic CCA since August 2022 (ClarIDH1y trial, NCT02989857)[100]. Analogously, Enasidenib (IDHIFA®) is used for the treatment of adult patients diagnosed with relapsed or refractory AML with *IDH2* mutations since 2019 (NCT01915498)[101]. However, although the promising emergence of *IDH* inhibitors has been considerably beneficial to the management of iCCA, acquired mechanisms of resistance have been reported, suggesting the existence of additional processes and proposing combinatorial therapies[102-104].

4.4.2 Oncogenic landscape of *IDH1*-mutant iCCA

As a metabolic gene that is frequently mutated across human cancers, *IDH1/2* exhibits the highest mutational recurrence in acute myeloid leukemia (AML) (20%), glioma (80%), chondrosarcoma (80%) and cholangiocarcinoma (20%)[3, 105, 106]. With interest in the latter malignancy, the majority of the mutations appear to be exclusive for iCCA (15-30% exhibiting *IDH1* mutations and less than 5% *IDH2* mutation) while they are barely present in pCCA and dCCA[3]. In contrast to glioma, in which arginine to histidine (*IDH1 R132H)* is the recurrent alteration, or arginine to lysine (*IDH1 R172K)* in AML, the most common amino acid substitution in iCCA is arginine to cysteine (*IDH1 R132C*), which accounts for more than 60% of the cases. This leaves a small percentage to leucine (*IDH1 R132L*), glycine (*IDH1 R132G*) and serine (*IDH1 R132S*)[107]. In regards to *IDH2*, R172 is mainly affected with substitution to lysine (*IDH2 R172K*) accounting for less than 15% of iCCA, while mutations at codon R140 have not been found in iCCA[3].

The stratification of CCA molecular subclasses has allowed the identification of different clinical and molecular features that exhibit potential therapeutic vulnerabilities[108]. Consequently, molecular profiling of 94 resected CCA specimens distinguished a small subset with concomitant *IDH* and *EGFR* pathway mutations (including *KRAS* and *PIK3CA*). These patients exhibited lymph node metastasis and a survival of 4 months post-surgical resection[109]. Interestingly, additional analysis identified frequent mutations in *IDH1* and *IDH2* that showed an increased DNA methylation, H3K79 dimethylation and associated with p53 activity[38]. Recent comprehensive studies focusing on the characterization of the molecular pathogenesis of CCA found an *IDH*-mutant-enriched class. In line with previous reports, Farshidfar and colleagues identified *IDH* hotspot mutations (*IDH1 R132C* and *IDH2 R172K/S*) that differed from those found in other malignancies such as glioma or AML. Remarkably, this class showed an enrichment in mitochondrial genes, including TCA cycle components and electron transport chain, as well as high mitochondrial DNA copy number and reduced expression of chromatin modifier signature genes, specifically exhibiting an *ARID1A* hypermethylated promoter[110]. Accordingly, further studies focused on unravelling the molecular heterogeneity of CCA, found the most recurrent mutational events to be *KRAS*, *TP53* and *IDH1* in a cohort of 427 by integrating genomic data, which included both whole-exome sequencing (WES) and targeted-exome sequencing (TES). Yet, while co-occurrence of *KRAS* and *TP53* were found in a small patient subset, *IDH1* appeared to be mutually exclusive with the other defined classes, and preferentially associated with chromatin modifier genes (*ARID1A, BAP1*), consistent with previous reports[111]. In addition, a study including 412 patients, confirmed the identification of *IDH1* as one of the most frequent oncogenic alterations, (20%), being mutually exclusive with *FGFR2* fusions, defining therefore two different CCA types[112]. As a result of the integrative analysis of 52 iCCA samples focused on DNA methylation patterns, Goeppert and colleagues identified four iCCA subgroups in which one was designated as *IDH*. This subgroup was characterized by *IDH1* (R132C, R132G and R132L) and *IDH2* (R172W, R172S and R172M) mutations, which were mutually exclusive with *TP53*. Markedly, the *IDH* group exhibited a highly aberrant genome, with deletions of chromosome arms 3p (including candidate genes as *BAP1*, *SPCS1* and *PBRM1*) and 6q, as well as an excessive hypermethylation that presented cholangiolar pattern[113]. Likewise, based on co-occurrence or mutual exclusivity of driver mutations, Wang and colleagues defined three different clusters in which one was characterized by *IDH1/2* mutation and *BAP1* mutation, with a tendency to be mutually exclusive with other alterations such as activation of *KRAS* and silencing of *TP53* and *SMAD4*. In addition, this *IDH*-mutant cluster displayed histopathological features corresponding to the small bile duct type[108].

Thus, although molecular heterogeneity comprises one of the challenges in the delineation of CCA pathogenesis, increasing efforts have fostered the understanding on the molecular underpinnings driving this disease. The combination of different types of molecular analyses together with a detailed histopathological characterization may allow further stratification of CCA patients, which is essential for revealing therapeutic vulnerabilities and improve its clinical management.

4.4.3 Mutant-*IDH1* and the tumor microenvironment

Early studies indicate that the underlying mechanism by which mutant-*IDH* drives cholangiocarcinogenesis relies on the suppression of *HNF-4α*, linked to the accumulation of 2-HG levels. Consequently, hepatocyte differentiation is supressed, and the development of biliary tumors can happen in cooperation with other genetic alterations[28]. However, apart from this intrinsic tumor cell effect, emerging data point to key effects of mutant-*IDH1* also in non-tumor cells, remodelling the tumor immune microenvironment (TIME) through diverse mechanisms[45]. Remarkably, in glioma, a malignant entity with more than 80% exhibiting mutations in the *IDH1* locus, 2-HG has been identified to foster a markedly immunosuppressive environment. In detail, a reduction of the recruitment of $CD8^+$ T cells to the tumor site, and the expression of cytotoxic T lymphocytes (CTL)-attracting chemokines (CXCL9 and CXCL10) through the inhibition of STAT1 signalling pathway was described[114]. In accordance to these observations, Bunse and colleagues described the molecular mechanism of this immune evasion phenotype in *IDH1* mutant glioma. This was based on the direct effect of 2-HG, which is imported by T cells through the SLC13A3 transporter, ultimately affecting intratumoral T cell proliferation[115]. This $CD8^+$ impairment has been further associated with an aberrant glucose metabolism, specifically inhibition of lactate dehydrogenase (LDH), that impacts not only the T cell proliferation, but also INF-γ expression signature[116]. Moreover, in addition to lymphocytes, *IDH1* mutations have been reported to remodel the myeloid microenvironment. In this regard, glioma-associated macrophages express an immunosuppressive signature, as a consequence of a stimulated tryptophan degradation pathway by 2-HG[117]. Also, dendritic cell differentiation seems to be impaired by the unique TIME, consequently limiting their antigen presenting cell properties and reducing T cell activation[118]. Consistently, and specifically in iCCA, transcriptomic analysis (exome sequencing and bulk RNA sequencing) of tumors revealed that mutant-*IDH1* iCCA can be classified as “cold” tumors, because of the low T cell infiltration and cytotoxicity[119]. This correlates with preclinical studies that

further support the role of mutant *IDH1* in driving an immunosuppressive microenvironment. In depth, the use of Ivosidenib as a selective inhibitor for *IDH1*-mutant iCCA showed beneficial anti-tumor effects through the stimulation of antitumor immunity (increased $CD8^+$ T cells), turning them into “hot” tumors and overcoming immune evasion. Indeed, combination of Ivosidenib with immunotherapy (CTLA-4), induced synergistic effects against tumor development[72]. In addition, rapid development of cell and gene therapies in immuno-oncology have allowed the development of *IDH1* R132H-specific peptide vaccine, that fostered T helper cell responses against *IDH1* mutant glioma tumors[120].

In light of the better understanding of the disease, it is reasonable to propose that combinatorial treatments with small molecule inhibitors together with immunotherapies could enhance immune response and overcome mechanisms of resistance, increasing clinical benefit for patients.

5 Hypothesis and aims

Missense structural mutations in *IDH1* have been identified as one of the most frequent altered genes in iCCA. Considering the extensive effects of these modifications disrupting homeostatic processes and rewiring the tumor microenvironment, it is reasonable to propose mutant-*IDH1* as a putative driver of iCCA pathogenesis. However, the diverse molecular mechanisms driving these changes need to be further elucidated.

Consequently, the main aim of this dissertation is to carefully characterize the molecular heterogeneity of *IDH1*-mutant CCA and the impact on the TIME. With that purpose, the following objectives were defined:

- The establishment of an *in vivo* model that enhances the functional study of mutant-*IDH1* and assessment of the tumorigenic capacity on the liver microenvironment.

- Investigating the genetic heterogeneity displayed by *IDH1*-mutant iCCA by studying the potential cooperation of *IDH1* mutations with single oncogenes and tumor suppressors in driving liver cancer.

- To address the effect of *IDH1* mutations in tumor initiation, progression and invasiveness by overexpressing mutant-IDH1 in established murine iCCA models.

- In depth characterization of the interplay between *IDH1*-mutant tumor cells and immune cell compartment in the TIME of iCCA models.

- Identification of immune cells involved in tumor development and their potential as a therapeutic target for the treatment of mutant-*IDH1* iCCA.

6 Material and methods

6.1 Cloning

Design and generation of plasmids was performed with the support of Tobias Riedl from the German Cancer Research Center in Heidelberg. Q5 polymerase used in PCR reactions and cloning enzymes used in this section were purchased from New England Biolabs. Vectors were amplified using NEB® Stable Competent E. coli (New England Biolabs, Cat#C3040) and isolated using either Monarch® Plasmid Miniprep Kit (New England Biolabs, Cat#T1010L) or QIAGEN Plasmid Maxi Kit (QIAGEN, Cat#12262) according to manufacturer´s recommendations.

6.1.1 CRISPR-Cas9 knock-out

Generation of knock-out plasmids for *in vivo* experiments was performed according to previously described protocol[121]. Briefly, sgRNAs targeting either murine *Smad4* and *Cdkn2a* (*p16*^{INK4}) were selected using the Chopchop v3 web tool[122]. 0.2 pmol of annealed oligos were inserted via golden gate assembly using BbsI-HF and T4 ligase into each plasmid backbone: px330 (px330-U6-Chimeric_BB-CBh-hSpCas9)- (for *in vivo* purposes) or px459 v2.0 (pSpCas9(BB)2A-Puro)-based plasmids (for *in vitro* efficiency testing), kindly gifted by Feng Zhang (Addgene, Cat#42230 and #62988, respectively). Assembly was corroborated using Sanger Sequencing (in collaboration with Microsynth Seqlab).

6.1.2 *IDH1* overexpression plasmids

For the generation of vectors overexpressing *IDH1* for hydrodynamic delivery, pMSCV-blasticidin plasmids encoding human cDNA of *IDH1 WT*, *IDH1 R132C* and *IDH1 R132H* were XhoI/EcoRI digested. *IDH1* vectors were a kind gift from Prof. Dr. Nabeel Bardeesy (Massachusetts General Hospital in Boston). Subsequently, *IDH1* ORFs were inserted into the XhoI/EcoRI digested pT3-EF1α-Empty-EGFP vector, generously provided by Prof. Dr. med. Darjus Tschaharganeh (German Cancer Research Center in Heidelberg). To generate additional mutant-*IDH1* (*IDH1 R132G, R132L, R132S*), plasmid pT3-EF1α-IDH1 WT-IRES-EGFP was used as a template with the Q5 Site-Directed Mutagenesis kit, using respective primer pairs for each mutation. Next, donor vectors were PasI/PflFI linearized and Kozak sequence and HA-tag were inserted by using

Gibson Assembly Master Mix. Assembly was verified by Sanger Sequencing (in collaboration with Microsynth Seqlab).

Table 2: Primers for cloning

Primer name	Internal code #	Primer sequence 5´-3´
Smad4_sgRNA1_F	sgR249	CACCGGTGGCGTTAGACTCTGCCG
Smad4_sgRNA1_R	sgR250	AAACCGGCAGAGTCTAACGCCACC
Cdkn2a_sgRNA9_F	sgR271	CACCGGGGTACGACCGAAAGAGTT
Cdkn2a_sgRNA9_R	sgR272	AAACAACTCTTTCGGTCGTACCCC
hU6F	c431	GAGGGCCTATTTCCCATGATT
IDH_cloning_XhoI F	c432	TACCTCGAGATGTCCAAAAAAATCAGTGGCG
IDH1_cloning_EcoRI R	c433	TGAGAATTCTTAAAGTTTGGCCTGAGCTAGTTTG
pT3-IDH1_Seq_F	s359	GGTGTACAGTAGCTTCCAAG
pT3-IDH1_Seq R	s360	GGCAATATGGTGGAAAATAAC
IDH1_mut_R132L_F	c465	ATCATCATAGGTCTGCATGCTTATGGG
IDH1_mut_R132L_R	c466	CCCATAAGCATGCAGACCTATGATGAT
IDH1_mut_R132G_F	c467	ATCATCATAGGTGGCCATGCTTATGGG
IDH1_mut_R132G_R	c468	CCATAAGCATGGCCACCTATGATGAT
IDH1_mut_R132S_F	c469	ATCATCATAGGTAGCCATGCTTATGGG
IDH1_mut_R132S_R	c470	CCCATAAGCATGGCTACCTATGATGAT
HA-IDH1 F	c506	TCGAGCCACCATGGGGTACCCATACGACGTACCAGATTACGCTGGGG
HA-IDH1 R	c507	TCGACCCCAGCGTAATCTGGTACGTCGTATGGGTACCCCATGGTGGC
IDH1qPCR_R	hrt447	TGGCTTCTCTGAAGACCGTG
IDH1.2qPCR_F	hrt448	CTATGATGGTGACGTGCAGTCG

6.2 Cell culture

HEK293T (ATCC CRL-3216) and FL83B cells (ATCC CRL-2390), used for plasmid validation, were cultured in DMEM (Gibco, Cat#61965-026)) or DMEM/F12-Nutrient Mix (Gibco, Cat#11320033) respectively, and supplemented with 10% FCS (Gibco, Cat#10500-064) and 1% Penicillin-Streptomycin (Gibco, Cat#15140122). Cells were split three times a week 1:5 using Trypsin/EDTA solution (Sigma-Aldrich, Cat#T3924).

6.2.1 Transfection

Efficiency testing was done by transfecting the generated px459 v2.0-based plasmids into FL83B cells by using Lipofectamine 3000 (Invitrogen) in accordance to manufacturer´s protocol. One day after transfection, cells were washed and cultured with 10 µg/mL puromycin (Carl Roth) for 2 consecutive days. Afterwards, genomic DNA was extracted (QiAmp, Qiagen) and Sanger Sequencing (Microsynth Seqlab) results from PCR amplicons were submitted to Tracking of Indels by DEcomposition (TIDE) analysis.

For *IDH1* overexpression plasmids, HEK293T cells were transfected with the pT3-EF1α-HA-IDH1-EGFP plasmids by using Lipofectamine 3000 (Invitrogen, Cat#L3000001) in accordance to manufacturer´s protocols. One day after transfection, cells were washed and lysed for protein analysis.

6.3 Animal experiments

Animal experiments were conducted in agreement with German law and the governmental bodies, and approved by the Regierungspräsidium Karlsruhe (approval Nr. DKFZ332, G-39/18, G-237/18, G-275/18 and G-292/20). 7-8 weeks old male C57BL/6J mice were purchased from Janvier and genetically-engineered animals were kindly provided by Prof. Dr. Nabeel Bardeesy (Massachusetts General Hospital, Boston). Animals were housed at the German Cancer Research Center (DKFZ) (temperature 20-24°C, 45-65% humidity,12-h light-dark cycle) and kept under specific pathogen-free conditions with *ad libitum* access to food and water.

6.3.1 Hydrodynamic tail vein injection

For hydrodynamic tail vein injection (HTVi) of genetic elements[123], I injected 7-8-weeks old male mice with 2 mL of 0.9% NaCl solution (Braun, Cat#3570160) (10% of the body weight) containing the DNA plasmid mixture in the lateral tail vein within 3 to 5 seconds by using a 2 mL syringe (BD, Cat#300928) adapted to a PrecisionGlide™ Needle 26G x ½ (0.45 mm x 13 mm) (BD, Cat#305111). The plasmid concentrations were as follows:

Table 3: Plasmids for HTVi

Plasmid	Source	Concentration (ug/mouse)
pT3-EF1α-Empty-EGFP	D.Tschaharganeh, DKFZ, Heidelberg	10
pT3-EF1α-KRASG12D-EGFP	D.Tschaharganeh, DKFZ, Heidelberg	5
pT3-EF1α- myr-AKT-HA (+loxp)	Addgene, #31789	5
pT3-EF1α- myr-AKT-HA (-loxp)	G.Halder, VIB-KU Leuven, Leuven	5
pT3-EF1α-MYC	D.Tschaharganeh, DKFZ, Heidelberg	5
pT3-EF1α-NICD-IRES-mCherry	Addgene, #46047	10
pT3-EF1α-IDH1 R132x-EGFP	M.Heikenwälder, DKFZ, Heidelberg	10
px330-sgTp53	Addgene, #59910	10
px330-sgPten	D.Tschaharganeh, DKFZ, Heidelberg	10
px330-sgp16^{INK4}	M.Heikenwälder, DKFZ, Heidelberg	10
px300-sgSmad4	M.Heikenwälder, DKFZ, Heidelberg	10
pCMV-SB13	D.Tschaharganeh, DKFZ, Heidelberg	Ratio 5:1 (transposon:transposase)

6.3.2. Treatments

One week after HTVi, animals were treated twice a week intravenously with 5mg/kg of either Rat IgG_1 Isotype control (Clone GL113, Leinco Technologies, Cat#I-1105) or anti-mouse CD172a (Clone P84, Leinco Technologies, Cat#P380) diluted in 0.9%NaCl solution (Braun, Cat#3570160). Anti-mouse PD-L1 (Clone 10F.9G2, Leinco Technologies, Cat#P363) was injected at a dose of 3mg/kg intravenously twice a week alone or in combination with anti-mouse CD172a.

6.3.3 Genetically engineered mouse model

The mouse line exhibiting constitutively liver specific expression of mutant-*Idh1 R132C* was kindly provided by Prof. Dr. Nabeel Bardeesy at the Massachusetts General Hospital in Boston. Generation of the mouse strain in detail was previously described[72]. Following embryo transfer in the German Cancer Research Center in Heidelberg, genotyping and sequencing of the offspring was performed in order to select animals for experiments.

Standard Polymerase Chain Reaction (PCR) was used for mice genotyping. DNA extraction was performed from ear punches taken for marking mice. Mouse ear biopsies were digested using

300 µl of 0.06 M NaOH lysis buffer for 10 min. at 100°C in an Eppendorf® Thermomixer Compact (Eppendorf). After neutralization with 100 µl of Tris Buffer 1M pH 8, 1 µl of each sample was used for PCR. PCR conditions were optimized based on primers sequence and One*Taq*® DNA Polymerase (NEB, Cat#M0480X). PCR conditions for the Albumin Cre as well as the *Idh1* genes were: 3 min. at 94°C as a denaturation step, followed by 5 cycles of 30 s. at 94°C, 30 s. at 64°C and 1 min. at 72°C, repetition of these 5 cycles which are continued by 25 cycles of 30 s. at 94°C, 30 s. at 59°C and 1 min. at 72°C for primer annealing, and 1 min. for 72°C for the extension step and a final extension of 5 min. at 72°C. Primers used are indicated in Table 4. PCR products were electrophoresed in 2% agarose gels adding Ethidium bromide 1% diluted 1:20000 (Carl Roth, Cat#2218.1) before polymerizing and using standard 1x TAE as running buffer. 5uL of 1Kb Thermo Scientific™ GeneRuler 1kb Plus DNA ladder (Thermo Fisher, Cat#SM0332) was used for fragments´ size identification and 9uL of PCR product were loaded. Gels were run at 100V for 30 min. and later observed under UV light using Molecular Imager® Gel Doc™ XR System (Bio-Rad).

Table 4: Primer sequence for genotyping

Primer name	Internal code #	Primer sequence 5´-3´
Idh_fw1	g421	GTCAAAGGCTGGCATGGTATAAT
Idh1_rev1	g423	TGGGCTCTATGGATAACTTCGTA
Idh1_rev2	g424	GAGGACCTGAGTAACTCCCTTTT
Alb-Cre_fw1	g427	TGCACACAGATCACCTTTCC
Alb-Cre_fw2	g428	GTGAAACAGCATTGCTGTCACTT
Alb-Cre_rev1	g429	CAATGGTAGGCTCACTCTGGGAGATGAT
Alb-Cre_rev2	g430	AACACACACTGGCAGGACTGGCTAGG

6.4 Histological analysis

Immunohistochemistry staining of murine tissues were performed in collaboration with Danijela Heide, Jenny Hetzer and Tim Machauer at the German Cancer Research Center in Heidelberg. Tissues collected were fixed in Histofix 4% (Roth, Cat#P087.3) for 48 hours and changed to 70% Ethanol until paraffin-embedded. Afterwards, 2 µm sections were stained with Hematoxylin and eosin or IHC antibodies (Table 5) on a Bond MAX (Leica Biosystems) and scanned with a SCN400 slide scanner (Leica Biosystems). Processing and analysis were performed using the pathology slide viewing software Aperio ImageScope v12.4.0 by Leica Biosystems, QuPath version 0.4.0 (QuPath) or Fiji ImageJ.

Table 5: Immunohistochemistry antibodies

Staining	Dilution	Catalog #
Hematoxylin	n.a.	3801582E
Eosin	n.a.	3801601E
HA	1:300	ab9110
GFP	1:250	A-11122
mCherry	1:300	ab167453
CK19	1:500	AB_2133570
HNF4α	1:2000	ab181604
Ki67	1:200	RM-9106-S1
p21	1:1000	ab188224
Cleaved Caspase3	1:300	9661
CD4	1:1000	14-9766
CD8	1:400	98941S
F/80	1:250	T-2006
MHCII	1:500	NBP1-43312
Cd11b	1:10000	ab133357
Cd11c	1:300	97585

6.5 Isolation of immune cells for immunophenotyping and cell sorting

Mice were euthanized and the liver was perfused through the inferior vena cava with HBSS 1x (Gibco, Cat#14065072) allowing for the removal of erythrocytes until the liver turned pale. Livers were dissected, transferred to a 6-well plate filled with MACS Buffer (PBS with v/v 0.4% 0.5 M EDTA pH=8 and w/v 0.5% albumin fraction V (Sigma-Aldrich, Cat#90604-29-8)) and left on ice until they were minced with dissecting scissors into small pieces. Liver digestion was then performed in RPMI1640 (Gibco, Cat#11875093) medium supplemented with Collagen IV 1:10 (60 U f.c.) and DNase I 1:100 (25µg/ml f.c.) and incubated for 40 min. at 37°C with gently shaking 130 rpm. Next, livers were filtered through a 100 µm cell strainer (Corning) and centrifuged for 5 min. 1600 rpm, 4°C. Lymphocyte enrichment was performed by Percoll (VWR) gradients (4 ml 80% Percoll/HBSS overlay with 8 ml 40% Percoll/HBSS) and centrifuged for 25 min. 1800g at 4°C (acceleration 4 and deceleration 0). Immune cells were washed with HBSS 1x. An additional step for red cell blood removal was performed by using RBC Lysis Buffer 1x (Biolegend,

Cat#420301) for 3 min. at room temperature. Cells were then plated in a V-bottom 96-well plate for further staining.

Isolation of leukocytes from spleen was performed by meshing half of the spleen through a 70 µm cell strainer and washed with MACS buffer. Red blood cells were removed by incubating the cells twice 5 min. at room temperature with RBC Lysis Buffer 1x (Biolegend, Cat#420301). Cells were then washed and plated in a V-bottom 96-well plate for staining.

Liver-draining lymph nodes and mesenteric lymph nodes were collected and filtered through a 70 µm cell strainer. Next, cell suspensions were centrifuged 3 min. 1600 rpm at 4°C, resuspended in MACS buffer and plated in a V-bottom 96-well plate for staining.

Live/Dead cell staining was performed by using DAPI (BioLegend, Cat #422801) or LIVE/DEAD™ Fixable Blue (Thermo Fisher, Cat#L34961). DAPI was added at 1:5000 dilution directly prior to cell sorting, whereas LIVE/DEAD™ Fixable Blue was used at 1:1000 for 15 min. at 4°C in the dark. After washing and centrifugation for 3 min. at 1600 rpm at 4°C, cells were stained in MACS Buffer for 20 min. at 4°C. Next, cells were washed and acquired on an Aurora spectral flow cytometer (Cytek™ Biosciences) equipped with 5 lasers in collaboration with Dominik Vonficht from the German Cancer Research Center in Heidelberg. Data was curated and logicle transformed using FlowJo (BD Biosciences) in collaboration with Dominik Vonficht from the German Cancer Research Center in Heidelberg. Multiparameter spectral flow cytometry data was preprocessed in R using the Spectre package[124] and only in presence of batch effects that can arise during staining, data from different organs were integrated using *Harmony*[125]. After successful integration of data, cells were clustered using *FlowSOM* algorithm[126] or *Fast PhenoGraph*[127]. Remaining cellular doublets and aberrant cells were removed from further analysis and data was annotated using known cell surface markers for respective cell types and CITE-seq reference data of murine lymphoid organs available in[128].

Cell sorting was performed under sterile conditions in collaboration with Dominik Vonficht from the German Cancer Research Center in Heidelberg, using a BD FACS Aria™ Fusion equipped with a 70 µm nozzle.

Table 6: Flow cytometry antibodies

Fuorochrome	Target	Dilution	Clone	Catalog No.
BUV395	F4/80	1:100	T45-2342	565614
BUV395	CD19	1:400	1D3	563557
BUV563	CD3	1:300	17A2	741319

BUV615	CD103	1:300	M290	751590
BUV737	CD11b	1:1000	M1/70	612801
BUV805	CD4	1:500	GK1.5	612900
BV421	CD11c	1:300	n418	117343
Super Bright 436	CD279 (PD-1)	1:200	J43	62-9985-82
Pacific Blue	CD62L	1:500	mel-14	104424
BV510	CD86	1:200	GL-1	105039
BV570	NK1.1	1:300	PK136	108733
BV605	CD44	1:1000	im7	103047
BV650	XCR1	1:300	ZET	148220
BV711	CD25	1:200	pc61	102049
BV711	CD274 (PD-L1)	1:300	MIH5	563369
BV785	MHC-II (I-A/I-E)	1:500	M5/114:15:2	107645
BV785	CD25	1:600	PC61	102051
BB515	CD19	1:1000	1D3	564531
FITC	TCRγδ	1:200	UC7-13D5	107504
FITC	CD44	1:1000	IM7	103022
FITC	CD11c	1:300	N418	117305
Spark Blue™ 550	Ly6G	1:300	1A8	127663
PerCp-Cy5.5	Ly6C	1:500	HK1.4	128011
PerCp-Cy5.5	CD8	1:1000	53-6.7	100734
PE	CD84	1:100	mCD84.7	122806
PE	CD64	1:100	X54-5/7.1	139303
PE	CD45	1:1000	30-F11	12-0451-82
PE	CD223 (LAG-3)	1:200	C9B7W	125208
PE-Dazzle	CD172a (SIRPα)	1:300	P84	144016
PE-Dazzle	CD279 (PD-1)	1:300	RMP1-30	109116
PE-Cy5	CD274 (PD-L1)	1:200	10F.9G2	124343
PE-Cy7	CD14	1:500	sa14-2	123316
PE-Cy7	CD366 (Tim3)	1:300	RMT3-23	119716
PE-Cy7	MHC-II (I-A/I-E)	1:1500	M5/114.15.2	107630
PE/Fire™ 810	B220	1:300	RA3-6B2	103287
APC	CD127	1:30	SB/199	564175
APC	CD11b	1:500	M1/70	17-0112-83
APC	CD152 (CTLA-4)	1:200	UC10-4B9	106309
Alexa Fluor® 647	CD192 (CCR2)	1:300	SA203G11	150603
Alexa Fluor 700	CD8	1:500	53-6.7	56-0081-82

APC-Cy7	TCRβ	1:300	H57-597	109219
APC-eFluor® 780	CD62L	1:500	mel-14	47-0621-82
APC/Fire™ 810	CD45	1:500	30-F11	103173

6.6 Cellular co-culture assays

Co-culture assays were done in collaboration with Dominik Vonficht from the German Cancer Research Center in Heidelberg. In detail, DCs were isolated from spleen and liver from tumor-bearing mice injected by HTVi using a BD FACS Aria™ Fusion. Next, OT-I $CD8^+$ T cells and OT-II $CD4^+$ T cells were isolated by magnetic negative selection from processed lymph nodes and spleen of the respective animals using the $CD8a^+$ T cell Isolation Kit, mouse (Miltenyi Biotec, Cat#130-104-075) and Dynabeads™ Untouched™ Mouse CD4 Cells Kit (Thermo Fisher, Cat#11415D). Further, the selected cell fractions were purified and sorted for $CD62L^+CD44^-$ to acquire a naïve population and resuspended in T-cell clone medium[129]. T cells were subsequently labelled with CellTrace™ Violet (Thermo Fisher, Cat#C34571) and cultured in the presence or absence of the respective OVA peptides: SIINFEKL (10 µg/ml) for OT-I cells (Thermo Fisher, Cat#15332186) and $OVA_{323-339}$ (25 µg/ml) for OT-II cells (InvivoGen, Cat#vac-isq) and previously sorted DCs. After 3 days of culture, cells were stained as described above and acquired using BD FACS Fortessa, and data were analysed with FlowJo (BD Biosciences).

6.7 Analysis of metabolites via UPLC-MS

Metabolite analysis was performed in collaboration with Gernot Poschet from the Metabolomics Core Technology Platform of Heidelberg University. Determination of organic acids was performed in accordance to previous studies[130-132]. In brief, 20-50 mg of ground fresh-frozen liver tissue were used for extraction in 0.8 ml ice-cold methanol by sonication on ice. 50 µl extract was used together with 25 µl 140 mM 3-Nitrophenylhydrazine hydrochloride (Sigma-Aldrich), 25 µl methanol and 100 µl 50 mM Ethyl-3-(3-dimethylaminopropyl) carbodiimide hydrochloride (Sigma-Aldrich) and incubated for 20 min. at 60°C. Next, separation was performed on an Acquity H-class UPLC system coupled to a QDa mass detector (Waters) using an Acquity HSS T3 column (100 mm x 2.1 mm, 1.8 µm, Waters) at 40°C. Increase of the concentration of 0.1 % formic acid in acetonitrile (B) in 0.1 % formic acid in water (A) at 0.55 ml/min as follows: 2 min. 15% B, 2.01 min. 31% B, 5 min. 54% B, 5.01 min. 90% B, hold for 2 min., and return to 15% B in 2 min. was

used for separation of derivates. Mass signals for the compounds of interest were detected in single ion record (SIR) mode with a negative detector polarity and 0.8 kV capillary voltage: 2-HG (417.0 m/z; 15V CV). Empower3 software suite (Waters) was used for data acquisition processing. Organic acids were quantified using ultrapure standards (Sigma).

6.8 Serum liver damage parameters

Blood was collected from the heart after sacrifice by carbon dioxide exposure, and centrifuged at 13000 rpm for 10min. Serum was used to measure liver damage parameters such as Alanine Aminotransferase (ALT), Aspartate Transaminase (AST), Alkaline Phosphatase (ALP) and Lipase (LIP) by using a Fuji DRI-CHEM NX500i machine with commercially available test application from FUJIFILM.

6.9 RNA isolation

Total RNA was extracted from cells according to the manufacturer´s recommendations using RNeasy Mini Kit (Qiagen, Cat#74034). For *in vivo* material, 20-30 mg of fresh frozen murine liver tissue were lysed with 500 µl of QIAzol (Qiagen, Cat#79306) and homogenized by using a Precellys® Evolution (Bertin Technologies). Next, phase separation (RNA isolation from DNA and proteins) was performed by adding 100 µl chloroform (Sigma-Aldrich, Cat#32211-1L-M). RNA contained in the aqueous phase was precipitated by adding 200 µl of 70% Ethanol and isolated continuing with Qiagen RNeasy Mini Kit protocol including DNAse treatment (Qiagen, #79254). RNA concentration was then measured with Qubit (Invitrogen) or NanoDrop™ spectrometer (Thermo Fisher).

6.10 RNA sequencing

High-throughput sequencing including library preparation and data quality control was performed in collaboration with the NGS Core Facility of the German Cancer Research Center in Heidelberg. Gene expression libraries were prepared following the manufacturer's protocol and sequenced on a NovaSeq 6000 Paired-End 100bp S4 (Illumina). Data processing was performed in collaboration with Detian Yuan in Shandong University in China, and Feng Han in the German Cancer Research Center in Heidelberg. Briefly, the quality of the raw sequencing data was

assessed using FastQC (v0.11.9). Adapter sequences and low-quality reads were removed using W3H Pipeline-system[133]. The clean reads were aligned to the mouse genome 38 (MG38) using STAR[134] with second read mapping to transcript. Gene expression levels were quantified using HtSeq-Count with the Ensembl annotation file (MG38)[135]. The raw read counts were then imported into R (v4.2.2) using the DESeq2 package (v1.38.3) for differential expression analysis. The Gene Set Enrichment Analysis (GSEA) was performed using the clusterProfiler package (v3.12.0)[136,137] and the org.Mm.eg.db annotation package (v3.16.0) in R. Gene Ontology (GO) enrichment analysis was performed separately for upregulated and downregulated genes, and an adjusted p-value lower than 0.05 was considered statistically significant.

6.11 Protein extraction and western blotting

Cell lysis was performed by adding lysis buffer consisting of RIPA buffer (Cell Signalling Technologies) supplemented with Complete (Roche) and PhosSTOP™ (Roche). After centrifugation, protein concentration was determined in supernatants by bicinchoninic acid (BCA) assay (Thermo Fisher) using a standard curve of bovine serum albumin (BSA) and the CLARIOStar® Reader (BMG Labtech). Equal protein concentrations were loaded onto an SDS-PAGE in a Mini-PROTEAN® Tetra Cell (Bio-Rad) running chamber at 80 V during for two hours. Next, proteins were transferred overnight to 0.2 µm nitrocellulose membranes (Millipore) by electroblotting in a Tank Electroblotter WEBTM (PeqLab), blocked with 5% milk blocking solution in TBS-Tween (TBS-T) 0.1% and incubated overnight at 4°C with the corresponding antibodies (Table 7). After washing, incubation with the secondary antibodies for one hour at room temperature was performed followed by an additional washing state. Membranes were developed using the strong western blot developer solution AceGlowTM Chemiluminiscence Substrate (VWR) or low western blot developer solution Pierce ECLWestern Blotting Substrate (Thermo Fisher) using ChemiDocTM MP Imaging System (BioRad).

Table 7: Antibodies used for Western blot

	Antibody	**Dilution**	**Catalog No.**
Primary antibodies	IDH1	1:500	3997s
	HA	1:5000	ab9110
	GFP	1:200	sc9996
	GAPDH	1:1000	A-11111
	Vinculin	1:5000	V9131

Secondary antibodies	Anti-rabbit IgG, HRP linked	1:5000	7074
	Anti-mouse IgG, HRP linked	1:5000	7076

6.12 Data visualization and statistical analysis

For data visualization and statistical analysis, one-way ANOVA with post-hoc Tukey test, Spearman correlation and the unpaired Student two-tailed t test were performed by using GraphPad Prism software version 9 (GraphPad software) or R (version 4.2) using the package ggplot2. Data are shown as mean±SEM, as individual points and boxplots according to previous publications[138]. Statistical significance is indicated as follows: 0.1<p<0.05, *p< 0.05, **p< 0.01, ***p< 0.001 and ****p< 0.0001.

7 Results

7.1 Determining the impact of *IDH1* mutations on the liver microenvironment

In an effort to investigate the effect that different *IDH1* mutations have on the remodelling of the liver microenvironment, I adopted a system that allows the rapid induction of particular and tailored genetic modifications *in vivo*. This model is based on the hydrodynamic tail vein injection and sleeping beauty mediated somatic integration of genetic factors (overexpression of genes by transposon-based vectors or deletion by using CRISPR Cas9 vectors). This allows delivering DNA in a specific manner into hepatocytes by generating an increase in blood pressure which in turn redirects the blood flow into the liver[79, 123, 139]. The technology enables to investigate the effects of various signalling pathways, the cooperation between genetic alterations in driving tumorigenesis in murine models, as well as their impact on the hepatic immune microenvironment, thereby gaining insight into the mechanisms driving disease.

7.1.1 Generation and *in vitro* validation of *IDH1* vectors

To generate the *IDH1* vectors for HTVi, human cDNA of *wild-type IDH1* (*IDH1 WT*), *IDH1 R132C* and *IDH1 R132H* mutations were obtained from the vectors pMSCV-blasticidin *IDH1 WT*, *IDH1 R132C* and *IDH1 R132H*, kindly provided by Nabeel Bardeesy (Massachusetts General Hospital in Boston-USA) and previously published by Saha and colleagues[28]. I in collaboration with Tobias Riedl from the German Cancer Research Center engineered the plasmids for HTVi delivery. The *IDH1* cDNA sequences were then subcloned into the transposon-based pT3-EF1α-IRES-EGFP (Empty) vector used for HTVi. This construct allows gene overexpression by the sleeping beauty-system and contains the gene of interest downstream the EF1α promoter followed by an IRES element and EGFP reporter. A N-terminal HA-tag was included to monitor the *IDH1* expression. Moreover, in order to understand the effect of additional IDH1-mutations described in human iCCA, constructs containing the *IDH1*-mutations R132G, R132L, R132S were generated by PCR site-directed mutagenesis using *IDH1 WT* as a template (Figure 6.A). Afterwards, the plasmid sequence was verified by Sanger sequencing.

With the purpose of validating the overexpression of the different *IDH1*-mutated versions *in vitro*, I transfected HEK293T cells and protein was harvested after 2 days, to further evaluate the induction of *IDH1* expression by western blotting. The results demonstrated the successful overexpression of *IDH1* using an antibody recognizing the N terminus of human *IDH1*, as well as

the expression of HA-tag and GFP reporter, which was detected in all the *IDH1*-transfected HEK293T cells, but not in the negative control, that is non-transfected HEK293T cells (Figure 6.B).

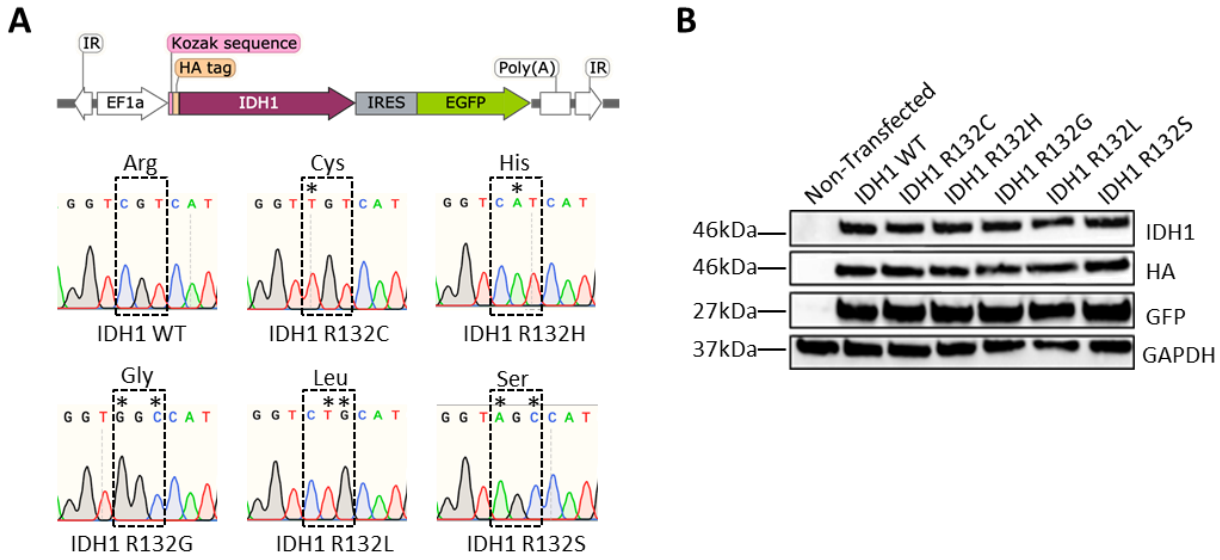

Figure 6. Validation of engineered *IDH1* vectors *in vitro*. (A) Representative scheme of engineered *IDH1* vectors for HTVi, together with the corresponding Sanger sequencing chromatogram for each plasmid. IR stands for inverted repeats of sleeping beauty sequence (B) Protein lysates from HEK293T cells transfected with the various *IDH1* vectors and analyzed by western blotting.

7.1.2 Mutant-*IDH1* leads to an increase in 2-HG *in vivo,* but fails to drive tumor initiation

Once the expression of the constructs was validated *in vitro*, I further studied the potential of mutant-*IDH1* in an *in vivo* experimental setting. For that, I delivered single mutant-*IDH1* vectors as shown in Figure 7.A. in 8-weeks old C57BL/6J males by HTVi. Additional groups injected with Empty and *IDH1 WT* vectors were included as technical and biological controls, respectively. Mice were then sacrificed after 3 months of HTVi, when blood and livers were collected and processed for histological analysis (Figure 7.B).

Macroscopic evaluation of livers did not reveal apparent morphological changes, which was also confirmed by IHC H&E staining showing a normal liver structure. Transfection of hepatocytes was corroborated by IHC staining of GFP reporter, found in all the different groups injected with plasmids. On the contrary, HA-tag was just detected in the *IDH1*-injected animals, but not in the Empty vector group (which does not contain *IDH1* sequence, therefore no HA-tag expression is expected) (Figure 7.C). This demonstrates the successful plasmid delivery *in vivo,* and also allows

to identify those animals in which technical problems could have occurred (such as unsuccessful plasmid delivery). These animals were therefore removed from the study.

In accordance with the HTVi method, staining of serial cuts by IHC indicated that the same transfected cell, based on localization, was expressing both HA-tag and GFP reporter. Likewise, the quantification of cells positive for these markers showed the same trends (Figure 7.D-E). However, the ratio HA/GFP was greater than 1, which could be explained by the limited the translational efficiency of the IRES element (Figure 7.F). Indeed, it has been reported as one of the disadvantages of the IRES system, in which the gene upstream of an IRES shows a robust expression (in this case *IDH1*, tagged with HA), whereas the downstream gene (EGFP in this setting) is expressed at lower levels[140]. Nevertheless, this drawback does not affect the present study as the target gene (*IDH1*) is upstream of the IRES element, and its expression is monitored by an HA-tag. Interestingly, quantification of HA-tag and GFP positive cells revealed a high variability in transfection efficiency when comparing animals injected with the same plasmid, therefore belonging to the same group, and also between *IDH1 WT* and different *IDH1*-mutant variants.

Following these observations, I proceeded to study the metabolic plasticity induced by *IDH1* mutations within the liver microenvironment. As previously described, *IDH1* mutations lead to the overproduction of the oncometabolite 2-HG[87]. With the purpose of confirming the biological effect derived by the delivered mutant-*IDH1*, TCA cycle metabolite levels were determined in murine liver tissue in collaboration with the Metabolomics Core Technology Platform of Heidelberg University. Ground fresh frozen liver tissue samples from injected animals were processed and analyzed by UPLC-MS method.

In line with prior reports describing the acquisition of a neo-enzymatic activity as a feature shared by all *IDH1* mutations, which convert α-KG to 2-HG[87], I observed a remarkable elevation of the 2-HG content in the *IDH1*-mutant groups, but not in the Empty and *IDH1 WT* groups (Figure 7.G). Noticeably, the variations seen in 2-HG content between the distinct experimental groups were very similar to the trends detected in the total number of transfected cells (quantified by HA^+ cells). For this reason, I evaluated the linear relationship between the two variables: 2-HG levels and HA^+ cells/mm^2. Empty and *IDH1*-mutant groups were included in the analysis. On the contrary, *IDH1 WT* group was considered a confounding variable due to the fact that even if it exhibited HA positive cells, it did not lead to 2-HG accumulation, and it was therefore excluded from this analysis. The Pearson correlation coefficient ($r = 0.7411$) indicated that the 2-HG content can be

explained to a large extent by a linear function of the number of HA positive cells detected (Figure 7.H).

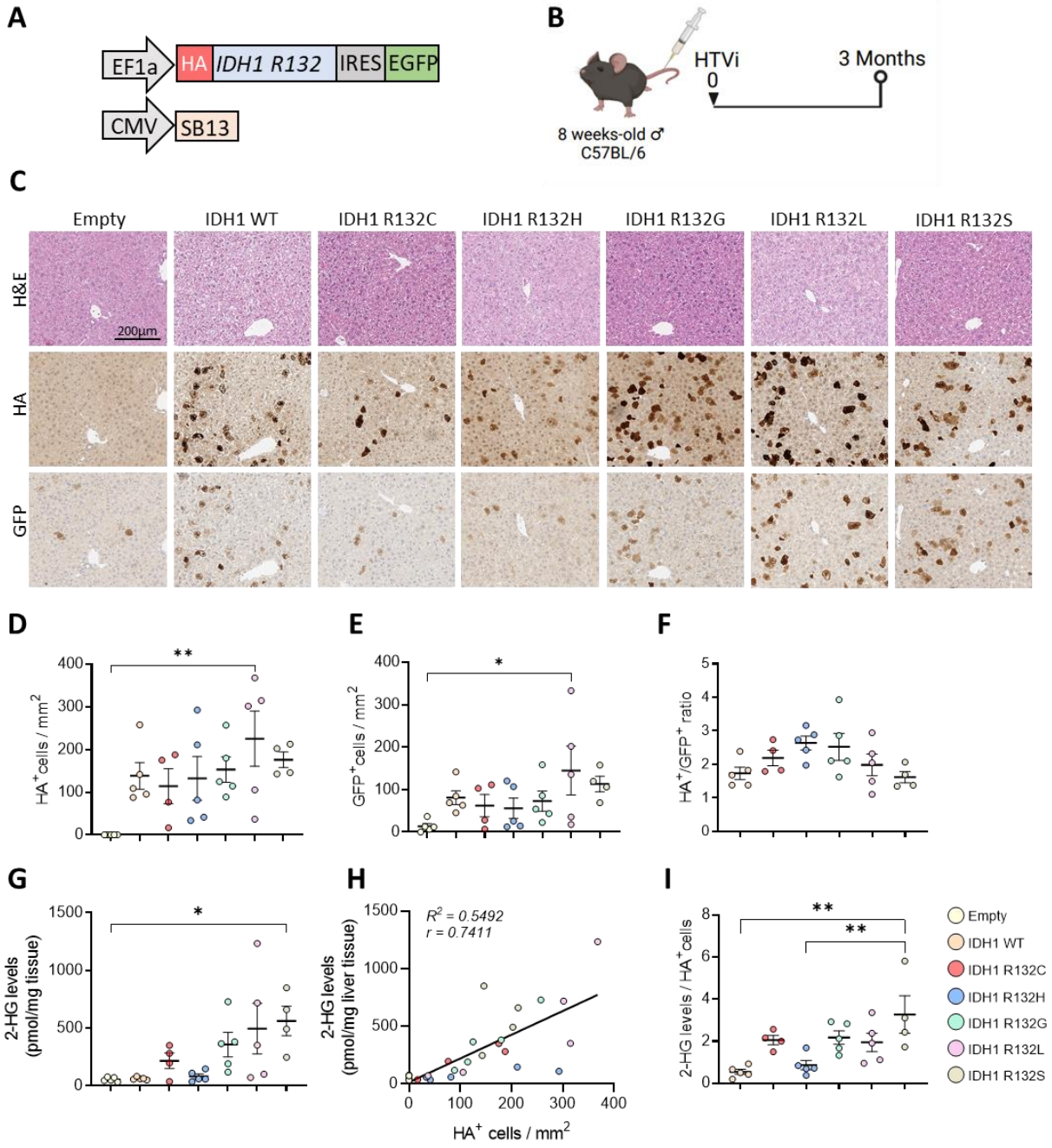

Figure 7. Validation of the expression and biological function of mutant-*IDH1 in vivo.* (A) Schematic representation of plasmids delivered by HTVi. (B) *In vivo* experimental setting: 8-week old C57BL/6J males were injected by HTVi and livers were collected after 3 months. (C) Representative pictures from IHC staining of livers injected with corresponding vectors by HTVi. H&E, HA-tag to monitor *IDH1* expression and GFP staining shown. Scale bar= 200µm. (D) Quantification of HA-tag and (E) GFP transfected cells by HTVi. (F) Ratio of HA^+/GFP^+ cells show the genes transcribed. (G) 2-HG content in murine liver tissue from animals injected with *IDH1*-vectors by HTVi and determined by UPLC-MS. (H) Linear relationship between

2-HG levels and HA^+ cells/mm^2. Linear regression (black solid line) displayed. Empty and *IDH1*-mutant groups included. (I) Ratio of 2-HG levels/HA^+ cells indicates the amount of oncometabolite per transfected cell. Data shown as mean ±SEM. Significance determined by one-way analysis of variance with post hoc Tukey´s multiple comparison test. *p<0.05 and **p<0.001 indicated (D-F, I).

Next, in order to compare the 2-HG levels between distinct groups and overcome the differences in transfection efficiency between animals, I determined the amount of 2-HG produced per cell (HA^+) (Figure 7.I). The ratio of 2-HG levels/HA^+ cells showed that the *IDH1* mutations found with increased frequency in human iCCA, namely *IDH1 R132C*, *IDH1 R132G*, *IDH1 R132L* and *IDH1 R132S*, lead to a greater production of 2-HG when compared to *IDH1 WT* and *IDH1 R132H*, the latter dominating in diffuse gliomas. Surprisingly, *IDH1 R132S* was the mutation that lead to a higher overproduction of 2-HG, and not *IDH1 R132C*, the most frequent mutation reported in human iCCA. In this regard, it has been proposed that certain mutations are predisposed to appear in specific malignancies, such as *IDH1 R132H* in the case of glioma[141]. In the case of iCCA, this observation seems to be in favor of the *IDH1 R132C* mutation. This predisposition could possibly be explained by the toxicity that 2-HG exerts in the cells. In my hands, *IDH1 R132S*-derived 2-HG content would reach excessive levels that would eventually lead to cell death. This selection pressure would enhance the *IDH1 R132C* cells, which produce a lower 2-HG content, to cope with these levels and remodel the homeostatic processes.

To gain a deeper understanding on the potential role of mutant-*IDH1* as a driver for liver tumorigenesis and its remodeling effect, I performed an additional *in vivo* experiment, focusing just on the most frequent *IDH1* mutation (R132C) in iCCA. Following the same experimental approach, I delivered Empty, *IDH1 WT* and *IDH1 R132C* plasmids by HTVi in 8-week old C57BL/6J males. Livers were collected after 6 months post-HTVi and further processed for histological examination (Figure 8.A).

Once more, no morphological alterations were found neither at the macroscopic nor the microscopic level (H&E staining) at this timepoint after HTVi. In terms of number of transfected cells (measured by HA^+ and GFP^+ cells), there was a large decrease when compared to the previous timepoint 3 months post-HTVi (Figure 7.D-E and Figure 8.B-C), suggesting the existence of a clearance mechanism that may lead to the elimination of transfected cells during the period comprised between 3 to 6 months after HTVi. Proposed hypothesis to this fact could be that transfected cells undergo oncogene-induced senescence, apoptosis or immune clearance (senescent cells secrete cytokines that can recruit immune cells, the so-called SASP, i.e. senescence-associated secretory phenotype or immunogenicity derived by GFP[142, 143]).

In accordance to this observation, the 2-HG content, which was elevated just in the *IDH1 R132C*-injected group, was also strongly decreased when compared to the 3 months timepoint (Figure 7.G and Figure 7.E). At 6 months after HTVi, the linear relationship between 2-HG levels and HA^+ cells showed a strongly positive relation with a Pearson correlation coefficient $r = 0.8489$, explaining the robust association between these two variables (Figure 8.F). Additionally, and in line with the previous observations at 3 months after HTVi, I also found that the *IDH1 R132C* was leading to a higher 2-HG content when normalized by the number of transfected cells at 6 months post-HTVi, as shown in Figure 8.G.

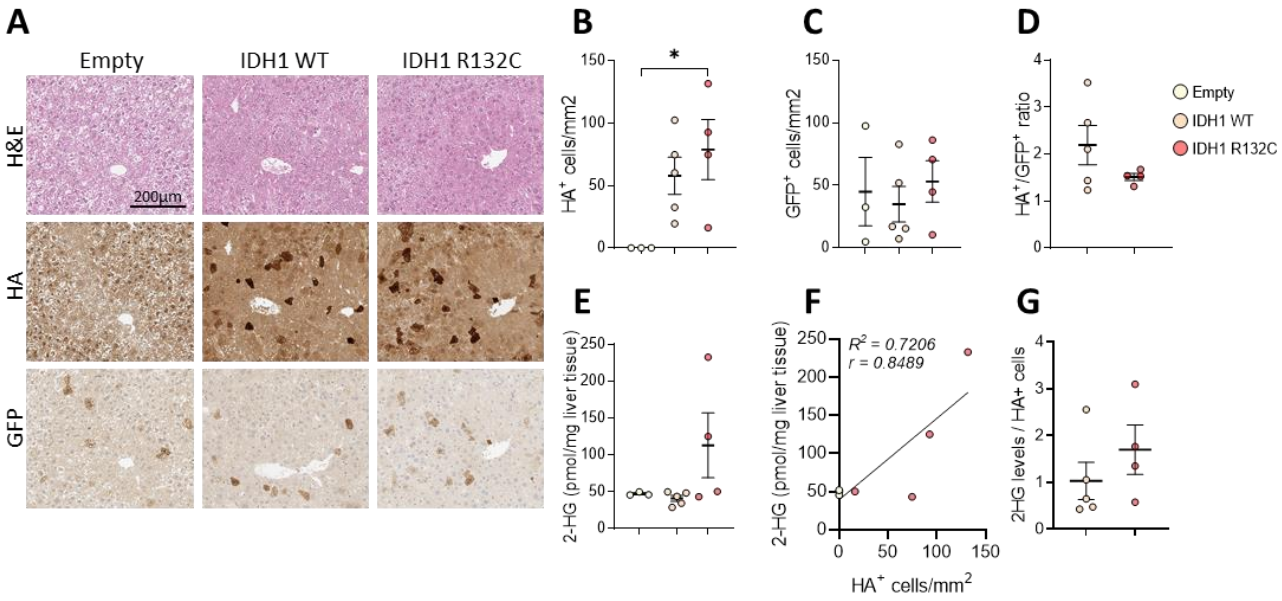

Figure 8. Mutant-*IDH1* leads to 2-HG production after 6 months post-HTVi. (A) Representative pictures from IHC staining of livers injected with corresponding vectors by HTVi. H&E, HA-tag monitoring IDH1 expression and GFP staining shown. Scale bar= 200µm. (B) Quantification of HA-tag and (C) GFP transfected cells by HTVi. (D) Ratio of HA^+/GFP^+ cells show the genes transcribed. (E) 2-HG content in murine liver tissue from animals injected with IDH1-vectors by HTVi and determined by UPLC-MS. (F) Linear relationship between 2-HG levels and HA^+ cells/mm^2. Linear regression (black solid line) displayed. Empty and *IDH1 R132C* groups included. (G) Ratio between 2-HG levels/HA^+ cells indicates the amount of oncometabolite per transfected cell. Data shown as mean ±SEM. Significance determined by one-way analysis of variance with post hoc Tukey´s multiple comparison test. *p<0.05 indicated (B-E, G).

Taken together, these experiments suggest that overexpression of a single *IDH1*-mutant does not drive liver tumorigenesis by means of HTVi, but it rather needs the cooperation with additional genetic alterations to lead to tumor initiation. Furthermore, and most importantly, these data validate the suitability of such a method to both monitor the expression and study the biological and functional role of mutant-*IDH1* in the liver microenvironment *in vivo.*

7.1.3 Mutant-*IDH1* GEMM hepatomegaly restricts the use for HTVi studies

As an alternative approach to the HTVi model to overexpress mutant-*IDH1*, and aiming to further investigating its biological effect in the liver microenvironment in a constitutive manner, I adopted an additional genetic mouse model kindly provided by Prof. Dr. Nabeel Bardeesy (Massachusetts General Hospital in Boston-USA) and previously described by Wu and colleagues[72]. The transgenic mouse model enables the expression of an engineered knock-in allele of *Idh1 R132C* mutation. In this setting, mutant-*Idh1* is endogenously controlled by a floxed stop cassette, which is induced upon Cre recombinase expression driven by the mouse albumin enhancer/promoter (*Alb-Cre* mice) (Figure 9.A-B). Therefore, this model allows the study of the functional effect of *Idh1 R132C* specifically in liver progenitor cells.

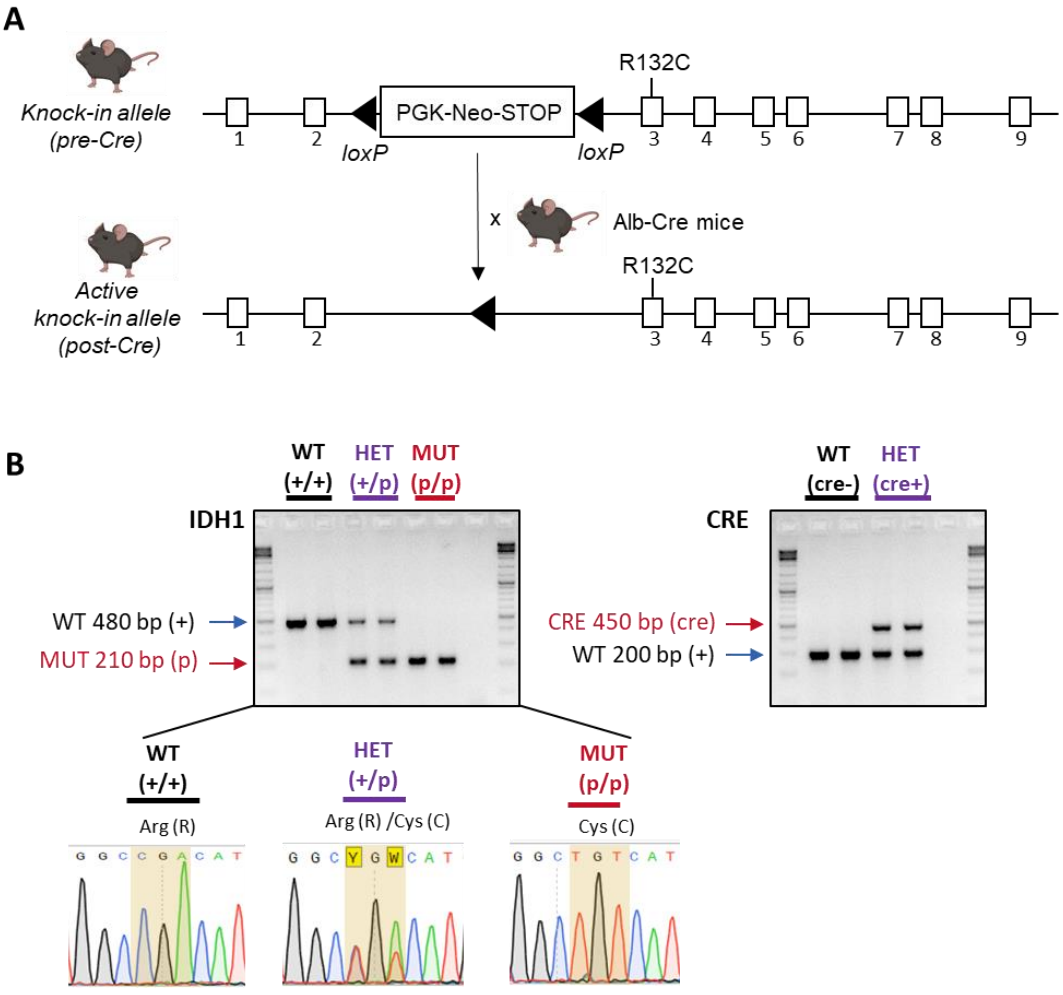

Figure 9. GEMM enables liver-specific expression of mutant *Idh1*. (A) Scheme of resulting *floxed Idh1 R132C* allele upon Albumin-Cre recombinase, enabling expression of mutant-*Idh1* in liver progenitor cells. Modified from Wu, Shi, Dubrot *et al.* Cancer discovery 2022[72]. (B) Agarose gel showing the PCR results for

the *Idh1* and *Albumin Cre* genes from DNA extracted from wild-type (WT), heterozygous (HET) and homozygous (MUT) animals, together with the corresponding Sanger sequencing chromatogram.

To this end, animals heterozygous for the *Idh1* gene (+/p) crossed with the *Alb-Cre* transgenic mice (cre+) exhibiting activated mutant-*Idh1* R132C expression (*Alb-Cre;Idh1*^{R132C}), were sacrificed at 7 to 8 weeks of age. The corresponding cre- animals were used as negative controls (Figure 10.A-B).

Intriguingly, I observed that while there were no differences in body weight, the livers of cre+ animals were markedly enlarged when compared to the respective cre- controls, as shown by a significantly increased liver weight, which correlated with an increased liver to body weight ratio (Figure 10.C-E). However, no differences in the spleen to body weight ratio were detected between groups (Figure 10.F).

In addition, significantly increased serum AST and ALT levels in cre+ livers suggested the presence of hepatic damage. In accordance to these observations, significantly decreased ALP levels indicated that the source of hepatic damage was not resulting from an affected biliary phenotype, but it was rather hepatocyte damage-driven (Figure 10.G-I).

Next, IHC analysis of the collected livers was used to unravel the mechanisms driving the differences between both genotypes. This revealed that cre+ liver specimens stained with H&E displayed comparable hepatic architecture to the cre- livers. Following these observations, no major differences were found in hepatocyte number (HNF4α^{+}cells/mm^{2}) or extent of cholangiocyte differentiation (% CK19^{+}area), although I could observe a slight trend for increased proliferation (Ki67), cell cycle arrest (p21) and apoptosis (cleaved-Caspase 3) in the cre+ livers. Interestingly, these cre+ livers exhibited a minor tendency in increased immune infiltration, which was statistically significant when analysing the number of CD8^{+} Tcells (Figure 10.J).

Altogether, this data confirms the suitability of this genetically engineered mouse model to study the functional relevance of mutant *IDH1* constitutively expressed in the liver microenvironment. However, I hypothesized that the remarkable hepatomegaly found in the cre+ animals could be considered as a technical restriction of the model for HTVi experimental use, for which animals are injected with a volume of plasmid solution according to their body weight (10% body weight). Under those circumstances, the resulting plasmid integration in the liver and consequent experimental output cannot be biologically controlled in an appropriate manner.

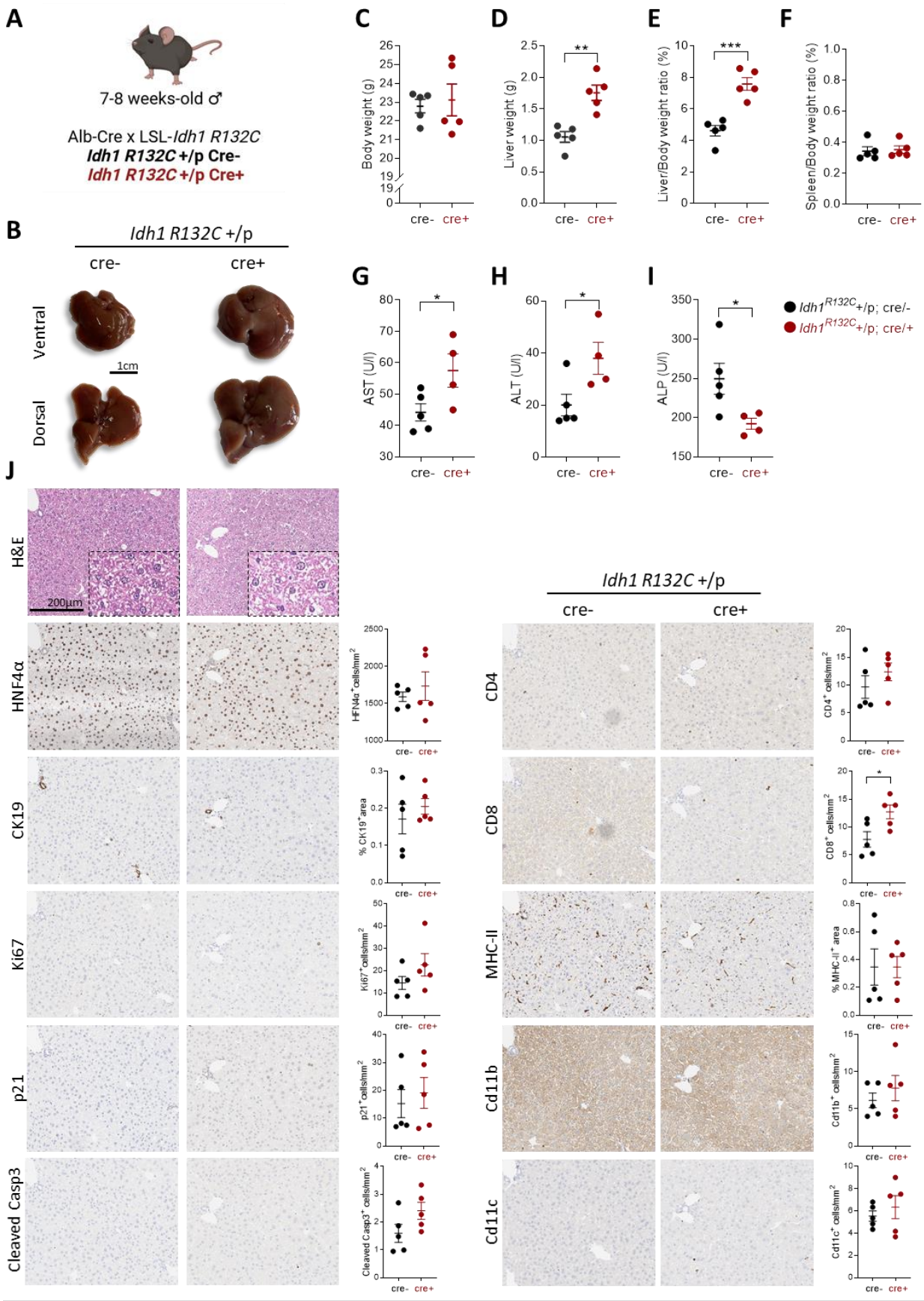
A
7-8 weeks-old ♂
Alb-Cre x LSL-Idh1 R132C
Idh1 R132C +/p Cre-
Idh1 R132C +/p Cre+
B
Idh1 R132C +/p
cre-
cre+
Ventral
Dorsal
1cm
C
Body weight (g)
D
Liver weight (g)
E
Liver/Body weight ratio (%)
F
Spleen/Body weight ratio (%)
G
AST (U/l)
H
ALT (U/l)
I
ALP (U/l)
Idh1R132C+/p; cre/-
Idh1R132C+/p; cre/+
J
H&E
200µm
HNF4α
CK19
Ki67
p21
Cleaved Casp3
CD4
CD8
MHC-II
Cd11b
Cd11c

Figure 10. Constitutive activation of liver-specific mutant *IDH1* leads to hepatomegaly, hepatocyte damage and increased CD8$^+$ T cell infiltration. (A) Genetically engineered mice with liver-specific *Idh1 R132C* are sacrificed at 7 to 8 weeks of age compared to controls. **(B)** Representative liver pictures from both genotypes. Dorsal and ventral view. Scale bar 1 cm. **(C)** Body weight **(D)** Liver weight **(E)** Liver to body weight ratio **(F)** Spleen to body weight ratio. **(G)** Serum levels of AST **(H)** ALT **(I)** ASP in animals from both genotypes. **(J)** Histological characterization of livers from B with corresponding hematoxylin eosin staining (H&E) at high (20X) magnification. Consecutive sections showing HNF4α as well as Cytokeratin-19 (CK19) as a biliary differentiation marker and proliferation marker Ki67, cell cycle arrest marker p21 and apoptosis marker cleaved caspase 3. For immune histological characterization: CD8 and CD4 T cells, antigen presenting cells marker MHC-II, monocyte marker CD11b and CD11c. Scale bars 200µm. QuPath and manual quantification shown. Data shown as mean ±SEM. Significance determined by two-sided unpaired t-test. *p<0.05, **p<0.01 and ***p<0.001 shown. AST: Aspartate Transaminase. ALT: Alanine Aminotransferase. ALP: Alcaline Phosphatase.

In order to verify the suitability of this model for forthcoming experimental purposes using HTVi, I delivered *AKT* overexpression plasmid by HTVi as a model that leads to a clear steatotic phenotype, as previously shown[144]. For this purpose, I injected 7 to 8 weeks old *Alb-Cre;Idh1*^{R132C} animals, and the corresponding cre- controls with a volume according to their body weight, which did not differ between genotypes. I then sacrificed the experimental animals after 3 months, as they did not display any signs of distress (Figure 11.A).

Interestingly, the significant difference in liver weight and liver to body weight ratio between genotypes (cre- and cre+ livers) that was previously shown on baseline conditions, was not observed in animals undergoing HTVi with AKT overexpression plasmid (Figure 11.B-D). Besides this, I could only remark these steatotic features in cre- livers, while cre+ seemed to be protected to develop such traits (Figure 11.C, E). This could be explained by the fact that the %HA$^+$ area (reporter for *AKT* expression) was significantly reduced in cre+ livers when compared to negative controls, indicating less transfection efficiency in cre+ livers (Figure 11. F-H)

These observations corroborated my earlier hypothesis on the potential limitation of using animals from the mouse line *Alb-Cre;Idh1*^{R132C} for HTVi experimental purposes. The main reason is that this type of method bases the volume to be delivered on the body weight of the animals, which in this case does not differ between genotypes (cre- and cre+). Certainly, the remarkable hepatomegaly that these cre+ animals exhibit supposes a technical restriction that needs to be considered, as I showed that the resulting outcome cannot be properly controlled to derive insightful biological conclusions on the role of the genetic factors delivered by HTVi.

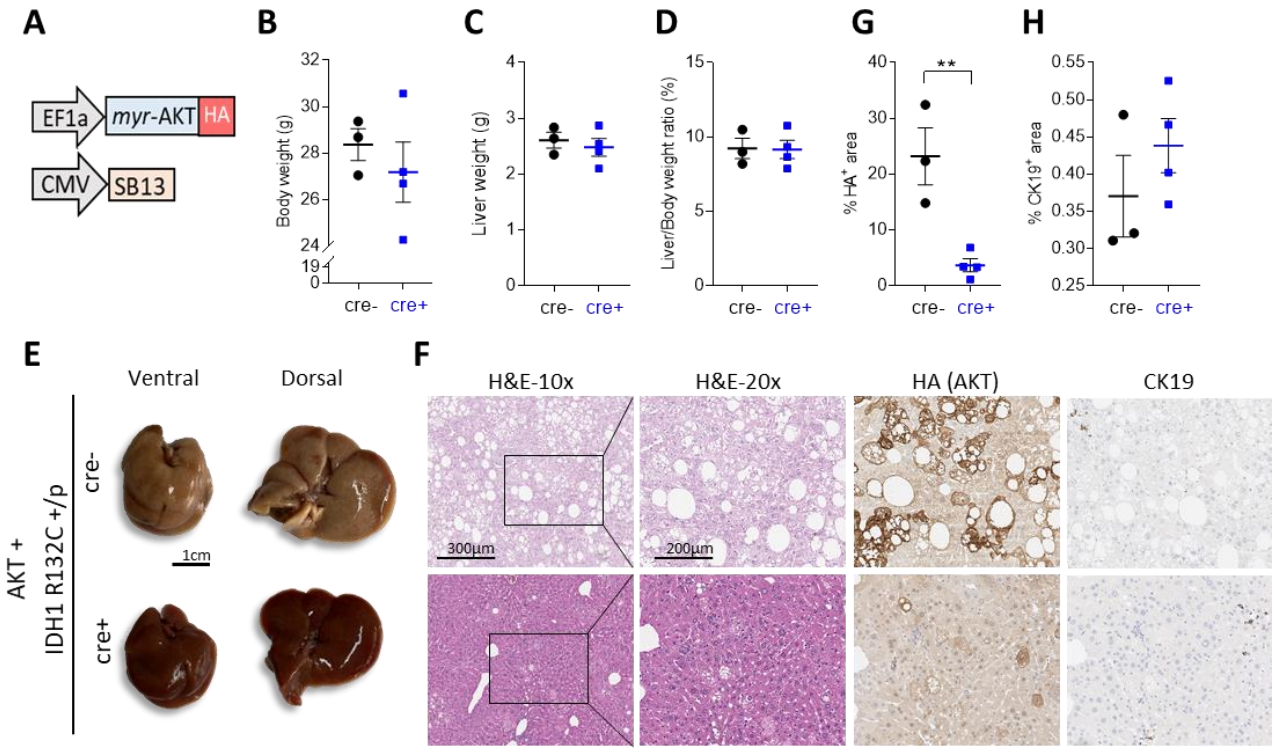

Figure 11. Hepatomegaly derived by constitutive activation of liver-specific mutant *Idh1* restricts the use of this mouse model for HTVi purposes. (A) Scheme of plasmids delivered in 7 to 8 weeks old *Alb-Cre;Idh1*^{R132C} animals. (B) Body weight (C) Liver weight (D) Liver to body weight ratio (G) Percentage of HA-tag positive area (H) Percentage of the biliary marker CK19 positive area in both genotypes. (E) Dorsal and ventral view of livers from both genotypes injected by HTVi with AKT overexpression plasmid. Scale bar 1 cm. (F) Histological characterization of livers from E with corresponding hematoxylin eosin staining (H&E) at low (10X-scale bar 300µm) and high (20X- scale bar 200µm) magnification. Consecutive sections showing HA reporter as well as Cytokeratin-19 (CK19) as a biliary differentiation marker. Data shown as mean ±SEM. Significance determined by two-sided unpaired t-test. ***p*<0.01 shown.

7.2. Cooperation between mutant-*IDH1* and frequent alterations in iCCA

In an effort to further investigate the potential role of mutant-*IDH1* in driving liver tumorigenesis, I aimed to model the genetic tumor heterogeneity of iCCA disease in an experimental *in vivo* setting. For that purpose, I first identified genes previously reported to be altered in iCCA by reviewing literature and the publicly available clinical database cBioPortal[145].

The most commonly observed alterations were found as missense mutations in *KRAS*, deletion of *TP53*, *SMAD4*, *PTEN*, *CDKN2A*[146] and amplification of *MYC* with variable frequencies due to the heterogeneity of the case studies[113]. Moreover, previous studies showed that the Notch pathway is able to control liver development through the modulation of biliary differentiation and ultimately drive cholangiocarcinoma[30] and PI3K/AKT signaling plays a critical role in biliary carcinogenesis and progression[147] (Figure 12.A).

In order to determine the potential cooperation between mutant-IDH1 with oncogenes or tumor suppressors in triggering tumor initiation, transposon-based vectors for gene overexpression (pT3-EF1α-KRASG12D-EGFP, pT3-EF1α- myr-AKT-HA, pT3-EF1α-MYC and PT3-EF1α-Notch ICD-IRES-mCherry) and CRISPR-Cas9 vectors enabling gene knockout (px330-sgTp53, px330-sgPten, px330-sgp16^{INK4} and px300-sgSmad4) were used for HTVi purposes (See Methods 6.1 for details), modelling the genetic alterations of interest (Figure 12.B).

I therefore delivered the single plasmid with oncogene overexpression or tumor suppressors silencing, alone or in combination with *IDH1 R132C*, in 8-weeks old male C57BL/6J mice. The mice were included in a survival analysis up to 6 months, a timepoint that was based on previous experiments in the laboratory and was considered sufficient for gene cooperation to trigger tumorigenesis by means of HTVi (Figure 12.C). Animals reaching this timepoint were then sacrificed and livers were collected and processed for histological analysis.

All the mice reached the timepoint 6 months post-HTVi without showing any signs of distress. Of note, on the macroscopic level, I could observe that in the group of animals injected with *AKT* plasmids, either single or in combination with *IDH1 R132C*, the livers were remarkably enlarged and had a steatotic appearance and correlated with an increased liver weight as shown in Figure 12.D. These observations were in accordance with previous studies in wild-type FVB/N mice[144].

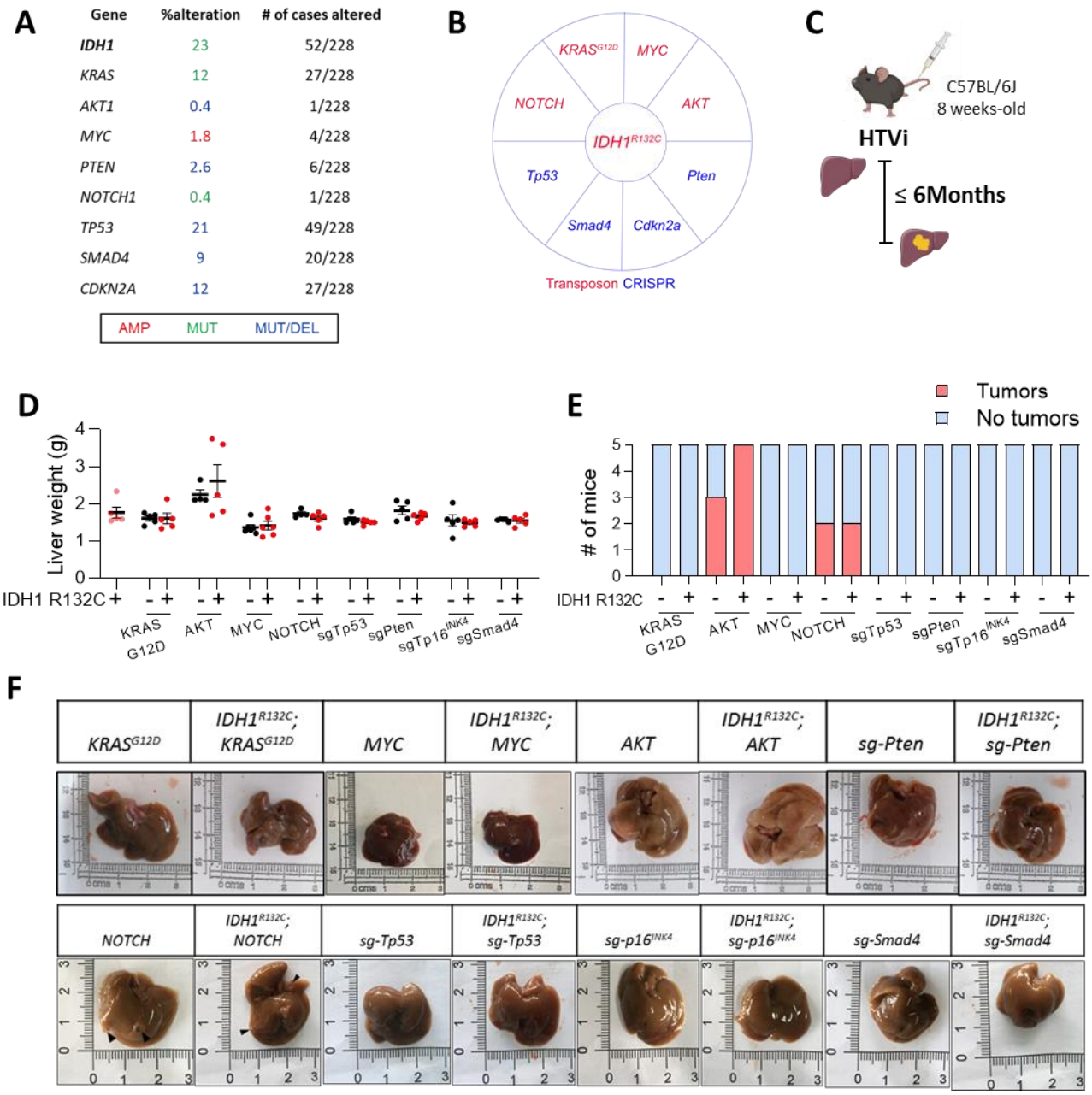

Figure 12. *In vivo* screening identifies potential cooperation between mutant-*IDH1* and frequent genetic alterations in iCCA. (A) Frequency of selected genes altered in iCCA patients from the TCGA, PanCancer Atlas and MSK, Clinical Cancer Research 2018 in cBioPortal. (B) Scheme of plasmid combinations (Transposon-based for overexpression and CRISPR-Cas9 for genetic knockout) delivered by HTVi. (C) Experimental approach showing plasmid delivery in 8-weeks old C57BL/6J male animals and monitored for tumor development up to 6 months, when sacrificed for analysis. (D) Liver weight from animals injected with plasmids from (B) after 6 months after HTVi. (E) Number of mice that developed tumors within 6 months after HTVi. (F) Representative pictures of livers from mice injected with different plasmid combinations and showing macroscopic tumors nodules. Black arrows indicate nodules and tumor masses. Significance determined by two-sided unpaired t-test comparing combination with *IDH1 R132C* – and +. Non-significance not shown (D).

Besides this finding, solid tumor nodules were identified in 60% of the *AKT*-injected mice (3/5 mice), and in 100% of the *AKT/IDH1 R132C* group (5/5 mice). Likewise, I could also recognize some minor cysts with comparable incidence (2/5 mice) in the groups injected with plasmids *NOTCH* and *NOTCH/IDH1 R132C*. Unfortunately, no further alterations or tumor nodules were observed in the rest of the cohorts (Figure 12.E-F).

To further study the impact of genetic alterations in the hepatic microenvironment, I next evaluated the collected livers on a microscopic level by IHC. In order to test the transfection efficiency, that is that the same cell was transfected with the different plasmids, IHC staining of the respective reporters (HA or GFP) contained in the sequence of the plasmids was performed (Figure 13. IHC: HA and GFP). Following previous observations, in those animals with no tumor development after 6 months post-HTVi (*KRAS*, *MYC*, *p53*, *Pten*, $p16^{INK4}$ and *Smad4*), I could remark that HA and GFP, as reporters for *IDH1 R132C* transfection, were barely present. This observation reassured the previously proposed hypothesis of cell clearance by a mechanism not yet determined, which is promoted by the co-expression of oncogenes and tumor suppressors.

In terms of tumor characterization, I focused on the groups injected with *AKT* and *NOTCH* plasmids that were found to exhibit lesions on a macroscopic level. In the case of *NOTCH*-injected mice, I only detected tumors in the liver by IHC in 2/5 mice of the combined *NOTCH/IDH1 R132C* group. This could be explained by the fact that due to the small size of the lesions observed macroscopically, these were lost upon sample collection and further processing. The lesions analyzed displayed a cholangiocellular pattern with expanded tubular structures comprised of aggregated cholangiocytes, positive for CK19 but negative for HNF4α (Figure 13. IHC: CK19, HNFα). Nonetheless, these lesions were negative for HA and GFP staining (*IDH1 R132C*), assuming that these lesions were driven by activation of *NOTCH* signaling and not by *IDH1* R132C.

In the *AKT*-group (both *AKT* and *AKT/IDH1 R132C*) the histopathological study showed that indeed the enlarged livers exhibited hepatocytes with dramatically extended cytoplasm, correlating with previous studies[144] (Figure 13. IHC:H&E). In these groups, I could relate the gross nodules observed on a macroscopic level (Figure 12.F) with tumor-like lesions (big aggregates of abnormal cells group together) negative for CK19. Additionally, I also observed tumors similar to the ones observed in *NOTCH/IDH1 R132C* group, with a cholangiocellular differentiation and positive for CK19 but negative for HNF4α (Figure 13. IHC: CK19, HNFα) showing a smaller tubular pattern. Overexpression of *AKT* in liver sections was corroborated by HA positive staining.

However, in the group injected with *AKT/IDH1 R132C*, as HA-tag is expressed in both plasmids *AKT* (pT3-EF1α-myr-AKT-HA) and *IDH1 R132C* (pT3-EF1a-HA-IDH1 R132C-IRES-EGFP), verifying the expression of GFP contained in the latter was key to discern between lesions driven by a single alteration or the combination of both. In this manner, I could identify that the tumors observed in the group of *AKT/IDH1 R132C* were fully positive for HA, but just a few cells were positive for GFP, concluding that the lesions were mainly driven by the overexpression of *AKT* and only partially by *IDH1 R132C*.

Nevertheless, the *AKT/IDH1 R132C* animals showed an increased liver weight (Figure 12.D) and also elevated serum AST and ALT levels, indicating an aggravated liver damage, as well as more cholangiocellular lesions on the histological level.

Taken together, these results led to the assumption that *IDH1 R132C* overexpression does not intrinsically contribute to tumor development in cooperation with other genetic tumor drivers, but rather fosters an environment that enables and promotes the development and differentiation of tumors in a specific oncogenic setting.

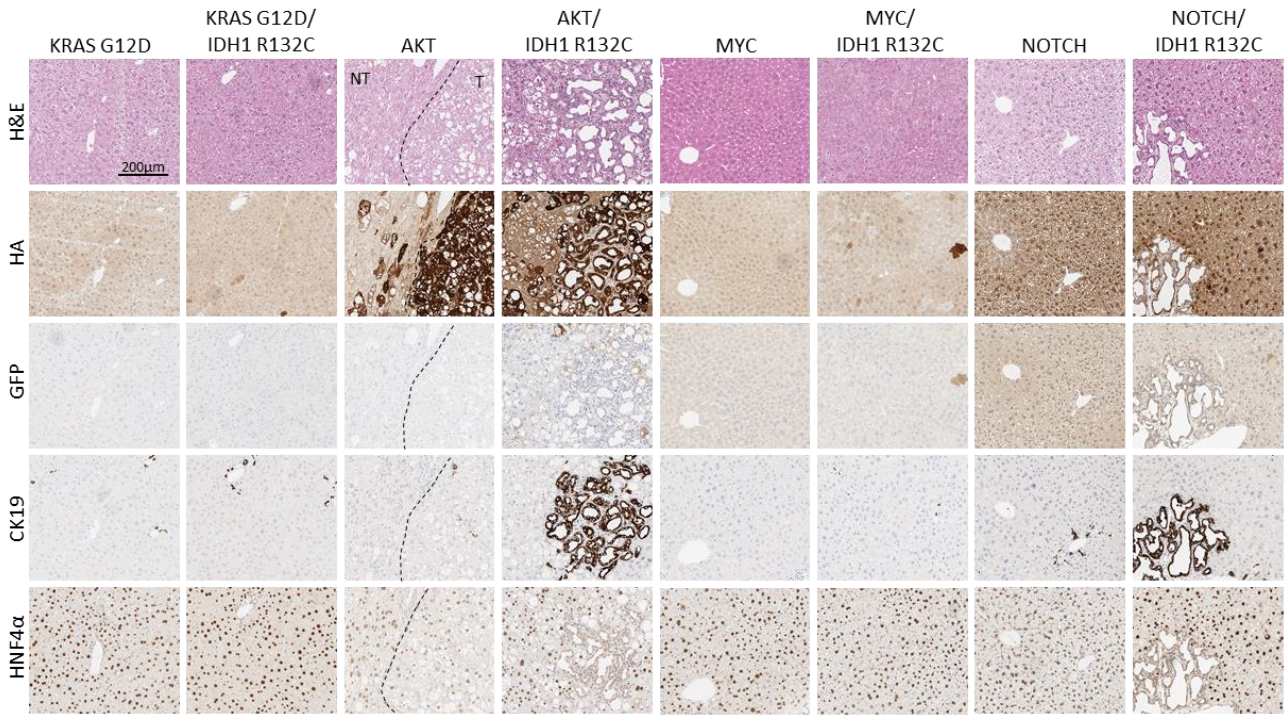

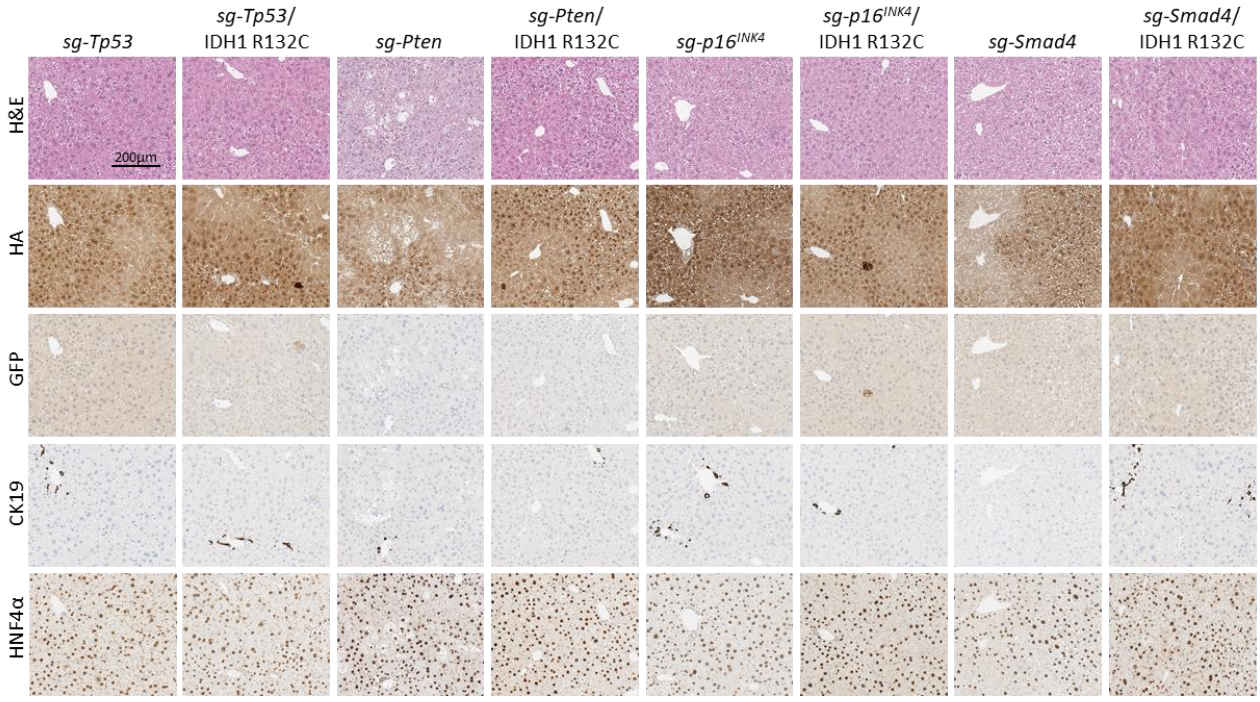

Figure 13. Histopathological analysis of livers resulting from the HTVi *in vivo* screening. Representative pictures from IHC staining of livers injected with corresponding vectors by HTVi. H&E, HA, GFP, CK19 AND HNF4α shown. Scale bar= 200 μm.

7.3 Impact of mutant-*IDH1* in iCCA development

My previous data suggests that *IDH1 R132C* is not decisively involved in driving tumorigenesis, but could potentially promote this process in collaboration with determined genetic alterations. To clarify the role of mutant-*IDH1* in iCCA development, I adopted established spontaneous iCCA models in immunocompetent C57BL/6J mice. With that purpose, I delivered combined plasmids encoding oncogenes and /or tumor suppressors together with mutant-*IDH1* plasmid by HTVi.

7.3.1 Mutant-*IDH1* enhances tumor development in NOTCH/p53-induced iCCA

Following previous work from Ding and colleagues[148], in which they investigated the role of *IDH1 R132C* in promoting iCCA tumorigenesis in combination with both *NOTCH* activation and *p53* loss, I performed HTVi in 8-weeks old C57BL/6J males. Specifically, I combined the overexpression plasmid encoding activated *NOTCH* (PT3-EF1α-Notch ICD-IRES-mCherry), the CRISPR-Cas9 plasmid with a guide RNA targeting p53, leading to *p53* knockout (px330-sgTp53) with either an Empty vector as a control group or the overexpression plasmid for *IDH1 R132C* (pT3-EF1a-HA-IDH1 R132C-IRES-EGFP) in the same saline solution (0.9%NaCl) for injection. Animals were then monitored on survival analysis and livers were harvested when the animals reached terminal stage (Figure 14.A).

Interestingly, in contrast to the Empty vector group (NOTCH/p53/Empty-injected animals), the addition of *IDH1 R132C* significantly accelerated disease progression resulting in a shortened survival of those animals injected with *NOTCH/p53/IDH1 R132C* (Figure 14.B). In my experience, and unlike the timeline of tumor development described in previous work[148], the spontaneous iCCA model led to a median survival of 13.28 weeks (when *IDH1 R132C* is present) and 16.43 weeks (with Empty vector), inducing the development of nodular and necrotic cysts that covered up to 70-90% of the liver parenchyma (Figure 14.F). The divergence between the outcome of these model could be explained by the dosage and different plasmid features used in different experiments, and possibly explained by the employment of two different strains (C57BL/6J vs. FVB/N mice). In terms of liver to body weight ratio, even though I could observe no differences between both groups, the number of tumor nodules was significantly increased and they tend to be smaller in the group injected with *IDH1 R132C*, suggesting a role for mutant-*IDH1* in tumor initiation and development in the context of *NOTCH/p53*-driven cancer (Figure 14.C-E).

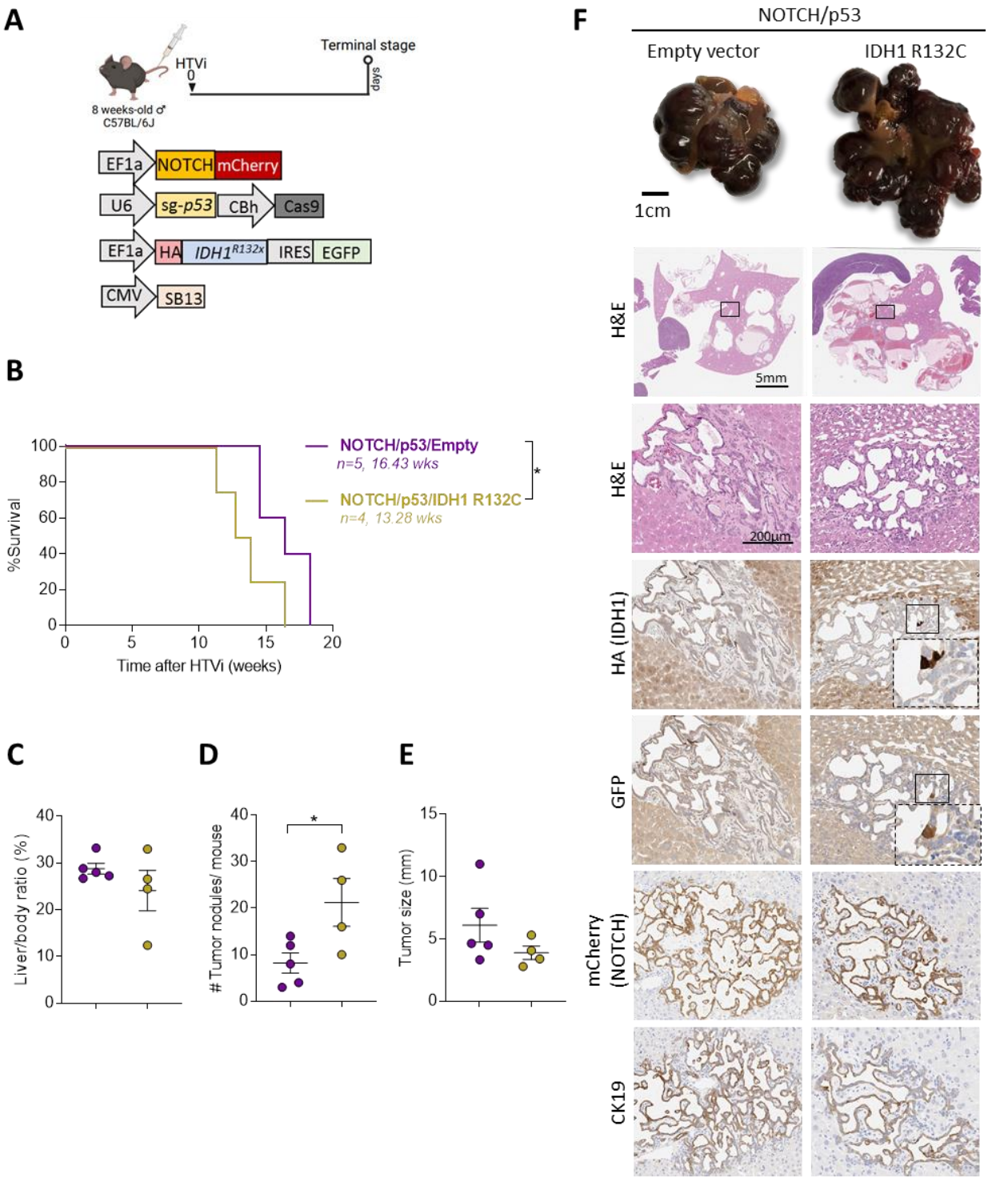

Figure 14. *IDH1 R132C* promotes tumor development in combination with *NOTCH/p53*. (A) Experimental approach and plasmid schemes delivered in 8-weeks old C57BL/6J male animals and monitored for tumor development until reaching terminal stage, when they are sacrificed for analysis. (B) Survival curve of animals from A. Number of animals and median survival shown. (C) Liver to body weight ratio. (D) Total number of tumor nodules per mouse. (E) Average tumor diameter per mouse. (F) Representative pictures from livers from A, and corresponding Hematoxylin eosin staining (H&E) in low

(0.5X) and high (20X) magnification, as well as HA-tag and GFP reporters for IDH1 R132C and mCherry for NOTCH plasmids. Scale bars: 1cm for bright field view, 5mm for 0.5X and 200µm for 20X. Data shown as mean ±SEM. Significance determined by Log-rank Mantel-Cox test for comparisons of Kaplan Meier survival curve (B) and two-sided unpaired t-test (C-E). *$p<0.05$ shown.

Histological analysis showed that the macroscopic cysts from both groups exhibited a ductular phenotype characteristic of iCCA. Remarkably, the tumor development in the *NOTCH/p53/IDH1 R132C* was mainly driven by the activation of *NOTCH* and *p53* loss, as tumor cells strongly expressed mCherry-tagged *NOTCH* (Figure 14. IHC: mCherry). However, *IDH1 R132C* was only present in a few cells that were part of the tumors (Figure 14. IHC: HA(IDH1) and GFP) and almost absent in the non-tumor tissue. This observation suggests a limitation of the HTVi method, in which delivery of several individual plasmids in the same injection, does not imply the uptake of all of them by the same cell, therefore not leading to the transfection and ultimate co-expression of the encoded genes.

Collectively, and in accordance with prior studies mentioned using a similar mouse model, these results further support an important role of *IDH1 R132C* in the iCCA initiation and progression.

7.3.2. *IDH1*-mutant worsens survival and increases tumor burden in KRAS/p53-induced model

To support these observations, I aimed to further investigate the role of mutant-*IDH1* in iCCA development by employing a previously described *KRAS/p53*-induced iCCA model[82].

With this aim, I injected 8-weeks old C57BL/6J male animals by HTVi with plasmids overexpressing *KRAS G12D* mutation (pT3-EF1α-KRAS G12D-EGFP) and CRISPR-Cas9 vectors for *p53* loss (px330-sgTp53) which results in a mean survival of 30 days post-HTVi. In addition to *KRAS/p53*, I included either Empty vector (*KRAS/p53/Empty*) as technical control group and *IDH1 WT* (*KRAS/p53/IDH1 WT*), which I considered as a biological control for mutant-*IDH1*. Moreover, *IDH1 R132C* mutation (*KRAS/p53/IDH1 R132C*) was used as the most frequent mutation in iCCA and *IDH1 R132H*, which is mainly associated with glioma, was included to compare the biological impact derived by a different amino acid substitution (*KRAS/p53/IDH1 R132H*). Following HTVi, animals were monitored for tumor development and livers were harvested when animals reached terminal stage (Figure 15.A)

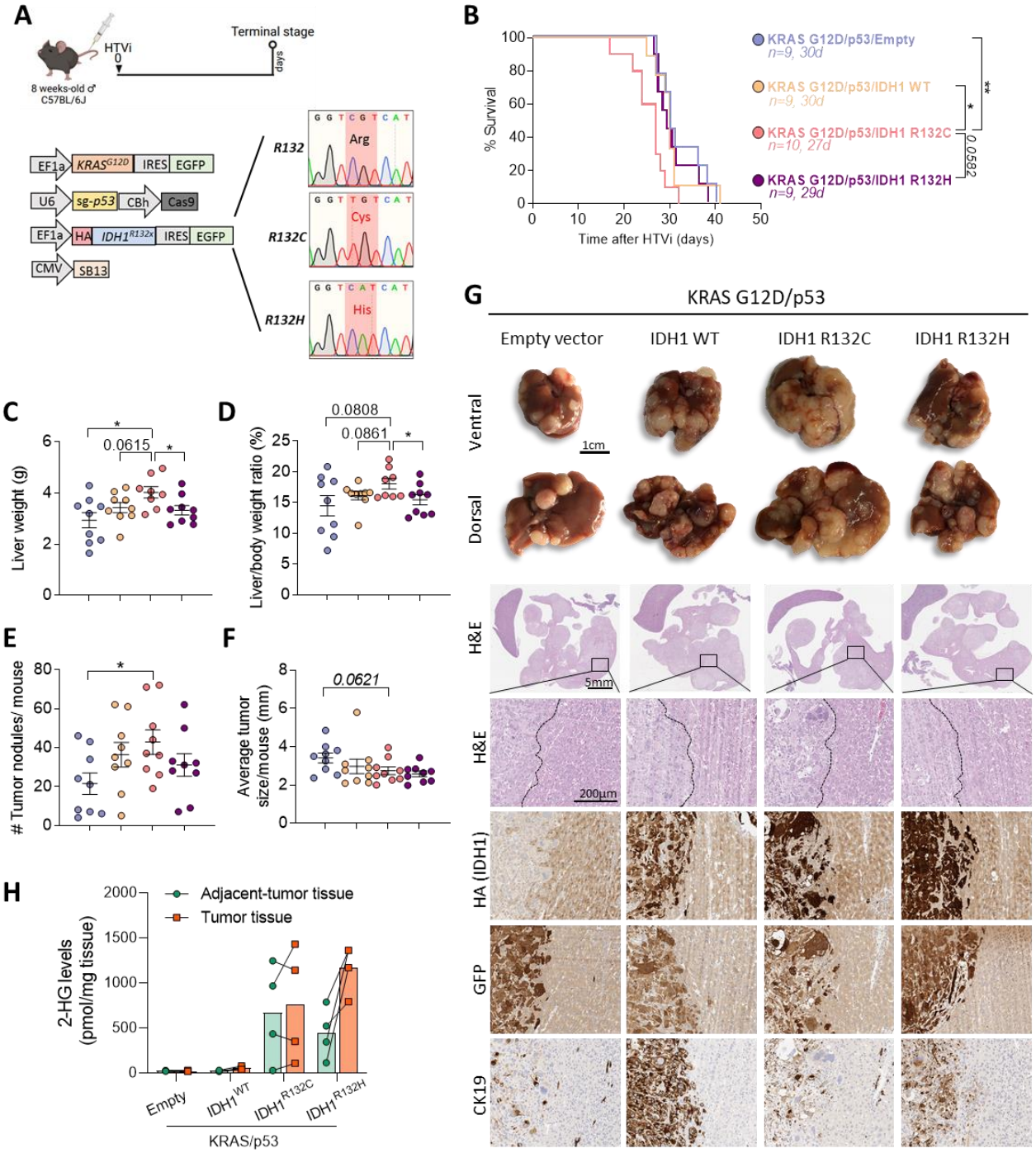

Figure 15. *IDH1 R132C* worsens *KRAS/p53*-induced iCCA development *in vivo*. (A) Experimental approach showing delivery of plasmids by HTVi in 8-weeks old C57BL/6J male animals and monitored for tumor development until reaching terminal stage, when they are sacrificed for analysis. Scheme of plasmids indicated. Sanger sequencing chromatogram corresponding to amino acid substitution leading to *IDH1 WT*, *IDH1 R132C* or *IDH1 R132H*. (B) Survival curve of animals from A. Number of animals and median survival shown. (C) Liver weight. (D) Liver to body weight ratio. (E) Total number of tumor nodules and (F) average tumor diameter per mouse. (G) Representative pictures from livers from A. Dorsal and ventral view. Scale bars 1cm. Corresponding hematoxylin eosin staining (H&E) in two different magnifications and consecutive

sections showing HA-tag for *IDH1* vectors and GFP for *KRAS* and/or *IDH1*, as well as Cytokeratin-19 (CK19) as a biliary differentiation marker. Scale bars 5mm and 200µm. (H) HPLC-MS analysis of 2-Hydroxyglutarate (2-HG) levels in adjacent non-tumor and tumor tissue. Data shown as mean ±SEM. Significance determined by Log-rank Mantel-Cox test for comparisons of Kaplan Meier survival curve (B) and one-way ANOVA with the post-hoc Tukey´s multiple comparison test (C-F). 0.1<p<0.05, *p<0.05 and **p<0.01 shown.

Important to note is that due to the prompt tumorigenesis of this model (median survival 30 days), even slight effects in survival infer a notable biological effect. Strikingly, I observed that animals injected with *KRAS/p53/IDH1 R132C* displayed an earlier tumor onset which led to a significantly decreased survival when compared to the control groups and the additional mutant-*IDH1* group *KRAS/p53/IDH1 R132H* (Figure 15.B).

Similar variances were observed in the livers on a macroscopic level (Figure 15.C-D), which exhibited a significant increase in the total number of tumor nodules with a tendency to be decreased in size, proposing a key role of *IDH1 R132C* in accelerating the tumor initiation rather than progression. Regarding the control groups (Empty vector and *IDH1 WT*), even though animals from both groups showed the identical median survival, I could observe differences in the tumor incidence as well as the size of these nodules (Figure 15.E-F), suggesting that the overexpression of *IDH1 WT* would have additional effects. This observation corroborates the suitability of including the Empty vector group in the experimental setting, considering it as a baseline for further interpretation of the data.

Histological analysis of consecutive liver sections validated the expression of the *IDH1* and *KRAS* vectors in the *IDH1*-injected groups by IHC co-staining of HA-tag and GFP, and just GFP in the *KRAS/p53/Empty* group. The expression of the plasmid reporters was obvious in the tumor areas, and scarce in the adjacent non-tumor tissue (Figure 15.G. IHC: HA(IDH1) and GFP). In the former case, that is animals injected with the combination of *KRAS/p53/IDH1* plasmids, some of the tumors were negative for HA-tag, meaning that these tumors did not incorporate the IDH1 plasmid, and were just driven by the cooperation between *KRAS* and *p53*. This observation highlighted the importance of corroborating the delivery and expression of plasmids. As expected, the positive CK19 staining confirmed the biliary phenotype of these tumor areas (Figure 15.G. IHC: CK19).

In line with previous observations, I confirmed the functional activity of mutant-*IDH1* by an increase in the 2-HG content in both the adjacent non-tumor and tumor tissue of the mutant-*IDH1*-injected animals. In contrast, and in accordance to my expectations, the technical (Empty) and

biological controls (*IDH1 WT*) showed baseline levels of 2-HG production (Figure 15.H). Interestingly, when comparing the 2-HG levels with my previous data on mutant-*IDH1* single injections (Figure 7.G and Figure 8.D), I observed that the 2-HG content was increased 3-fold, suggesting that the alteration of determined genetic alterations boosts the biological effect of mutant-*IDH1* by driving the overgrowth and proliferation of transfected cells.

7.3.3 *IDH1 R132C* leads to an increased metastatic spread in KRAS/p53-induced model

In addition to the data above, I had a striking observation in the *KRAS/p53*-induced iCCA: the presence of solid tumor-like structures arising from the pancreatic tissue (Figure 16.A. IHC: H&E). In order to clarify the nature of this tissue, IHC staining of the plasmid reporters was performed. Then, I could confirm the expression of both HA-tag and GFP in the *IDH1*-injected animals, and just GFP in the Empty vector group. In addition, positive CK19 staining in serial liver cuts revealed the biliary phenotype of the GFP^+ and HA^+GFP^+ positive cells that were part of these structures (Figure 16.A. IHC: HA(IDH1), GFP and CK19).

Based on this data, and taking into consideration that the literature indicates that the plasmid delivery by HTVi occurs accurately and solely in hepatocytes, I assumed that the *KRAS/p53*-induced malignant cells acquired the ability to migrate and invade the surrounding pancreatic tissue at the terminal stage. Next, I quantified the metastatic tumors per condition, revealing that the invasive phenotype was magnified by the addition of *IDH1 R132C* in the *KRAS/p53* model, leading to the spreading of tumor cells that was present in all the individual animals, belonging to this group. Similar observations were made in the *KRAS/p53/IDH1 R132H* group with nearly 90% of the mice showing this feature, and to a lesser extent in the control groups (Figure 15.B). To show the metastatic spread of invading tumor cells, I quantified the magnitude of invasion and remarked that the *KRAS/p53/IDH1 R132C* group showed a significant increase in the metastatic area when compared to the Empty control (Figure 16.C).

Collectively, my results led to the assumption that *IDH1 R132C* plays a role in promoting the tumor development of *KRAS/p53*-induced iCCA, enhancing the migration and invasion of tumor cells.

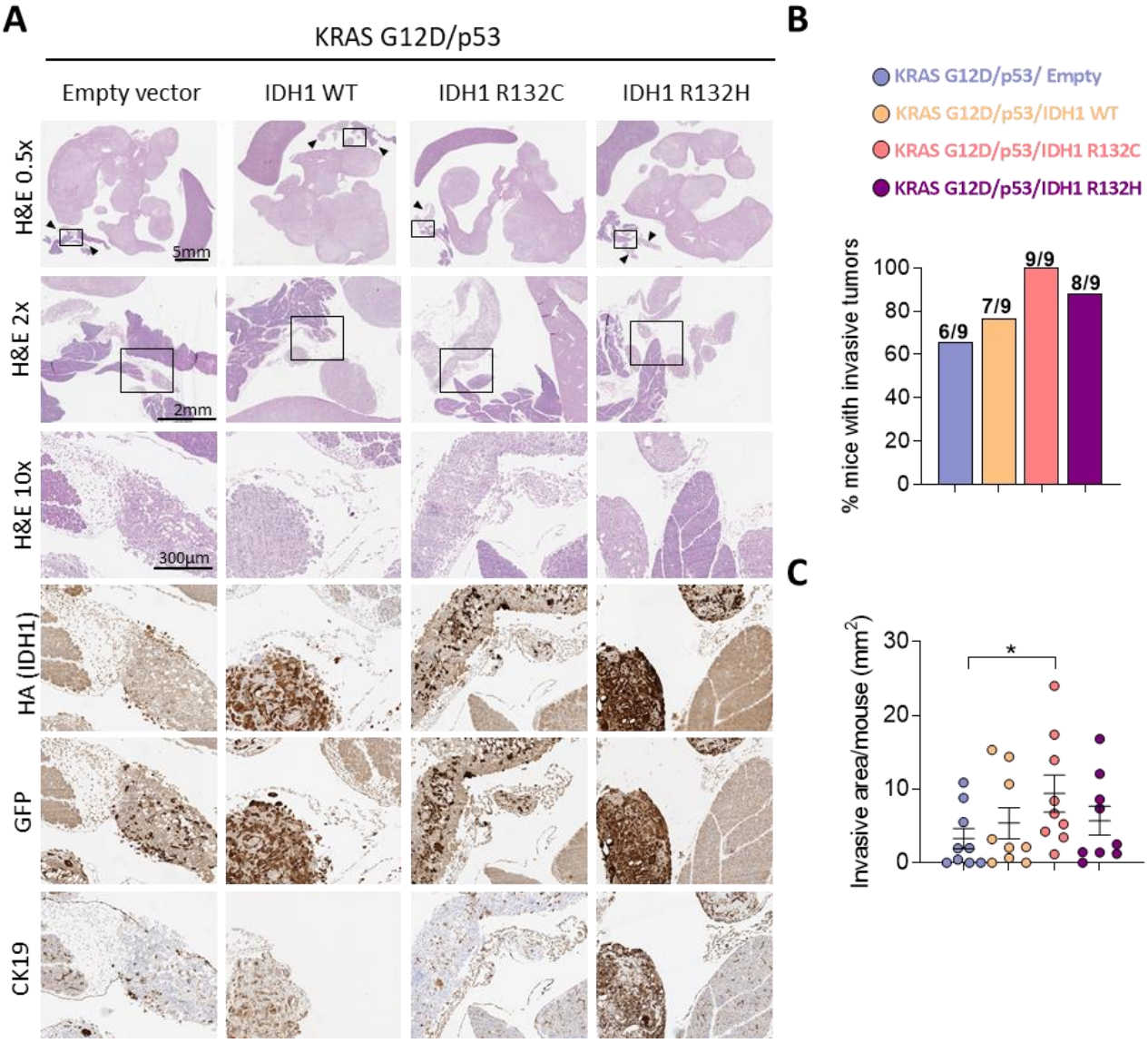

Figure 16. *IDH1 R132C* amplifies tumor cell migration and invasion of the pancreatic tissue in the *KRAS/p53*-induced iCCA model. (A) Representative pictures of liver sections stained with Hematoxilyn eosin (H&E) staining in different magnifications (0.5X, 2X, 10X) focusing on the extrahepatic metastasis. Corresponding staining reporting *IDH1* expression (HA-tag and GFP) and *KRAS* expression (GFP), as well as biliary differentiation marker Cytokeratin-19 (CK19). Scale bars 5 mm (0.5X), 2 mm (2X) and 300 µm (10X) indicated. (B) Histogram showing incidence of invasive tumors in the extrahepatic tissue in the different groups. (C) Total invasive area per animal in mice injected by HTVi at terminal stage. Data shown as mean ±SEM. Significance determined by one-way ANOVA with the post-hoc Tukey´s multiple comparison test (C). *p<0.05 shown.

7.3.4 *IDH1 R132C* promotes molecular pathways involved in aggressiveness, inflammation and metabolic processes

In order to understand the molecular mechanisms by which *IDH1 R132C* exerts an effect in survival and increased invasiveness, I, in collaboration with the NGS Core Facility and Feng Han from the German Cancer Research Center in Heidelberg, and Detian Yuan in Shandong University in China, performed bulk-RNA sequencing of tumors from each of the different *KRAS/p53*-driven models, and included the respective surrounding non-affected tissue.

Principal component analysis (PCA) of non-affected tissue showed clear differences in the transcriptional profiles between technical and biological controls and the *IDH1* mutants. Interestingly, while the Empty and *IDH1 WT* groups clustered together, indicating the comparability between technical and biological controls, *IDH1 R132C* and *IDH1 R132H* formed their own clusters, that separated from each other, suggesting a unique gene expression profile in the context of each mutation in non-affected tissue. This data would be in line with the effects previously shown in survival analysis and migratory abilities of mutant-*IDH1* compared to controls (Figures 17.A, 15.B and 16). Gene Set Enrichment Analysis (GSEA) based on the Normalized enrichment score (NES) and p-adj<0.05, comparing non-affected tissue from *IDH1 R132C* and *IDH1 WT* showed an up-regulation of Hallmark gene sets involved in essential pathways driving cellular proliferation and migration (EMT, KRAS signalling, MYC targets, Hypoxia and Angiogenesis, P53 Pathway), cell cycle and cell division (G2M Checkpoint, E2F Targets, Mitotic Spindle, Myogenesis,) inflammation (TNFα-Signaling via NF-κB, Inflammatory Response, IL2-STAT5 Signaling) and metabolic pathways (Glycolysis). Downregulated Hallmark gene sets were involved in metabolic processes (Bile Acid Metabolism, Fatty Acid Metabolism and Cholesterol Homeostasis), oxidation (Peroxisome and Oxidative Phosphorylation) and immune-related pathways (Complement and IFNα-Response) (Figure 17.B).

In contrast to non-affected tissues, PCA analysis from tumor tissues revealed that the transcriptional profiles of the Empty group clustered apart and differed from the rest of the groups. In turn, all the *IDH1*-derived tumors formed a common cluster, indicating that tumors at terminal stage might display similar molecular features (Figure 17.C). GSEA based on NES and p-adj<0.05 showed that the upregulated pathways were involved in inflammation (IL6-JAK-STAT3 Signaling, Inflammatory Response and Complement), KRAS Signaling and Xenobiotic Metabolism. Downregulated gene sets included pathways that were upregulated in the non-affected tissue, indicating the divergent transcriptional profiles that the two different tissues types exhibited.

Consequently, tumor tissue from IDH1 R132C compared to WT control revealed a downregulation of genes involved in cell cycle and cell division (E2F Targets, G2M Checkpoint, Mitotic Spindle) and proliferation (MYC Targets), oxidation and metabolic processes (MTORC1 Signaling, Oxidative Phosphorylation, Fatty Acid Metabolism, Adipogenesis, Peroxisome and Glycolysis) and immune pathways (TNFα-signaling via NF-κB).

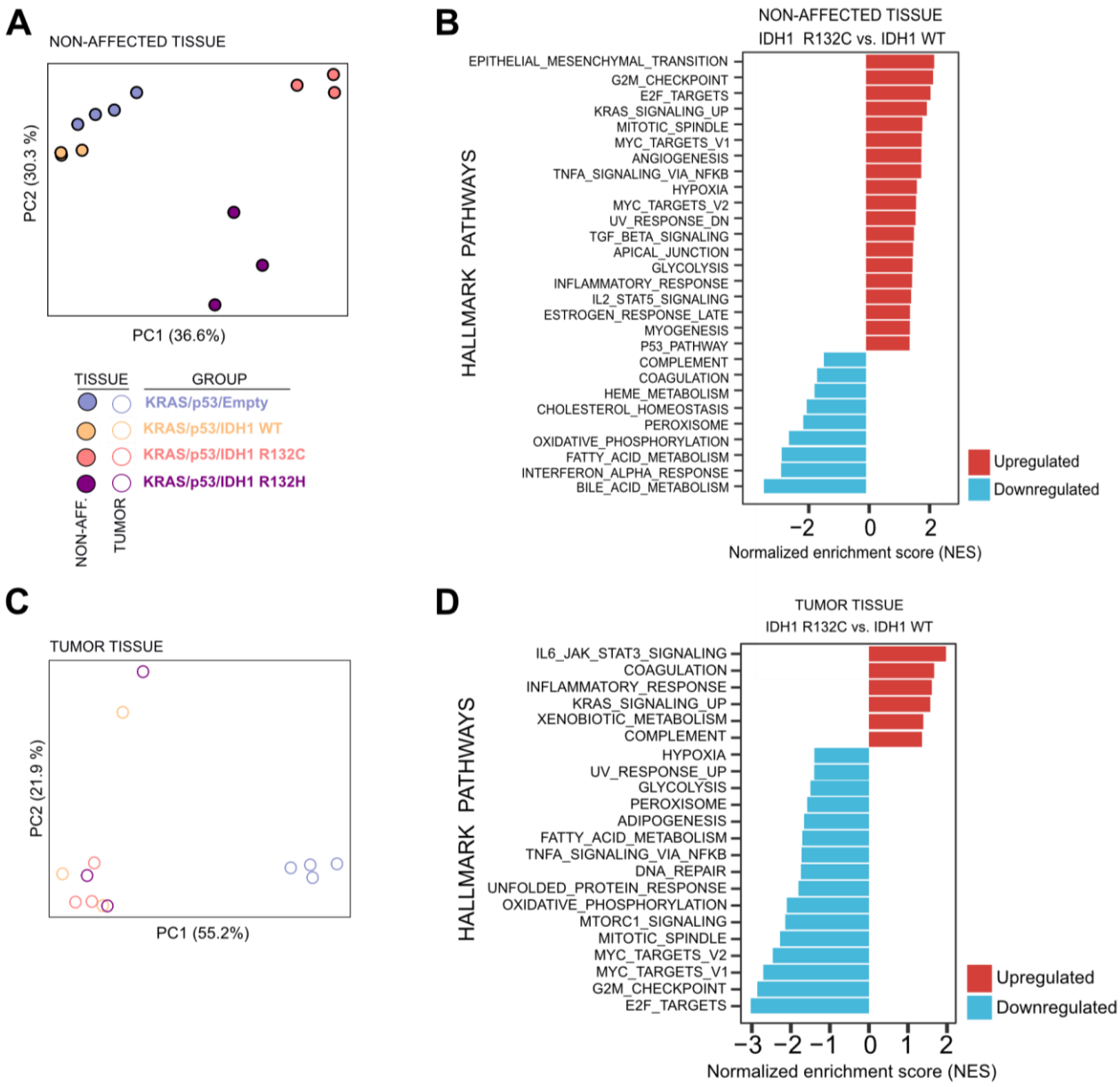

Figure 17. Bulk-RNA-sequencing identifies *IDH1 R132C* to shape the TIME by increasing aggressiveness, inflammation and metabolism. (A) PCA from gene expression analysis from non-affected tissue. (B) GSEA from Hallmark gene set based on NES and p-adj<0.05. Upregulated and downregulated hallmark pathways shown. C. PCA from gene expression analysis from tumor tissue. D. GSEA from Hallmark gene set based on NES and p-adj<0.05. Upregulated and downregulated hallmark pathways shown.

In summary, this data further demonstrated that *IDH1 R132C* plays a pro-tumorigenic role in the *KRAS/p53*-induced iCCA model. On a transcriptional level at terminal stage, *IDH1 R132C* displays a remodelling effect in the non-affected microenvironment tissue, rather than on the tumor cells. This is driven by an increased cell division and proliferation, as well as the upregulation of pathways involved in migration and invasiveness. Moreover, this data does not only point out to an immunomodulatory effect but also a metabolic effect in the different cellular compartments, potentially driven by 2-HG as the main effector derived from *IDH1* mutation.

7.3.5 *IDH1 R132C* accelerates tumorigenesis in *KRAS/p53*-induced model

To validate my previous results and further understand the impact of mutant-*IDH1* in the tumor growth, I harvested the livers from the different groups at an earlier timepoint: 21 days post-HTVi (Figure 18.A). Notably, one animal from the *KRAS/p53/IDH1 R132C* group reached terminal stage and had to be sacrificed before the experimental endpoint, highlighting the significant effect of this mutation in enhancing tumorigenesis. The accelerated tumorigenesis previously reported in the survival analysis was evidenced macroscopically by a significantly increased tumor incidence in the *KRAS/p53/IDH1 R132C*-injected animals at this timepoint. Accordingly, liver weight and liver body weight ratio were remarkably increased in the *KRAS/p53/IDH1 R132C* cohort when compared to the rest of the groups (Figure 18.B-D), correlating with an obvious and higher number of tumor nodules which exhibited a larger diameter (Figure 18.E).

Surprisingly, even though the 2-HG content derived from the additional mutant-*IDH1* (*IDH1 R132H*) had similar levels to the *IDH1 R132C* at terminal stage (Figure 18.E), the obvious differences observed between these two groups suggested that the single amino acid substitution led to distinct mechanistic underpinnings in the context of *KRAS/p53*-induced iCCA.

Further assessment of liver damage parameters in the serum of the experimental animals corroborated the altered liver function, shown by a significant increase in the levels of ALT, AST and ALP released enzymes in the *KRAS/p53/IDH1 R132C* group, following the observations in tumor incidence (Figure 18.F-H).

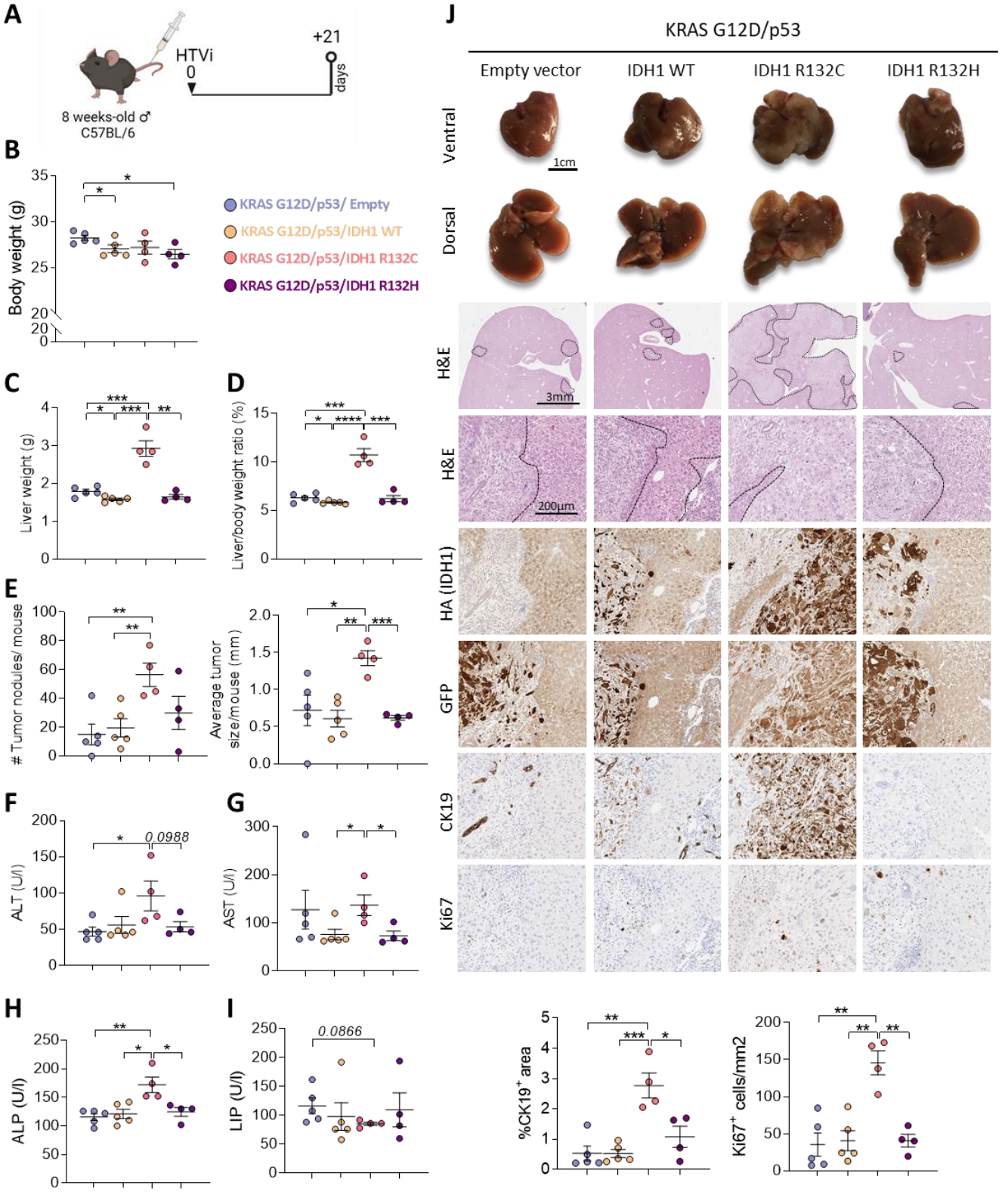
A
HTVi
0
+21
days
8 weeks-old ♂
C57BL/6
B
Body weight (g)
KRAS G12D/p53/ Empty
KRAS G12D/p53/IDH1 WT
KRAS G12D/p53/IDH1 R132C
KRAS G12D/p53/IDH1 R132H
C
Liver weight (g)
D
Liver/body weight ratio (%)
E
Tumor nodules/ mouse
Average tumor size/mouse (mm)
F
ALT (U/l)
0.0988
G
AST (U/l)
H
ALP (U/l)
I
LIP (U/l)
0.0866
J
KRAS G12D/p53
Empty vector
IDH1 WT
IDH1 R132C
IDH1 R132H
Ventral
Dorsal
1cm
H&E
3mm
H&E
200µm
HA (IDH1)
GFP
CK19
Ki67
%CK19+ area
Ki67+ cells/mm2

Figure 18. *IDH1 R132C* accelerates tumor initiation of *KRAS/p53*-driven iCCA. (A) Experimental set up: 8-weeks old C57BL/6J male animals are injected by HTVi and culled at 21 days-post HTVi. (B) Body weight per mouse. (C) Liver weight per mouse. (D) Percentage showing the liver to body weight ratio. (E) Tumor incidence showing the number of tumor nodules as well as the mean average size of these per mouse. (F) Serum ALT, (G) AST, (H) ALP and (I) LIP levels in mice injected by HTVi with different plasmid combinations. (J) Representative pictures from livers from A. Dorsal and ventral view. Scale bars 1 cm. Corresponding hematoxylin eosin staining (H&E) at low (1X) and high (20X) magnification. Consecutive sections showing HA-tag for *IDH1* vectors and GFP for *KRAS* and/or *IDH1*, as well as Cytokeratin-19 (CK19) as a biliary differentiation marker and proliferation marker Ki67. Scale bars 3 mm (1X) and 200 µm (20X). QuPath quantification of percentage of positive CK19 area, and number of positive Ki67 cells. Data shown as mean ±SEM. Significance determined by one-way ANOVA with the post-hoc Tukey´s multiple comparison test (B-J). 0.1<p<0.05, *p<0.05, **p<0.01, ***p<0.001 and ****p<0.0001 shown. ALT: Alanine Aminotransferase. AST: Aspartate Transaminase. ALP: Alcaline Phosphatase. LIP: Lipase.

In addition, to verify the effect in metastatic spread and invasion of the pancreatic tissue, I analysed the levels of lipase in serum. Elevated lipase levels indicate that dying pancreatic tissue is occurring. However, in contrast to my predicted outcome, these levels tended to decrease in the *KRAS/p53/IDH1 R132C* group, indicating that the pancreatic damage does not necessarily need to happen during invasion (Figure 18.I). In this regard, I could not observe the explicit metastatic spread and the solid structures affecting extrahepatic tissue, as compared to terminal stage livers. At this timepoint, I noticed randomly disseminated $HA^{+}GFP^{+}CK19^{+}$ cells in the pancreatic tissue and only in animals injected with *KRAS/p53/IDH1 R132C.* As this group exhibited a significantly higher tumor load compared to the rest of the groups, it is reasonable to propose that the metastatic spread takes place once the tumor has been established and progressed to certain stage with a higher ability to migrate.

Additionally, and in accordance to previous results, I validated the plasmid delivery by staining of serial liver sections with HA-tag and GFP on a histological level. Besides, quantification of CK19 positive area as well as number of proliferating cells by positivity of Ki67 IHC marker, confirmed the previous observations that *IDH1 R132C* accelerates tumor initiation in the context of *KRAS/p53*-driven iCCA (Figure 18.J).

7.3.6 *IDH1 R132C* increases immune-related molecular pathways in *KRAS/p53*-iCCA

In order to understand the mutant-*IDH1* remodelling effect on a transcriptional level, I in collaboration with the NGS Core Facility and Feng Han from the German Cancer Research Center in Heidelberg, performed RNA-sequencing analysis from non-affected tissue at 21-days post-HTVi. This revealed striking differences in the gene expression profiles between the groups.

PCA analysis indicated once more that control groups (Empty and *IDH1 WT*) clustered together. At this timepoint, also *IDH1 R132H* seemed to cluster with control groups, showing that the transcriptional profiles of these surrounding non-tumor tissues might display similar molecular states, which would be in line with the homogeneous tumor load in these groups. Replicates of *IDH1 R132C*-derived non-tumor tissues clustered together, but were interestingly distinct from the rest of the groups, although slightly close to some *IDH1 R132H* samples (Figure 19.A). GSEA of Hallmark genes indicated upregulated pathways in *IDH1 R132C* compared to *IDH1 WT* which were involved in immune response (IL-6-JAK-STAT3 Signaling, INF-γ Response, Inflammatory Response, TNF-α Signaling via NK-κB) and cell proliferation and invasion (EMT, KRAS Signaling, Mitotic Spindle, E2F targets and G2M Checkpoint) (Figure 19.B). Moreover, unsupervised Gene Ontology (GO) pathway analysis indicated that mitochondrial processes were suppressed ("inner mitochondrial membrane protein complex" and "mitochondrial protein-containing complex") in the *IDH1 R132C* group. Also, *IDH1 R132C* exerted an immunomodulatory effect by upregulating immune response pathways ("neutrophil migration", "granulocyte migration", "myeloid leukocyte migration", "leukocyte chemotaxis" and "defense response to bacterium") and increased cell-cell communication ("cell adhesion molecule binding", "actin binding", "extracellular matrix" and "receptor ligand activity") (Figure 19.C)

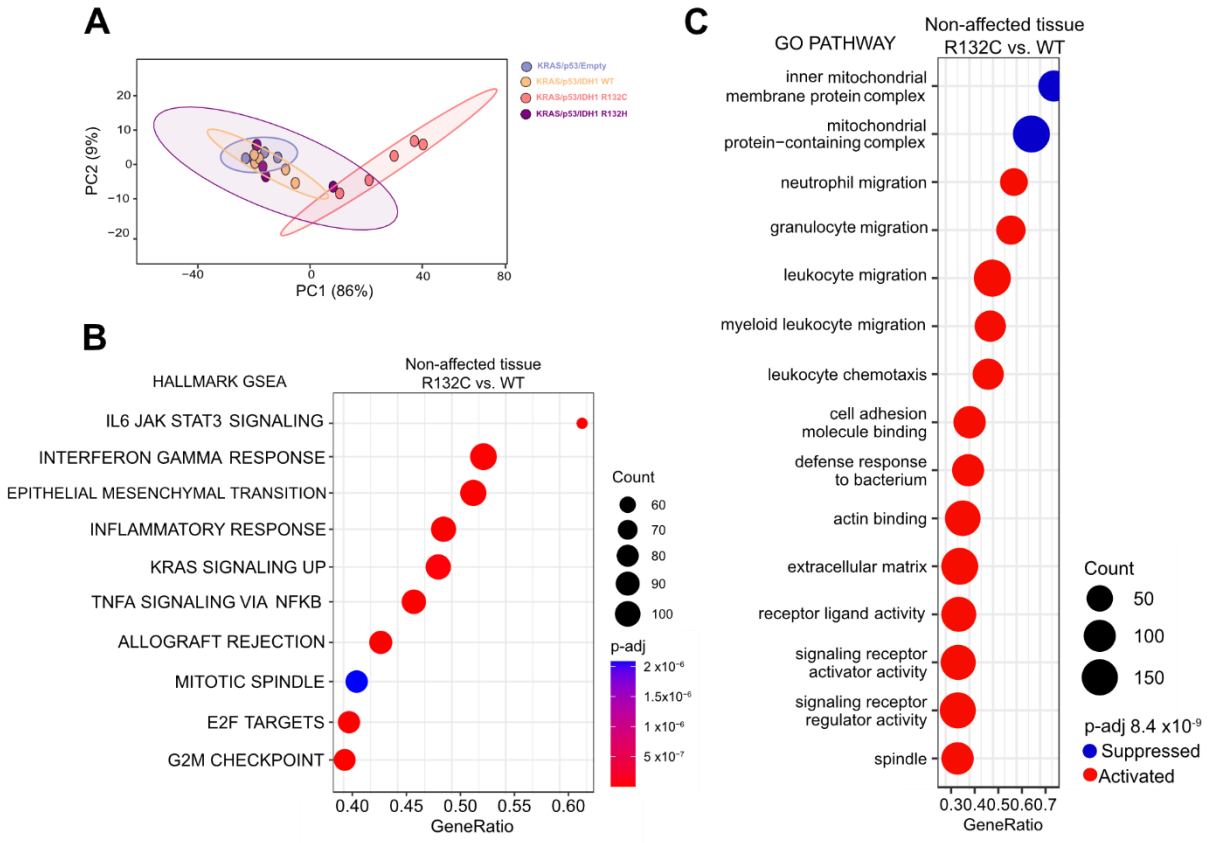

Figure 19. *IDH1 R132C* promotes molecular pathways involved in immune response and cell proliferation. (A) PCA analysis from non-affected surrounding tissue of animals injected with different plasmid combinations at 21 days post-HTVi. (B) GSEA of Hallmark gene sets from *IDH R132C* compared to *IDH1 WT*. Count and p-adjusted indicated. (C) GO pathway analysis showing supressed and activated transcriptional profiles. Gene count and p-adjusted (p-adj) indicated.

Overall, this data further demonstrates that *IDH1 R132C* not only plays a role in promoting cholangiocarcinogenesis (enhancing cell proliferation and invasiveness), but also displays an immunomodulatory effect in the liver microenvironment that might contribute to this pro-tumorigenic effect.

7.3.7 *IDH1 R132C* reshapes the immune microenvironment and leads to an enrichment of the myeloid compartment

My previous data indicated a remodelling effect of *IDH1 R132C* in the non-affected adjacent tissue and an upregulation of GO pathways related to myeloid infiltration. These results prompted me to further understand the relevance of *IDH1 R132C* in tumor development and the potential role in shaping the TIME of *KRAS/p53*-driven iCCA. With that purpose, I in collaboration with Dominik Vonficht from the German Cancer Research Center in Heidelberg analysed in depth the immune compartment using multiparametric spectral flow cytometry.

For that purpose, I collected the livers from mice injected with different plasmid combinations at timepoint 21 days post-HTVi. Of note, as I could not discern between non-tumor tissue and tumor tissue in mice injected with the different plasmid combinations, I processed entire livers and isolated the intrahepatic immune cells for further characterization.

First, I in collaboration with Dominik Vonficht used the surface marker expression of 15 cell type or cell state markers to identify clusters of $CD45^+$ living cells in the abovementioned tissues by *FlowSOM* algorithm[126] and could annotate 11 different clusters. Following that, to visualize this high-dimensional data in a two-dimensional space, I in collaboration with Dominik Vonficht used the uniform manifold approximation and projection (UMAP) algorithm and applied it on 18000 randomly chosen cells. Of note, the same number of cells (1000) was used from every sample. For annotation of individual immune populations, I in collaboration with Dominik Vonficht used the surface marker combinations, which are summarized in the heatmap shown in Figure 20.B. I detected 1 cluster of B cells ($CD19^+MHCII^+$), 2 clusters of $CD4^+$ T cells including $CD4^+$

(TCRβ$^+$CD4$^+$) and PD1$^+$CD4$^+$ (TCRβ$^+$CD4$^+$PD1$^+$), 1 cluster of CD8$^+$ T cells (TCRβ$^+$CD8$^+$), 1 cluster of TCRγδ$^+$ T cells (TCRβ$^-$CD4$^-$CD8$^-$TCRγδ$^+$), 1 cluster of NK cells (CD11b^{dim}NK1.1$^+$), 1 cluster of Eosinophils/Basophils labelled as "EoBaso" (SSC^{high}CD11b$^+$), 1 cluster of Dendritic cells "DCs" (CD11b$^+$CD11c$^+$MHCII$^+$) Ly6C$^+$ Monocytes (Cd11b$^+$CD11c$^-$ Ly6C$^+$), Ly6G$^+$Granulocytes (CD11b$^+$CD11c$^-$Ly6C$^+$) and 1 cluster of CD11c$^+$ myeloid cells negative for MHCII (CD11b$^+$CD11c$^-$ MHCII$^+$) (Figure 20.A-B).

Next, I in collaboration with Dominik Vonficht analysed the abundance of these immune populations. This quantification revealed that the CD45$^+$ composition strikingly changed between the different groups, with an obvious enrichment of the myeloid compartment specifically in the *KRAS/p53/IDH1 R132C* group (Figure 20.C-D). Namely, I observed a significant increase in DC infiltration in the livers of *KRAS/p53/IDH1 R132C*-injected mice when compared to the rest of the groups, including controls and *KRAS/p53/IDH1 R132H* animals. Although not statistically significant, I could remark a mild increase in the clusters Ly6C$^+$Monocytes, CD11c$^+$MHCII$^-$Myeloid and CD4$^+$ T cells in the *KRAS/p53/IDH1 R132C* group. Additionally, NK cells appeared to be significantly decreased in the group *KRAS/p53/IDH1 R132C* when compared to the *KRAS/p53/IDH1 WT* livers. Notably, no significant differences were found in the rest of the clusters. (Figure 20.D-E).

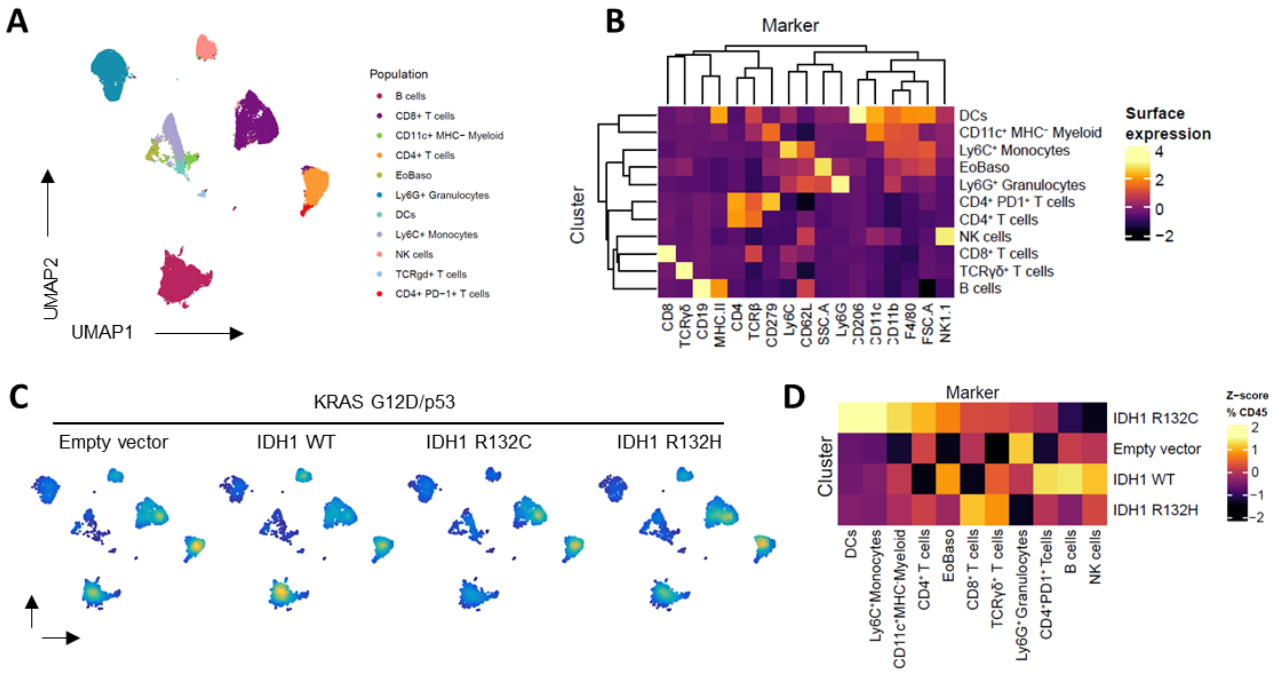

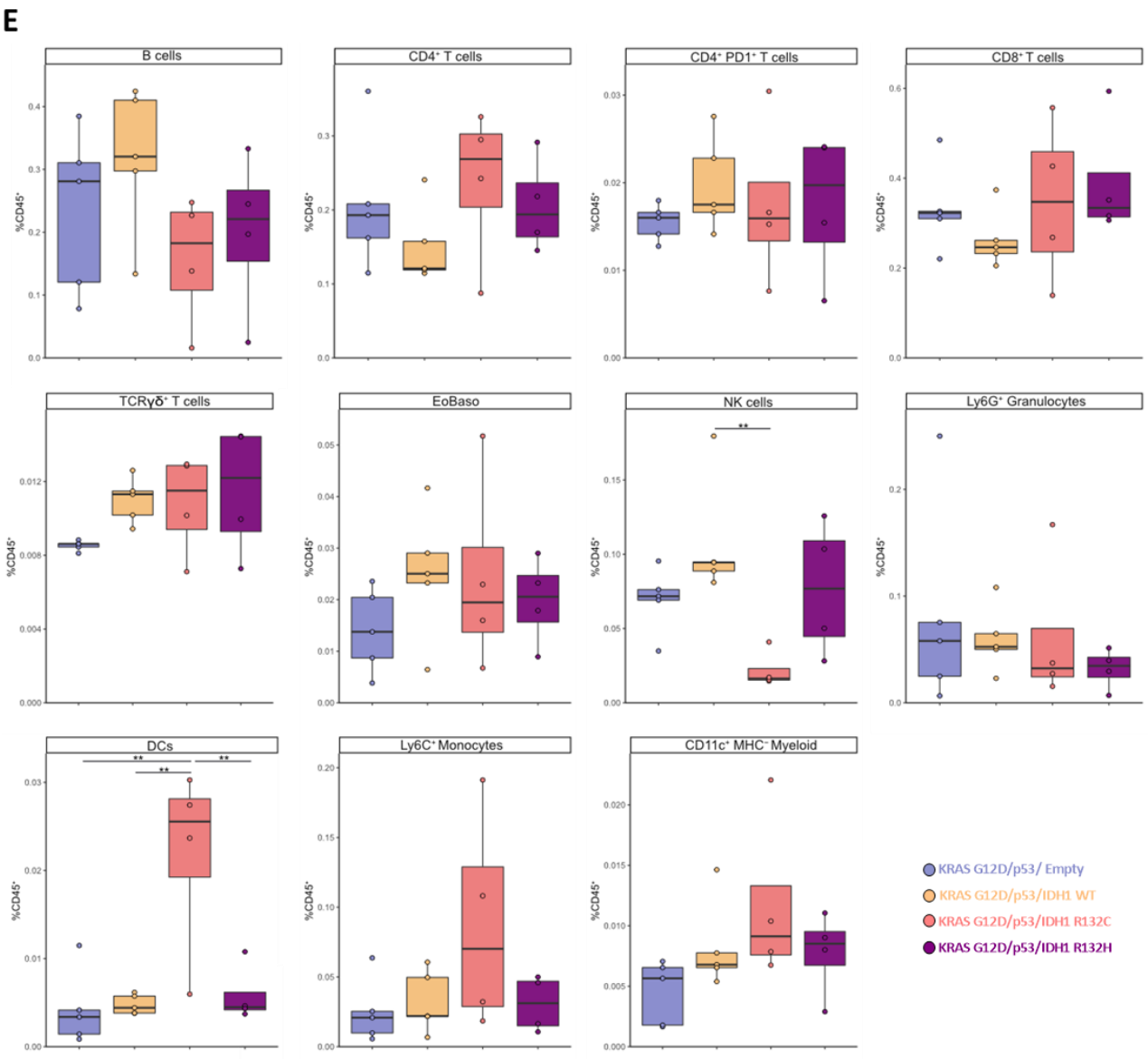

Figure 20. Deciphering the role of mutant-*IDH1* in the immune microenvironment of *KRAS/p53*-driven iCCA. (A) UMAP derived from spectral flow cytometry analysis of intrahepatic immune cells. Individual clusters were annotated and are depicted in different colors. n=18000 cells (B) Heatmap depicting the surface expression of 15 cell type of cell state markers to annotate immune populations, including FSC and SSC. (C) Feature plots highlighting the cellular density within the two-dimensional UMAP space, depicting the differential abundance of immune populations defined in B among the different plasmid groups. n=6000 cells per group. (D) Heatmap depicting the relative mean abundance of living single CD45$^+$ cells within the different plasmid groups. (E) Box plots showing the abundance analysis of the immune populations defined in B relative to single, living CD45$^+$ cells (percentage). Data are shown as individual points in boxplots. See Methods (6.12) for further details. Significance determined by one-way ANOVA with the post-hoc Tukey´s multiple comparison test, ***p*<0.01 shown.

Further, I focused on better understanding the immunomodulatory effect of *IDH1 R132C* in the liver microenvironment of *KRAS/p53*-driven iCCA. To define the immune infiltration on a spatial level I used IHC staining of immune markers in the livers from animals injected with the different plasmid combinations.

Therefore, I analysed the immune infiltration of whole liver tissue section using QuPath, including both non-affected microenvironment tissue and tumor tissue.

Interestingly, I observed that B cells (stained with B220 marker) were significantly increased in the *KRAS/p53/IDH1 R132C* livers specifically, in contrast to my previous flow cytometry data displaying minimal depletion. In the case of T cells (stained with CD4 and CD8 marker), although no differences were observed for $CD8^+$, $CD4^+$ T cells were mildly increased, not significantly, in the *KRAS/p53/IDH1 R132C* group. These results were in accordance with my flow cytometry data. Furthermore, B cells and both $CD4^+$ and $CD8^+$ T cells (stained with CD4 and CD8 marker, respectively) were infiltrating the small tumor nodules in the control groups and *KRAS/p53/IDH1 R132H* groups, but in the case of *KRAS/p53/IDH1 R132C* (displaying the highest tumor burden) these cells were rather found in the tumor periphery, that is in the border between the tumor and non-tumor microenvironment tissue.

Additionally, in line with my previous flow cytometry results, I could not detect significant variations in macrophage infiltration, but there was a mild increase of MHC-II^+ cells in the *KRAS/p53/IDH1 R132C* group in comparison to the other groups. Moreover, specifically in this *IDH1* mutant group, I could observe a remarkable and statistically significant increase in $CD11b^+$ staining, standing for monocytes, granulocytes, macrophages and DCs, and $CD11c^+$, for DCs. Notably, I found these myeloid cells mostly located within the tumor and in the periphery. (Figure 21).

Thus, this data further corroborates my previous findings that showed the ability of *IDH1 R132C* to remodel the hepatic immune microenvironment of *KRAS/p53*-induced iCCA, by displaying a significantly enriched myeloid compartment that includes intratumoral monocytes and dendritic cells.

Besides, additional effects in other immune populations, such as a decreased abundance of NK cells, suggest the cumulative assembly of an immunosuppressive microenvironment that inhibits the activity and homing of cytotoxic cells into the tumor. As a result of that, it appears that the *IDH1 R132C*-mutation has the potential to create a pro-tumorigenic environment by making the tumor cells highly proliferative and invasive resulting in an accelerated tumor development and worse survival.

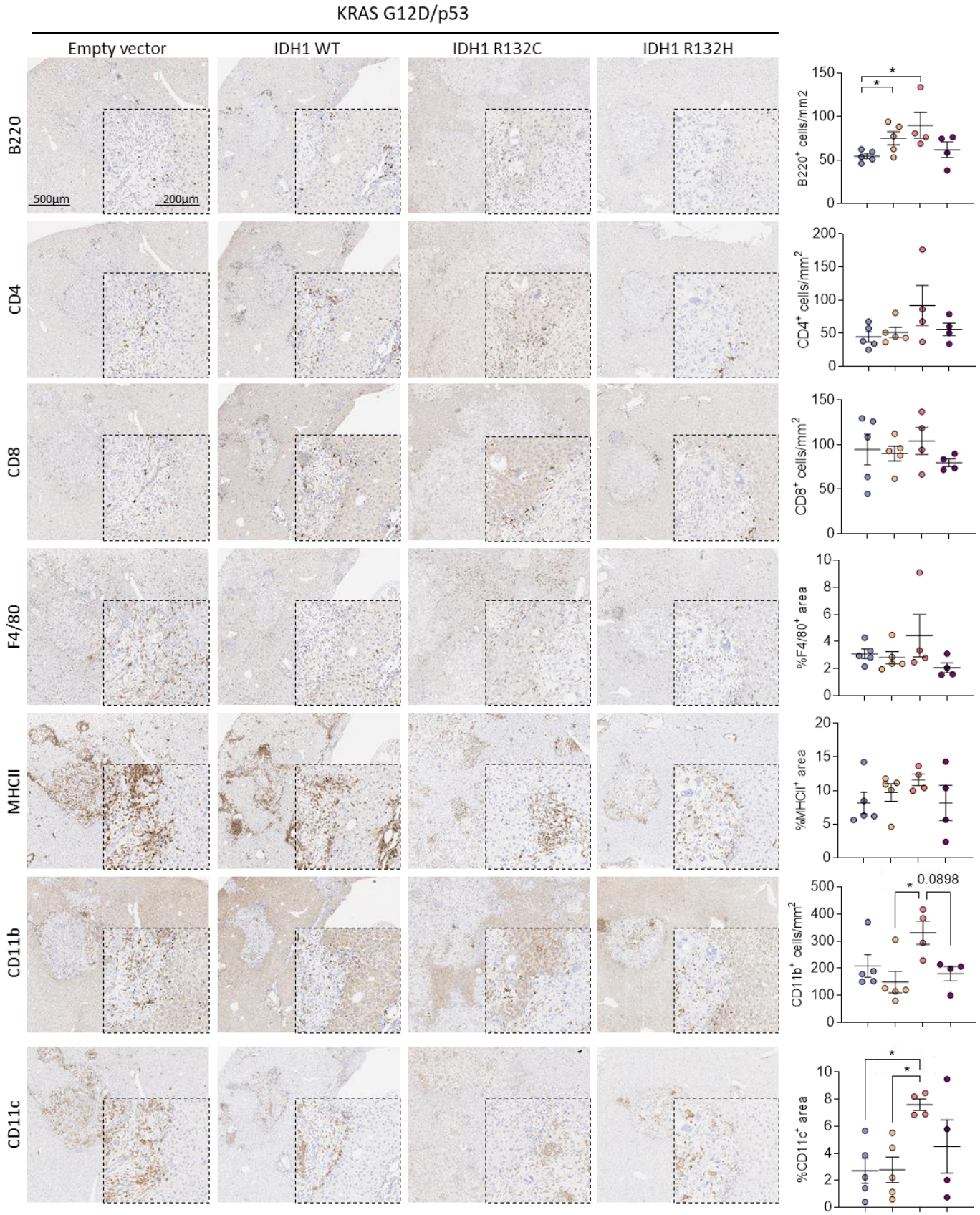
KRAS G12D/p53
Empty vector
IDH1 WT
IDH1 R132C
IDH1 R132H
B220
CD4
CD8
F4/80
MHCII
CD11b
CD11c
500µm
200µm
B220+ cells/mm2
CD4+ cells/mm2
CD8+ cells/mm2
%F4/80+ area
%MHCII+ area
CD11b+ cells/mm2
%CD11c+ area
0.0898

Figure 21. *KRAS/p53/IDH1 R132C* livers exhibit an enriched B cell and myeloid compartment. IHC staining of consecutive sections for different immune markers with respective quantification: B220, CD4, CD8, F4/80, MHCII, CD11b and CD11c. Scale bars 500µm and 200µm shown. Data are shown as mean ±SEM. Significance determined by one-way ANOVA with the post-hoc Tukey´s multiple comparison test (B-J). 0.1<*p*<0.05, **p*<0.05, ***p*<0.01, ****p*<0.001 and *****p*<0.0001 shown. ALT: Alanine Aminotransferase. AST: Aspartate Transaminase. ALP: Alcaline Phosphatase. LIP: Lipase.

7.3.8 *IDH1 R132C*-derived DCs promote a unique CD4⁺ T cell state

Next, I aimed to understand the interplay between the different immune cells and the mechanisms by which the myeloid compartment could potentially contribute to tumor progression. Notably, DCs, macrophages and B cells are considered classical antigen-presenting cells (APCs), with the ability to deliver several types of signals to T cells that result in a broad spectrum of responses. Depending on the nature of the APCs, they specially can affect CD4⁺ T cell activation, leading to a proinflammatory or immunosuppressive T cell state[149]. Therefore, having identified DCs as one of the greatly increased populations in the *KRAS/p53/IDH1 R132C*-injected animals, I used an *in vitro* DC-T cell co-culture assay to study the interaction of these immune cells and immediate downstream effects in T cells.

Consequently, I isolated both splenic and intrahepatic immune cells from *KRAS/p53/IDH1 WT* as control group, and *KRAS/p53/IDH1 R132C* at 21 days post-HTVi, to recapitulate my previous results in terms of tumor incidence (Figure 22.A-F).

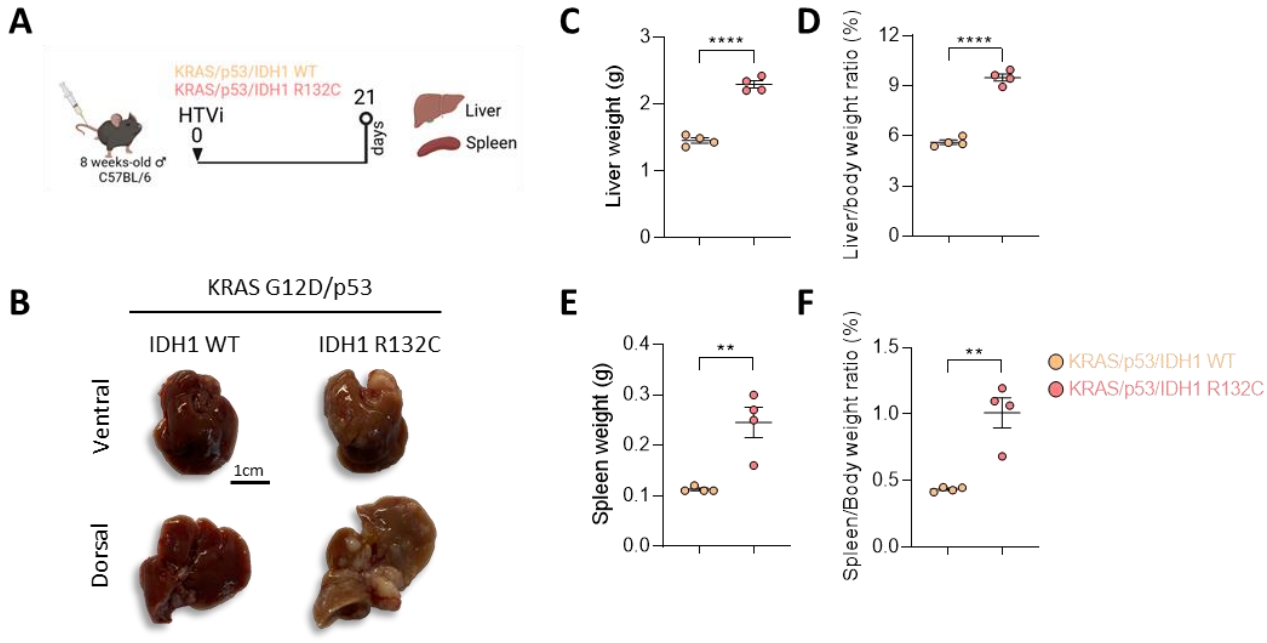

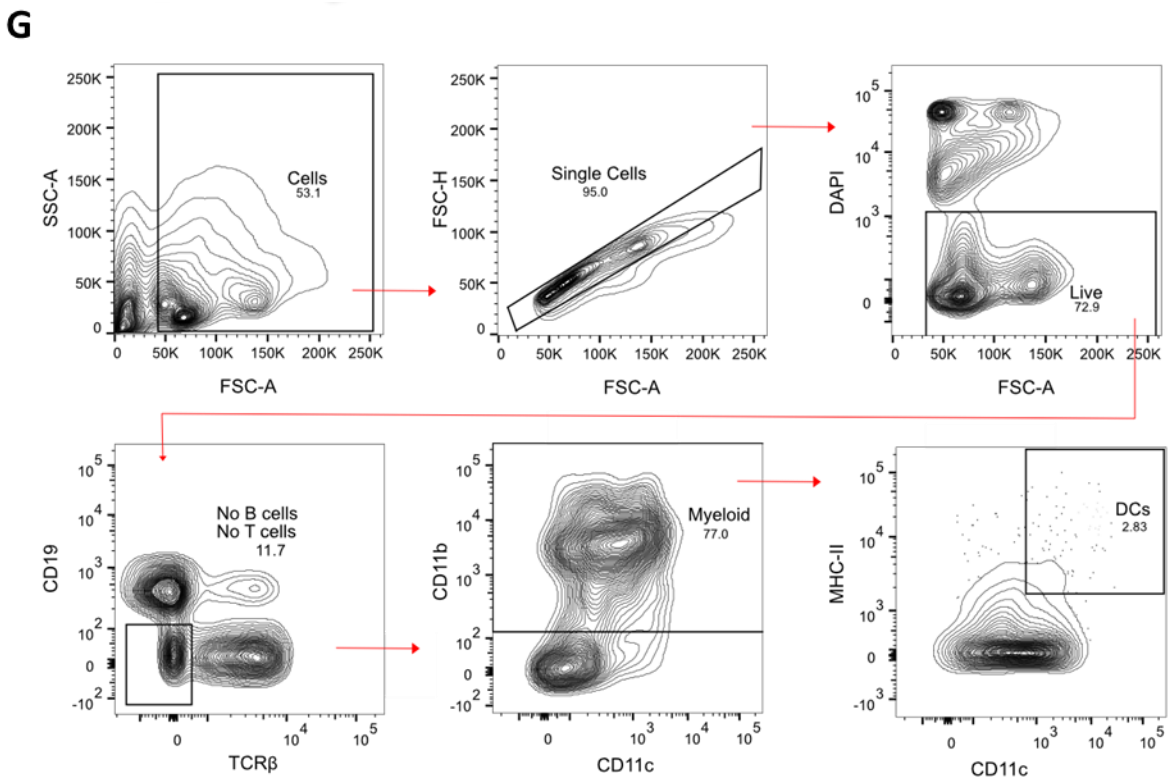

Figure 22. Unravelling the immune cell interactions in *KRAS/p53/IDH1 R132C* TIME. (A) Schematic of the experimental setting: 8-weeks old C57BL/6J male animals are injected by HTVi and livers and spleen are collected at 21 days-post HTVi for immune cell isolation. (B) Representative pictures of livers from A. (C) Liver weight per mouse. (D) Percentage showing iver weight relative to body weight. (E) Spleen weight. (F) Percentage showing spleen weight relative to body weight. (G) Representative gating strategy for FACS of DCs. Data shown as mean ±SEM. Significance determined by two-sided unpaired t-test (C-F). ***p<0.01* and *****p<0.0001* shown.

Next, I in collaboration with Dominik Vonficht sorted DCs according to the gating strategy shown in Figure 21.G ($CD45^+CD19^-TCRb^-CD11c^+CD11b^+MHCII^+$), and incubated them for 4 days with naïve OT-I and OT-II cells ($CD8^+CD62L^+CD44^-$ and $CD4^+CD62L^+CD44^-$, respectively) in presence or absence of the specific ovalbumin peptides (SIINFEKL and $OVA_{323-339}$, correspondingly).

OT-I and OT-II cells will recognize their respective peptide in the context of MHC-II on the DC and start to get activated. In case that DCs derived from KRAS/p53/IDH1 R132C-livers possess immunomodulatory or immunosuppressive capacities, upregulation of immunosuppressive immune checkpoint molecules on T cells can be the consequence, priming them towards a suppressive phenotype[129].

Analysis of the data revealed no apparent changes in neither proliferation nor polarization of $CD8^+$ T cells after culture with DCs. In the case of $CD4^+$ T cells incubated with intrahepatic and splenic DCs, CTV staining revealed that $CD4^+$ T cells were not affected in terms of cell proliferation (Figure 23.A-F). Likewise, quantification of the T cell activation status using CD44 and CD62L expression in $CD4^+$ OT-II cells showed only minimal changes (Figure 23.G-J). However, I found a remarkable switch in the $CD4^+$ T cell state. I observed that *KRAS/p53/IDH1 R132C*-derived DCs induced a polarization towards a suppressive phenotype of $CD4^+$ T cells, which significantly upregulated surface expression of markers such as CTLA-4, PD-L1 and CD25 (Figure 23.K-L), which have been linked to regulatory features with the potential to contribute to immune evasion and suppression of immune responses[150, 151].

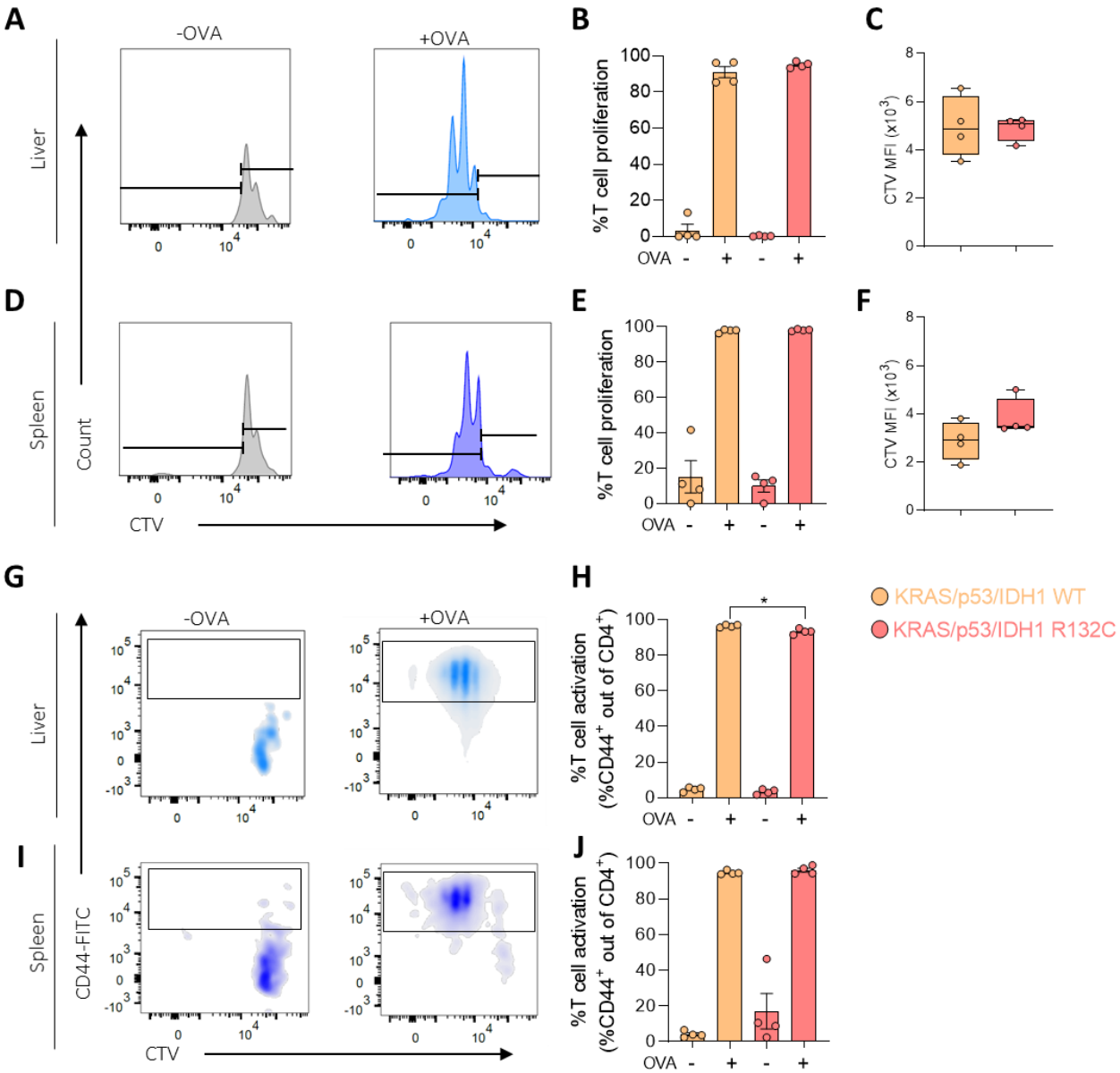

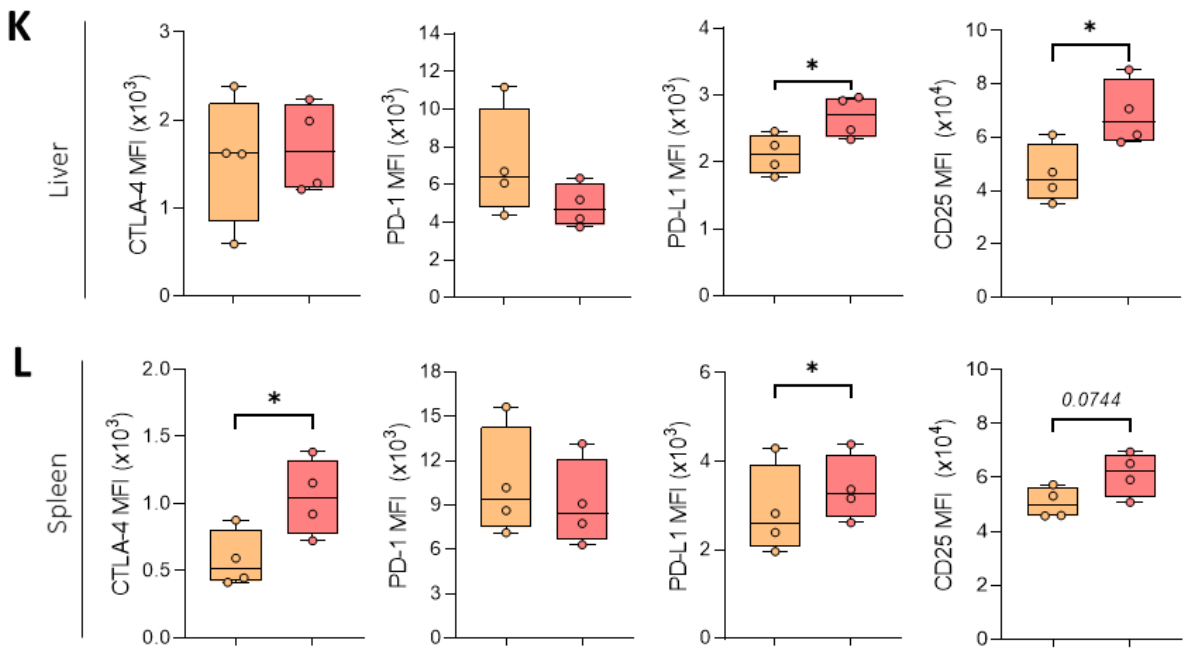

Figure 23. *KRAS/p53/IDH1 R132C*-derived DCs induce an immunosuppressive CD4⁺ T cell phenotype. (A) Representative histograms showing the Cell Trace Violet (CTV) proliferation of CD4⁺ T cells incubated with intrahepatic DCs isolated from *KRAS/p53/IDH1 WT* and *KRAS/p53/IDH1 R132C*, in presence and absence of OVA peptide. (B) Quantification of A. (C) Mean fluorescence intensity (MFI) of CTV staining from activated CD4⁺ T cells (CD4⁺CD44⁺). (D) Representative histograms showing the CTV proliferation of CD4⁺ T cells incubated with intrasplenic DCs isolated from *KRAS/p53/IDH1 WT* and *KRAS/p53/IDH1 R132C*, in presence and absence of OVA peptide. (E) Quantification of C. (F) MFI of CTV staining from activated CD4⁺ T cells (CD4⁺CD44⁺). (G) Representative histograms of CD44 expression and CTV from CD4⁺ T cells incubated with intrahepatic DCs isolated from *KRAS/p53/IDH1 WT* and *KRAS/p53/IDH1 R132C*, in presence and absence of OVA peptide. (H) Quantification of T cell activation from G. (I) Representative histograms of CD44 expression and CTV from CD4⁺ T cells incubated with intrasplenic DCs isolated from *KRAS/p53/IDH1 WT* and *KRAS/p53/IDH1 R132C*, in presence and absence of OVA peptide. (J) Quantification of T cell activation from I. (K) Surface MFI expression of CTLA-4, PD-1, PD-L1 and CD25 in CD4⁺ T cells incubated with intrahepatic DCs and (L) intrasplenic DCs. Data shown as mean ±SEM. Significance determined by one-way ANOVA with the post-hoc Tukey´s multiple comparison test (B, E, H and J) and with two-sided unpaired t-test (C, F, K and L). *0.1<p<0.05, *p<0.05, ****p<0.0001* shown.

7.3.9 SIRPα as a putative target for mutant-*IDH1* iCCA

In order to further define the responsible cells driving the immunosuppressive phenotype, I performed an additional but more detailed characterization of the immune cell and especially myeloid compartment on a systemic level. For that purpose, I collected not only the livers, but

also spleen, mesenteric (mLN) and liver-draining lymph nodes (dLN) from mice injected with the different plasmid combinations at 21 days post-HTVi.

To facilitate and unify annotation of spectral flow cytometry data, I in collaboration with Dominik Vonficht from the German Cancer Research Center in Heidelberg, used Harmony[125] to integrate data derived from 4 different organs. Then, I used the surface marker expression of 27 cell type or cell state markers to identify clusters of $CD45^+$ living cells in the abovementioned tissues using the *FlowSOM* algorithm[126]. First, I defined both lymphoid populations and myeloid populations based on presence of classical lymphoid lineage markers (CD3, TCRβ, CD4, CD8, NK1.1, CD19 and B220) or myeloid lineage markers (CD11b, CD11c, MHC-II, Ly6C, Ly6G and F4/80) (Figure 24.A). Using the *Fast PhenoGraph*[127] algorithm I could annotate 27 different clusters. To visualize this high-dimensional data in a two-dimensional space, I used uniform manifold approximation and projection (UMAP) algorithm and applied it on 19200 randomly chosen cells (Figure 24.A). Of note, the same number of cells, 200, was used from every sample. For annotation of individual immune populations I used the heatmap shown in Figure 24.B, and I could detect 1 cluster of B cells ($CD19^+B220^+MHCII^+$), 6 clusters of $CD4^+$ T cells including Activated $CD4^+$ ($CD3^+TCR\beta^+CD4^+CD25^+$), Memory $CD4^+$ ($CD3^+TCR\beta^+CD4^+CD44^{high}CD62L^{low}$), Naïve $CD4^+$ ($CD3^+TCR\beta^+CD4^+CD44^-CD62L^{high}$), $CD4^+$ Double Negative (DN) ($CD3^+TCR\beta^+CD4^+CD44^-CD62L^-$), $CD4^+$Treg ($CD3^+TCR\beta^+CD4^+CD127^{low}CD25^+$) and $CD4^+Ly6C^{hi}$ ($CD3^+TCR\beta^+CD4^+Ly6C^{high}$), 6 clusters of $CD8^+$ T cells including Effector $CD8^+$ ($CD3^+TCR\beta^+CD8^+CD44^{low}CD62L^{high}$), $CD8^+$ memory $Ly6C^{hi}$ cells ($CD3^+TCR\beta^+CD8^+CD44^{high}CD62L^{low}Ly6C^{high}$), Naïve $CD8^+$ T cells ($CD3^+TCR\beta^+CD8^+CD44^-CD62L^{high}$), Naïve $CD8^+$ $Ly6C^{hi}$ ($CD3^+TCR\beta^+CD8^+CD44^-CD62L^{high}Ly6C^{high}$), $CD8^+Ly6C^{hi}$ ($CD3^+TCR\beta^+CD8^+Ly6C^{high}$) and $CD8^+$ DN ($CD3^+TCR\beta^+CD8^+CD44^-CD62L^-$), 1 cluster of $TCR\gamma\delta^+$ T cells ($CD3^+TCR\beta^-CD4^-CD8^-TCR\gamma\delta^+$), 1 cluster of NK cells ($CD11b^{dim}NK1.1^+$), 1 cluster of Eosinophils ($SSC^{high}CD11b^+$), 4 clusters of DCs subdivided in conventional type 1 DCs (cDC1) $CD11b^{low}CD11c^+MHCII^+XCR1^+$), conventional type 2 (cDC2) ($CD11b^+CD11c^+MHCII^+CD172a^+$), plasmacytoid DCs (pDCs) ($CD11b^{low}CD11c^+MHCII^{dim}B220^+Ly6C^+$) and migratory DCs (migDC) ($CD11b^+CD11c^+MHCII^{high}CD86^+CD25^+$), 2 clusters of Monocytes divided in $CD192^{hi}$ Monocytes ($F4/80^-CD11b^+CD14^+CD192^{high}Ly6C^+$) and $CD192^{low}$ Monocytes ($F4/80^-CD11b^+CD14^+CD192^{low}XCR1^+$), 2 clusters of Granulocytes including $CD62L^{hi}$ Granulocytes ($F4/80^-CD11b^+Ly6C^+Ly6G^-CD62L^{high}$) and $CD62^{dim}$ Granulocytes ($F4/80^-CD11b^+Ly6C^+Ly6G^-CD62L^{dim}$), 1 cluster of Tumor-associated macrophages (TAM) ($F4/80^+Ly6G^+CD14^+CD86^+$) and 1 cluster of myeloid-derived suppressor cells (MDSC) ($CD11b^+CD11c^+CD14^+CD84^+Cd172a^{high}Cd192^{high}$) and MDSC-like cells

(CD11b^{+}CD11c^{+}CD14^{+}Cd172a^{high}). Interestingly, the population annotated as Eosinophils also showed a high expression of the CD84 cell marker, which has been reported to regulate the immunosuppressive effect of MDSCs[152]. In addition, DN CD4^{+} and DN CD8^{+} T cells were predominantly found in liver and to a smaller extent in the other organs.

Quantification of the abundance of the previously defined clusters relative to CD45^{+} living cells, revealed massive systemic changes in *KRAS/p53/IDH1 R132C* tumor-bearing animals, specifically. Notably, lymphatic organs (dLN and mLN) and spleen displayed similar trends and variations between different groups, therefore I focused on the changes in dLN because of its relevance in draining the liver and therefore the tumors.

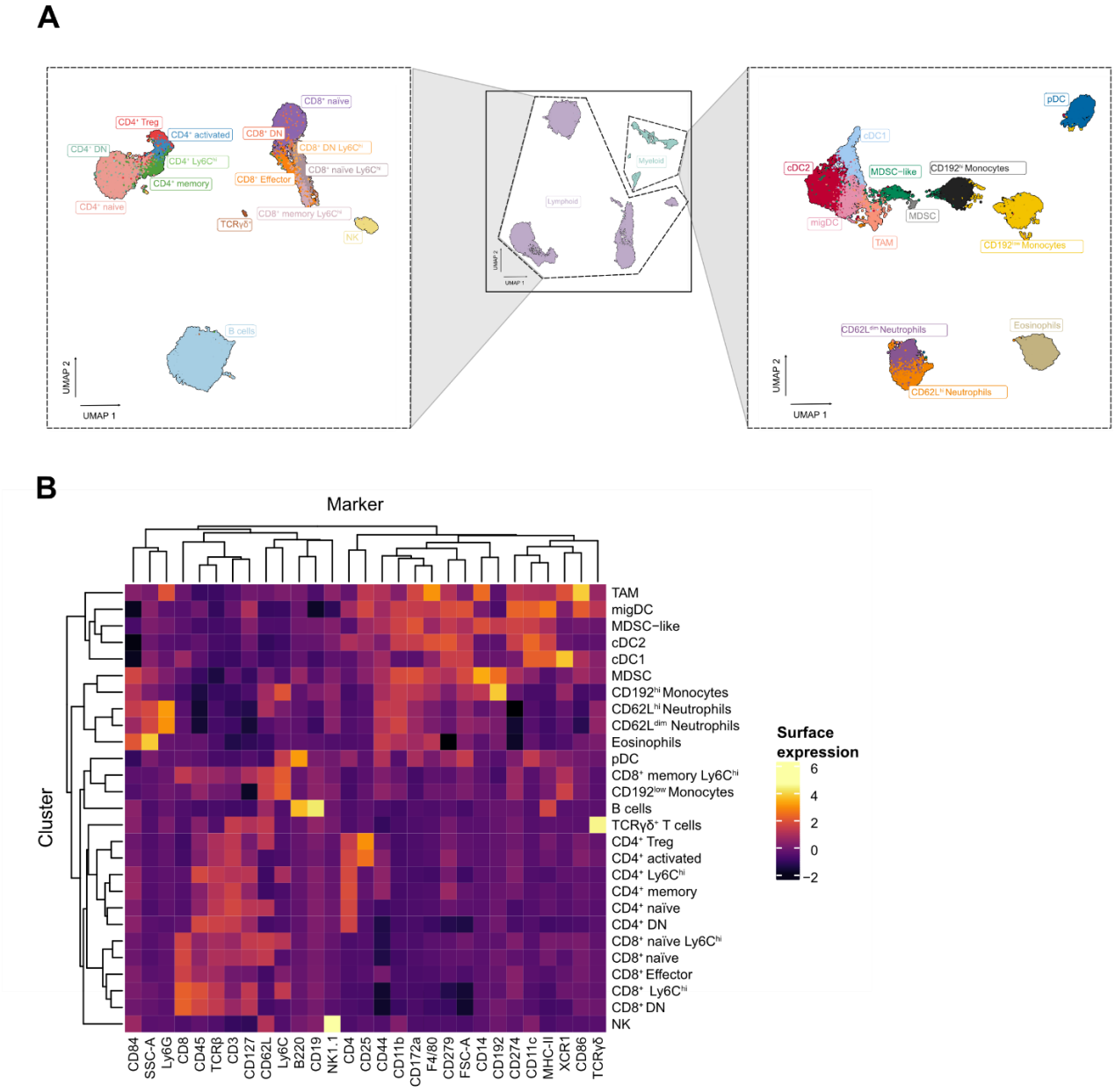

Figure 24. In-depth characterization of the *KRAS/p53/IDH1 R132C* immunosuppressive tumor microenvironment. (A) UMAP derived from spectral flow cytometry analysis of intrahepatic, splenic, dLN and mLN-derived immune cells: In depth analysis and visualization of lymphoid subset (left), overall data (middle) and in-depth visualization and characterization of the myeloid compartment (right). (B) Heatmap depicting the Z-scored mean surface marker expression in all populations.

In detail, B cells were significantly depleted in the mutant-*IDH1 R132C* liver microenvironment, in comparison to the rest of the injected animals. However, I could observe a completely reversed phenotype in the dLN, in which B cells were significantly increased in this specific group. Interestingly, I found significantly increased $CD4^+$ activated T cells in all the organs, $CD4^+$ memory and $CD4^+$ negative but decreased $CD4^+$ naïve in dLN. This overall indicates that $CD4^+$ T cells acquire a highly activated state, which would be in line with an inflammatory phenotype. However, I could not observe any changes in classical $CD127^-CD25^+CD4^+$ T_{regs} in the organs.

In line with previous studies[72, 115], $CD8^+$ effector T cells and $CD8^+$ memory $Ly6C^+$ were significantly depleted in the *KRAS/p53/IDH1 R132C*-derived livers, showing therefore a suppression of the cytotoxic activity of $CD8^+$ T cells. Moreover, consistent with my previous results, I could observe a notable increase of myeloid populations in the liver, and to an even greater extent in the dLN. Eosinophils as well as DCs (including cDC1, cDC2 and migDC) were significantly increased in the dLN. Similar trends, meaning, significant increases were found in monocyte and neutrophil populations, also in both organs of *KRAS/p53/IDH1 R132C*-injected animals. Remarkably, also in both organs, I found a striking enrichment of TAM and MDSC-like cells (cells with macrophage/monocyte features and immunosuppressive markers), specifically in the *IDH1 R132C* mutant group (Figure 25).

Thus, these observations further confirmed the establishment of an inflammatory phenotype characterized by and increased infiltration of immunosuppressive cells in *KRAS/p53/IDH1 R132C*-derived TIME.

Next, with the aim of potentially targeting these cells as a therapeutic strategy to cease tumor progression in iCCA, I focused on identifying surface markers characteristic of these immunosuppressive cells. Visualization of the mean relative abundance of immune populations in $CD45^+$ single living cells in different organs and injected groups, highlights again an enrichment of the myeloid populations (Figure 26.A). By analysing pan-myeloid surface marker expression, I found that CD172a, which stands for Signal regulatory protein α (SIRPα), is mainly and specifically expressed in myeloid-lineage cells, comprising monocytes, macrophages, DCs and neutrophils (Figure 26.B). SIRPα has been previously characterized as an inhibitory molecule mainly

expressed in myeloid-lineage cells which limits innate immunity responses through its interaction with the surface ligand CD47[153]. Indeed, in my experimental setting, I could confirm the literature data and found SIRPα to be predominantly expressed in myeloid populations, with the highest expression in cDC2, TAM, MDSC and MDSC-like cells. Notably, these populations corresponded to the significantly enriched immune populations that I proposed to induce the immunosuppressive phenotype in the *KRAS/p53/IDH1 R132C*-injected animals. In addition, to further prove the relevance of this inhibitory molecule as a potential therapeutic treatment, I in collaboration with Dominik Vonficht binned overall $CD45^+$ single living cells into $CD172^+$ and $CD172^-$ compartments, and performed this for all of the organs and experimental groups. I could observe a compelling increase of $CD172a^+$ cells in all *KRAS/p53/IDH1 R132C*-derived organs of interest (Figure 26.C).

Consequently, I identified SIRPα as a myeloid-lineage marker of proinflammatory and likely immunosuppressive cells that could be further explored as a potential immune checkpoint in mutant-*IDH1* iCCA.

7.3.10 SIRPα and PD-L1 blockade synergize to reduce tumor burden in *KRAS/p53/IDH1 R132C*-driven iCCA

My data indicates that SIRPα is expressed in the myeloid populations which are significantly increased in the context of *KRAS/p53/IDH1 R132C* iCCA. This observation prompted me to explore the role of $SIRP\alpha^+$ cells in driving the immunosuppressive microenvironment and their potential contribution to tumor development.

With that aim and following my previous experimental set up, I injected 8-weeks old C57BL/6J male animals by HTVi with either *KRAS/p53/IDH1 WT* plasmids as a control group, or *KRAS/p53/IDH1 R132C*. After one week of HTVi, I started a biweekly treatment with selective antibodies blocking SIRPα or Isotype IgG_1 control antibody. In addition, based on my previous data showing the induction of an immunosuppressive phenotype in $CD4^+$ T cells after incubation with DCs isolated from *KRAS/p53/IDH1 R132C* tumor-bearing livers (Figure 23), I included an additional experimental condition to test the effects of anti-PD-L1 treatment as a single agent or in combination with anti-SIRPα. To determine the therapeutic potential of the treatments mentioned above, I culled the animals at 21 days-post HTVi (Figure 27.A)

A

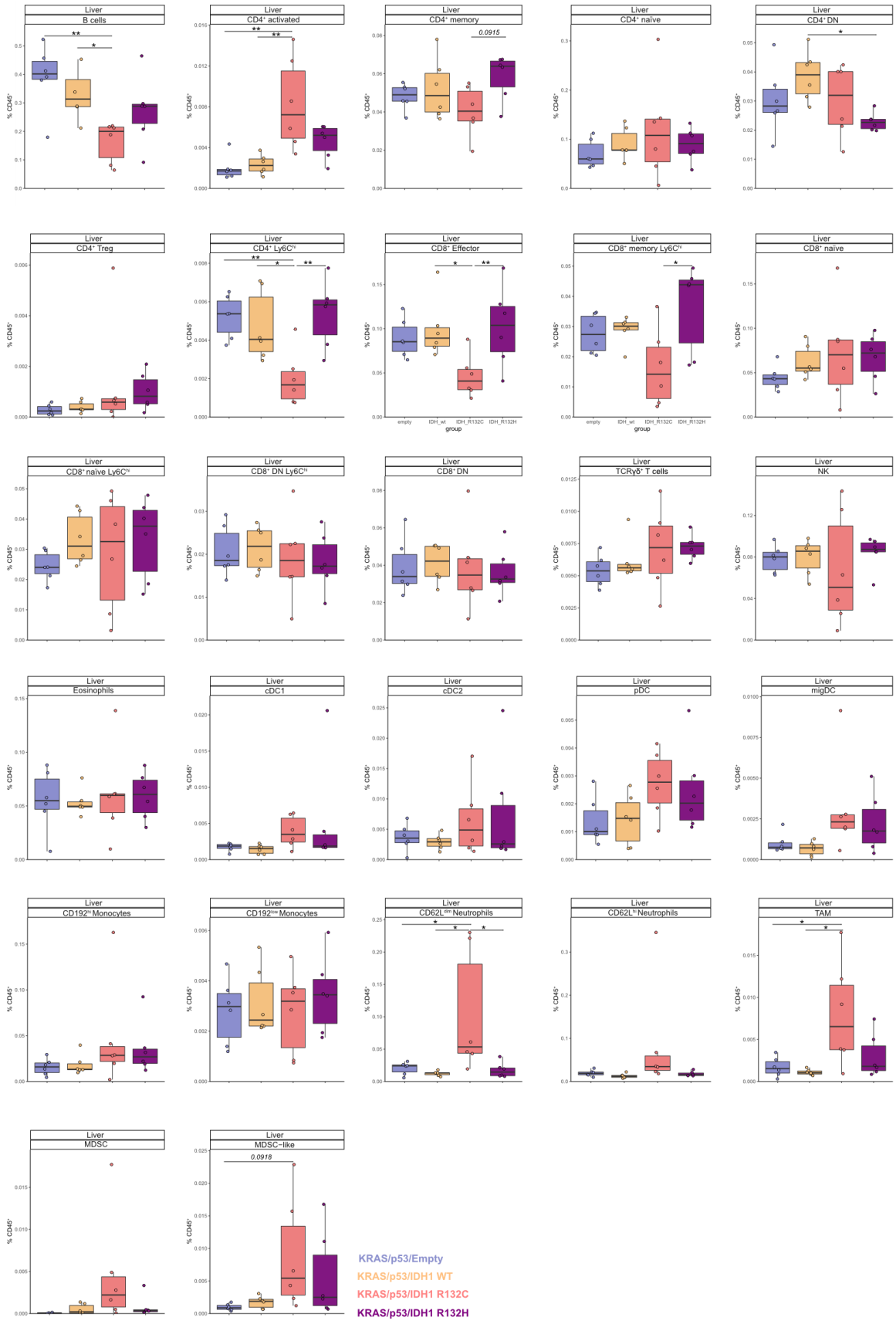
Liver
B cells
Liver
CD4+ activated
Liver
CD4+ memory
0.0915
Liver
CD4+ naïve
Liver
CD4+ DN
Liver
CD4+ Treg
Liver
CD4+ Ly6Chi
Liver
CD8+ Effector
Liver
CD8+ memory Ly6Chi
Liver
CD8+ naïve
Liver
CD8+ naïve Ly6Chi
Liver
CD8+ DN Ly6Chi
Liver
CD8+ DN
Liver
TCRγδ+ T cells
Liver
NK
Liver
Eosinophils
Liver
cDC1
Liver
cDC2
Liver
pDC
Liver
migDC
Liver
CD192hi Monocytes
Liver
CD192low Monocytes
Liver
CD62Lint Neutrophils
Liver
CD62Lhi Neutrophils
Liver
TAM
Liver
MDSC
Liver
MDSC−like
0.0918
% CD45+
group
empty
IDH_wt
IDH_R132C
IDH_R132H
KRAS/p53/Empty
KRAS/p53/IDH1 WT
KRAS/p53/IDH1 R132C
KRAS/p53/IDH1 R132H

B

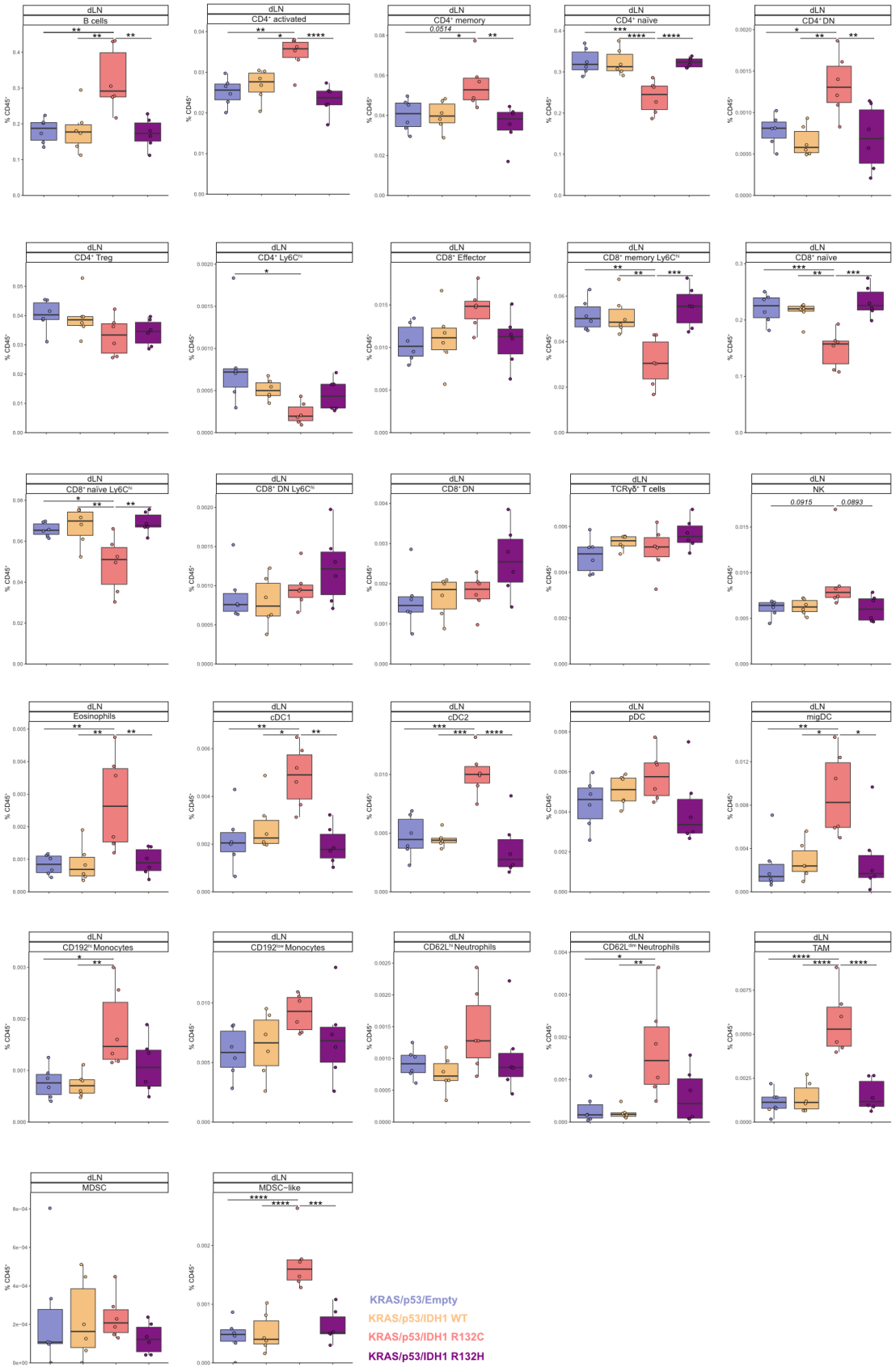
dLN
B cells
dLN
CD4+ activated
dLN
CD4+ memory
0.051
dLN
CD4+ naive
dLN
CD4+ DN
dLN
CD4+ Treg
dLN
CD4+ Ly6Chi
dLN
CD8+ Effector
dLN
CD8+ memory Ly6Chi
dLN
CD8+ naive
dLN
CD8+ naive Ly6Chi
dLN
CD8+ DN Ly6Chi
dLN
CD8+ DN
dLN
TCRγδ+ T cells
dLN
NK
0.0915
0.0893
dLN
Eosinophils
dLN
cDC1
dLN
cDC2
dLN
pDC
dLN
migDC
dLN
CD192hi Monocytes
dLN
CD192low Monocytes
dLN
CD62Lhi Neutrophils
dLN
CD62Ldim Neutrophils
dLN
TAM
dLN
MDSC
dLN
MDSC-like
% CD45+
KRAS/p53/Empty
KRAS/p53/IDH1 WT
KRAS/p53/IDH1 R132C
KRAS/p53/IDH1 R132H

Figure 25. *IDH1 R132C* leads to an enrichment of immunosuppressive myeloid, aggravating inflammation and tumor development. (A) Box plots showing quantification of immune populations relative to CD45⁺ single living cells in the livers and (B) dLN of animals injected with different plasmids. Data shown as mean ±SEM. Significance determined by one-way ANOVA with the post-hoc Tukey´s multiple comparison test. *0.1<p<0.05, *p<0.05, ** p<0.01, *** p<0.001* and *****p<0.0001* shown.

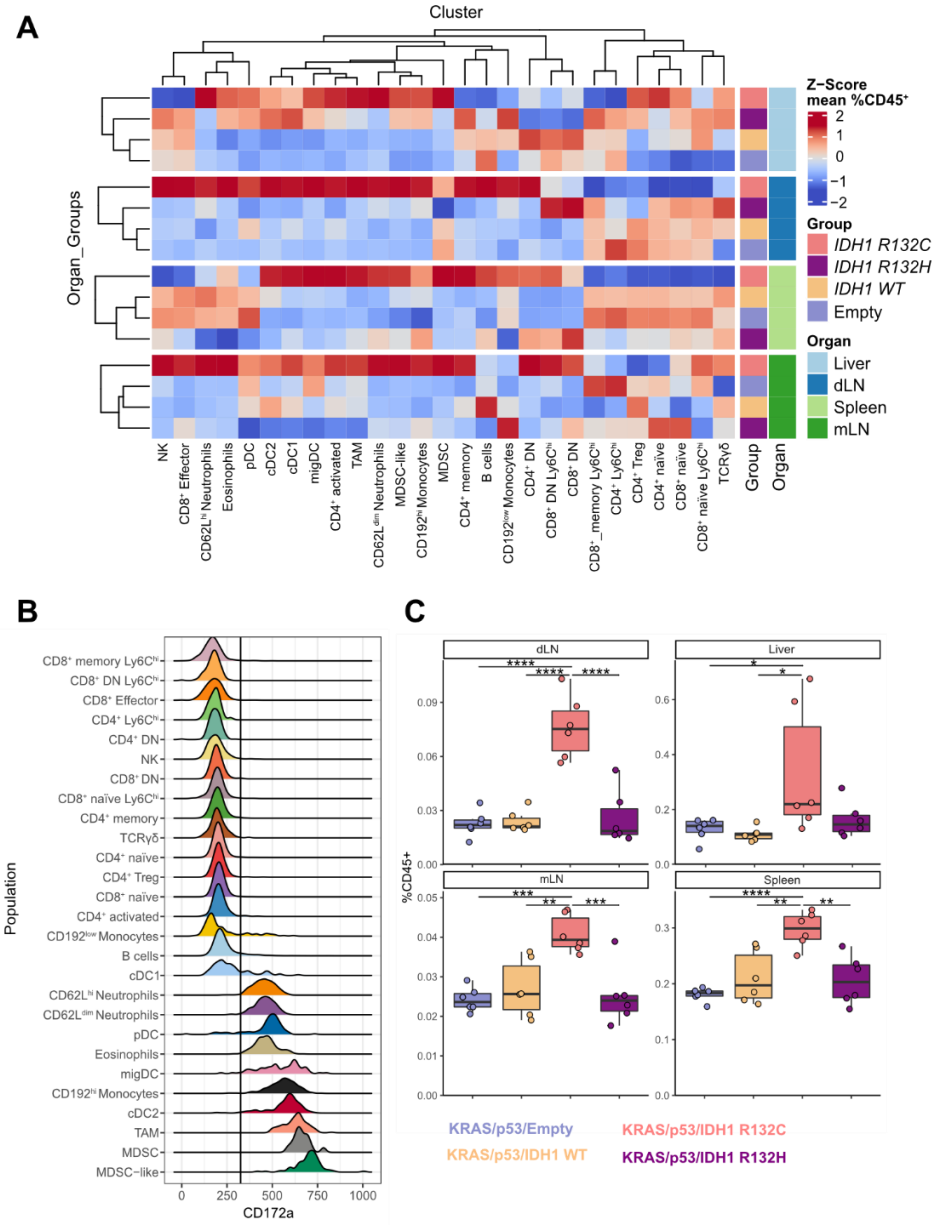

Figure 26. SIRPα⁺ cells are enriched in *KRAS/p53/IDH1 R132C*-derived immune compartment. (A) Heatmap showing abundance of clusters defined in Figure 24 in the different organs and groups. (B) Ridge plot showing the expression of CD172a in the different populations. Logicle transformation of CD172a expression shown on the X axis. Black vertical line was used for binning CD45⁺ cells into CD172⁺ and CD172⁻ groups. (C) Quantification of SIRPα⁺ cell abundance relative to CD45⁺ living cells in the different organs and groups. Data shown as mean ±SEM. Significance determined by one-way ANOVA with the post-hoc Tukey´s multiple comparison test. *0.1<p<0.05, *p<0.05, ** p<0.01, *** p<0.001* and *****p<0.0001* shown.

In accordance to my previous data, I observed a remarkable increase in the liver weight and liver to body weight ratio in the group of animals injected with *KRAS/p53/IDH1 R132C* plasmids and treated with Isotype control, when compared to *KRAS/p53/IDH1 WT* treated with Isotype control (Figure 27.C-D). These observations were in line with the quantification of tumor number and tumor size, which correlated with the analysis of $CK19^{+}$ area and the number of $Ki67^{+}$ proliferating cells (Figure 27.E-I). Besides, I found similar significant changes between *IDH1 WT*- and *IDH1 R132C*-driven groups treated with anti-SIRPα group, indicating that blockade of SIRPα is not capable of inducing a response against tumor development. However, the addition of anti-PD-L1 to SIRPα blockade led to striking results. Although I did not observe any differences in the *KRAS/p53/IDH1 WT*-injected animals, combinational therapy of anti-PD-L1/anti-SIRPα significantly reduce tumor burden in the context of *KRAS/p53/IDH1 R132C*-driven iCCA (Figure 27.E-I).

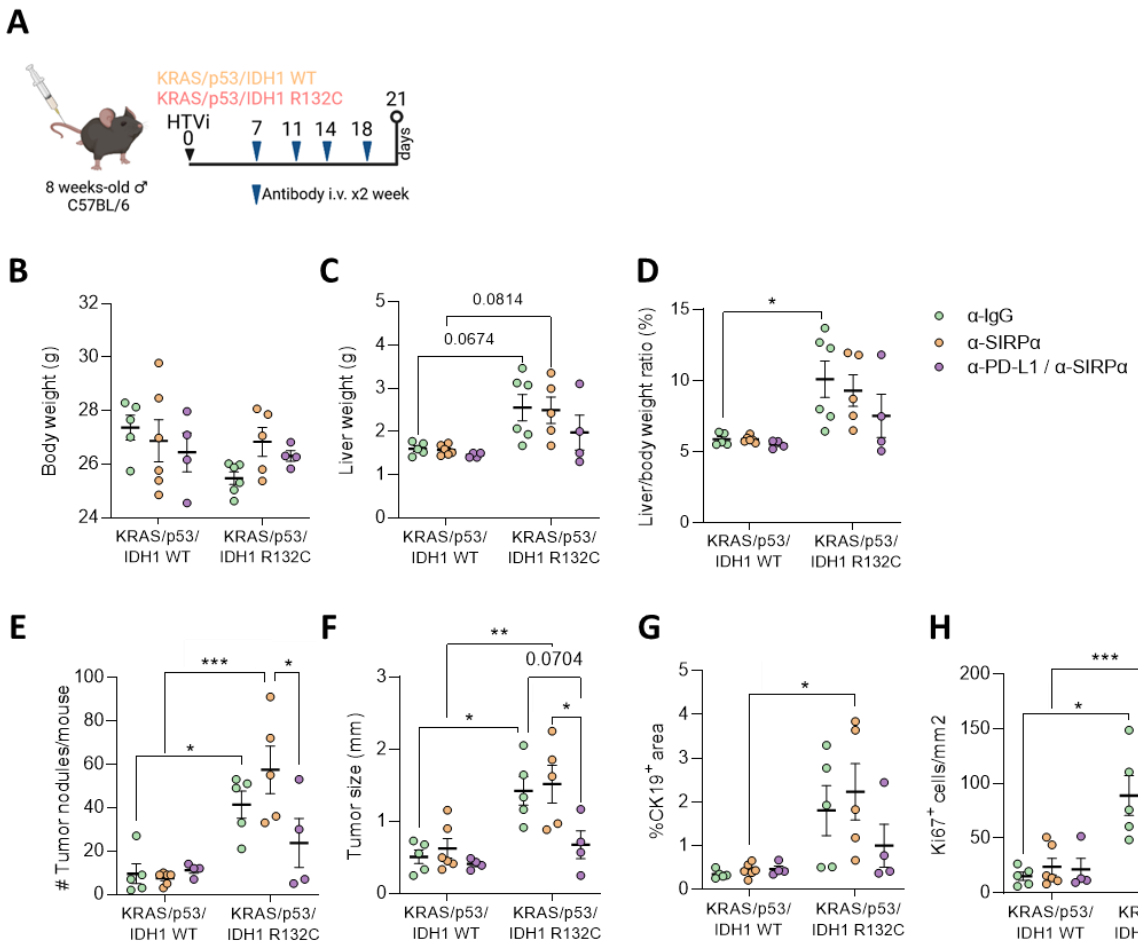

I

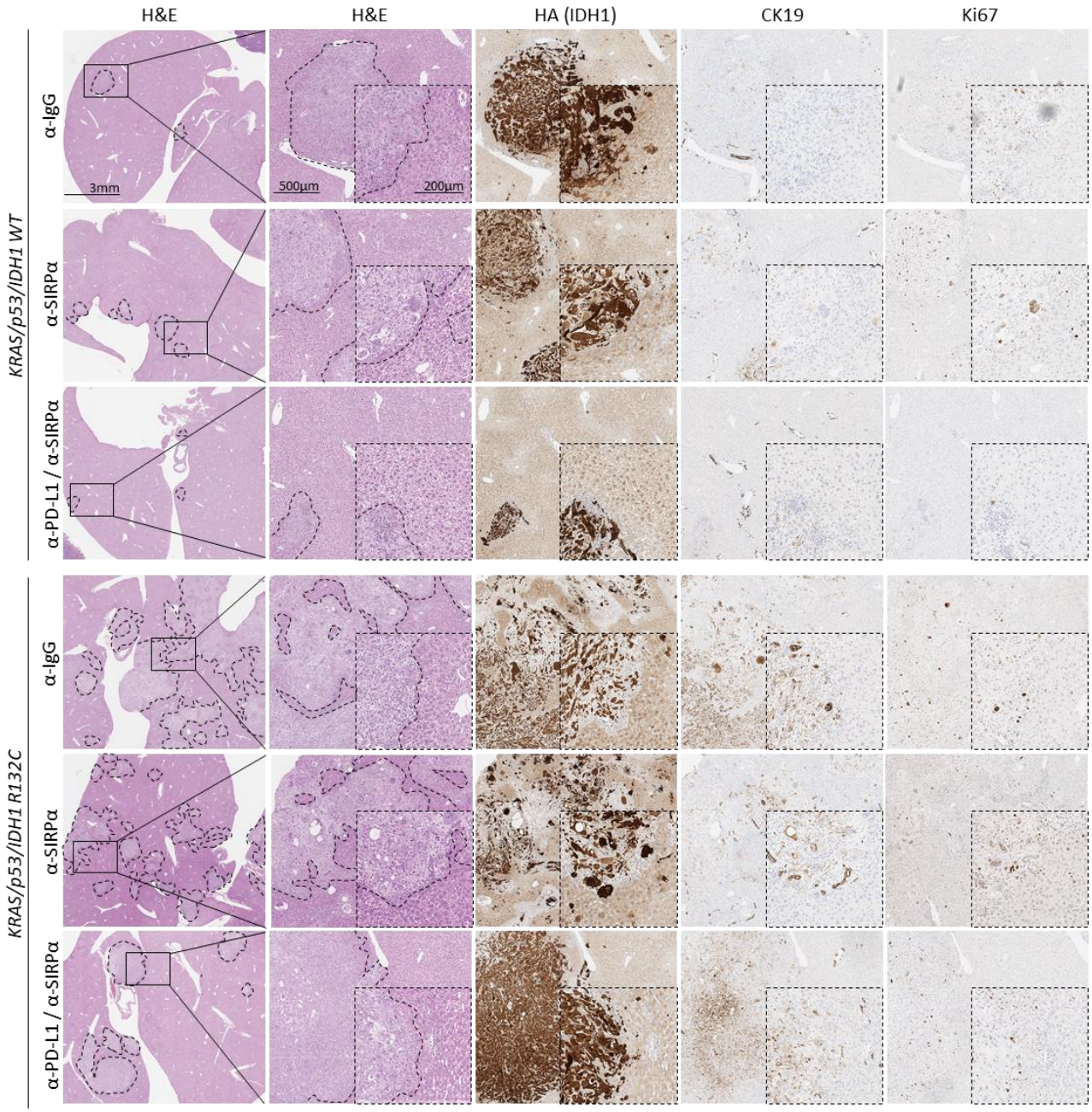

Figure 27. SIRPα and PD-L1 blockade synergizes to reduce tumor burden in *KRAS/p53/IDH1 R132C*-driven iCCA. (A) Experimental set up in which 8-weeks old C57BL/6J male animals are injected by HTVi with *KRAS/p53 and IDH1 R132C* or *IDH1 WT* as a plasmid control group. These animals are treated biweekly starting one week post-HTVi (7 days) with Isotype IgG_1 antibody (α-IgG), anti-SIRPα (α-SIRPα) and the combination of α-SIRPα with α-PD-L1. (B) Body weight. (C) Liver weight. (D) Percentage showing liver to body weight ratio. (E) Number of tumor nodules and (F) tumor size per mouse. (G) Analysis of IHC staining in liver sections corresponding to percentage of CK19 positive area and (H) proliferative cells by number of Ki67 marker. (I) IHC staining of consecutive sections for different immune markers with respective quantification: H&E, HA-tag for IDH1 expression, biliary differentiation marker CK19 and proliferation marker Ki67. Scale bars 500 µm and 200 µm shown. Data shown as mean ±SEM. Significance determined by two-way ANOVA with the post-hoc Tukey´s multiple comparison test. *0.1<p<0.05, *p<0.05, ** p<0.01* and *** p<0.001* shown.

Notably, animals injected with anti-PD-L1, regardless of the plasmid combination, exhibited an anaphylaxis-like reaction after the third and fourth application of the antibody intravenously (day 14 in Figure 27.A) dying within 5 min. after injection. In the combined treatment group (anti-PD-L1/anti-SIRPα), certain animals survived reaching the analysis timepoint. Despite the technical issue, animals injected with *KRAS/p53/IDH1 R132C* and treated with anti-PD-L1 exhibited a high tumor load. These observations led to the assumption that only when combined, PD-L1 and SIRPα blockade remodels the liver microenvironment to enhance anti-tumor response.

8 Discussion

In the past decades, an alarming rise in the cases of iCCA has been reported, a particularly heterogeneous cancer that emerges in the bile ducts located in the liver[22]. The diversity that characterizes this malignancy is not only present on a molecular level, with a broad deregulation of signalling pathways, but also includes the possibility that different cell types can act as the cell of origin. The latter renders diverse histopathologic phenotypes possible in iCCA that show various differentiation and growth patterns[2, 16, 25, 26]. Moreover, as the disease progresses silently without clinical manifestations, detection only in later stages is likely, leaving the patient subject to chemotherapy and surgical resection as current standard of care[23]. Although relevant progress in the development of therapeutic strategies has been made in recent years, iCCA is still considered a rare and challenging disease.

In order to identify and develop new therapeutic approaches, a focus on understanding the molecular underpinnings governing this disease is crucial. With that purpose, thorough integrative analyses have been conducted and potential targetable mutations have been identified[2, 31-35]. Notably, gain-of-function mutations in the *IDH1* gene, which lead to the production of 2-HG, have been found in 15-20% of iCCA cases[87, 105]. These alterations have been shown to be involved in several pathophysiological mechanisms, enhancing tumor development and remodelling the immune landscape, and driving human cancer[83]. Moreover, the recent approval of a selective small-molecule *IDH1* inhibitor (Ivosidenib) for the treatment of locally advanced or metastatic mutant-*IDH1* CCA has raised interest for understanding this condition to develop strategies that reduce potential mechanisms of resistance[100].

8.1 Impact of *IDH1* mutations in the liver microenvironment

With the aim to determine the effects that *IDH1* mutations have in the liver microenvironment, I made use of two different immunocompetent *in vivo* mouse model systems: transposon-based models and GEMMs.

The transposon-based model consists on the HTVi technique that allows the integration of DNA elements specifically into the liver, enhancing the overexpression by transposon-based vectors and/or deletion of genes of interest by using CRISPR-Cas9 vectors[79]. For that, I in collaboration with Tobias Riedl, established DNA vectors encoding the overexpression of various *IDH1*

mutations found in human iCCA cases (R132C as the most common amino acid alteration, reported in 80% of the cases, followed by R132G, R132L and R132S) as well as the R132H mutation mostly found in glioma, and the appropriate technical and biological controls (that is, Empty and *IDH1 WT* vectors, respectively) (Figure 6).

Delivery of single *IDH1* plasmids in 8-weeks old male C57BL/6J mice validated the appropriate transfection and functional activity of mutant-*IDH1* (Figure 7 and 8). This shows the advantage of the HTVi model system to study the expression of a certain genetic alteration, mutant-*IDH1* in my work, with the derived molecular consequences in an immunocompetent host. In detail, although I did not observe any alterations on a histological level, my data showed increased hepatic 2-HG levels ranging between 200-750 pmol/mg tissue, depending on the *IDH1* amino acid substitution. However, these levels were markedly lower in comparison with the GEMM model published by Wu and colleagues (median concentration 35.3nmol/mg in *Alb-Cre;Idh1*^{R312C})[72]. In addition, a potential limitation of using the HTVi model system was the high variability of transfection efficiency (shown by HA^+GFP^+ cells). These observations were in line with previous publications indicating different expression levels of oncogenes in tumors derived by HTVi, which depended on the levels of gene integration (*MYC*, *Tert* overexpression model)[154]. Due to the fact that 2-HG is the direct oncometabolite derived from *IDH1* mutations, in this context transfection efficiency may affect not only the gene expression levels, but also the derived biological role of mutant-*IDH1*. Indeed, the inter-heterogeneity derived from variable transfection rates was further accentuated as shown by the strong positive correlation between the number of transfected cells and 2-HG levels. Moreover, the decrease of transfected cells from 3 to 6 months timepoint could be explained by the process in which cells overexpressing the mutation undergo oncogene-induced senescence, apoptosis or immune clearance (senescent cells secrete cytokines that can recruit immune cells, the so-called senescence-associated secretory phenotype -SASP), previously reported in hepatocytes overexpressing *NRAS G12V* by HTVi[142]. Potential immunogenicity of the elements included in the engineered vectors would also explain the clearance of the lost expression. In detail, previous reports have shown that proteins that are not expressed normally in mice but are part of the vectors, that is GFP, mCherry or Cas9 are immunogenic in the C57BL/6 background, and therefore cleared by immune cells[143, 155].

In my hands, single *IDH1* mutations did not lead to any histopathological manifestations in the liver. Therefore, future experiments could focus on assessing the effects of mutant-*IDH1* by studying the relationship between the dose of mutant-*IDH1* that each mouse perceived, that is more than 10 ug/mouse used in my work. This would potentially enhance the cell transfection and

therefore increased production of the oncometabolite, with higher chances of affecting the liver microenvironment.

Additionally, I used the recently published mutant-*Idh1* GEMM model[72] as an alternative tool for studying the remodelling effects of mutant-*Idh1* (Figure 9). This model allows the study of the constitutively active *Idh1* mutations in the liver microenvironment in combination with other genetic alterations. However, I found that the hepatomegaly shown by cre+ animals could potentially comprise a technical limitation for the use of this model for HTVi purposes, as the volume injected is based on the variable of body weight, non-differing between both genotypes (Figure 10). To further address this hypothesis, I overexpressed AKT by HTVi in these mice, which has been previously shown to promote an enlarged and steatotic liver phenotype[144]. Nevertheless, only cre- mice developed such features, supporting my previous hypothesis, where the difference in basal liver weight restricts the experimental approach (Figure 11).

Overall, these observations were in line with previous studies indicating that the introduction of a sole alteration was not able to induce tumor development in the liver of C57BL/6J mice, but rather needs additional modifications[154].

8.2 Contribution of mutant-*IDH1* with genetic alterations in iCCA

To understand intra-tumor heterogeneity of mutant-*IDH1* iCCA*,* I delivered individual common genetic alterations found in human iCCA, together with *IDH1 R132C* plasmids by HTVi. Nevertheless, my data indicated that in contrast to other genetic modifications that just need an additional hit to drive tumorigenesis[139, 154, 156], this does not apply to mutant-*IDH1* in the liver.

In my experience, groups injected with *AKT* or *NOTCH* overexpression, alone or in combination with *IDH1 R132C*, were the only groups that exhibited tumor nodules after 6 months post-injection. Based on IHC results showing a markedly low amount of HA+GFP+ transfected cells in tumors, therefore expressing mutant-*IDH1*, I hypothesized that these mutations may contribute to remodelling the liver microenvironment, enhancing tumorigenesis -depending on the oncogenic signalling- but it is not sufficient to drive the carcinogenic process by HTVi (Figure 12 and 13). This is in accordance with unpublished data from collaboration partners, showing that mutant-*IDH1* delivered by HTVi and organoid culture, suffers a selective pressure leading to cell death, therefore not able to lead to cancer. In contrast, Prof. Dr. Nabeel Bardeesy´s research showed that although constitutive activation in hepatocytes (*AlbCre*) of *IDH1* and *IDH2* mutations (R132C

and R172K, correspondingly) in GEMMs did not lead to tumor incidence, cooperated with *Kras G12D* in generating aggressive tumors within 49.3 and 47.3 weeks in average, respectively[28, 72].

Taken together, these observations indicate the importance of mutant *IDH1*-derived remodelling effects, in terms of expression and biological function, with the latter increasing 2-HG production.

8.3 *IDH1 R132C* accelerates tumorigenesis, migration and remodels the liver immune microenvironment of iCCA

Considering my previous data on the molecular characterization of mutant *IDH1* in the liver microenvironment, I assessed the tumor heterogeneity of *IDH1* mutations in the tumorigenic environment of iCCA.

In line with my previous data, published studies indicate that *IDH1 R132C* in combination with *NOTCH* overexpression and *p53* silencing cooperates to drive cholangiocarcinogenesis by HTVi[148]. In my work, despite using a different mouse strain (C57BL/6J in my experience vs. FVB/N animals), engineered vectors (sgRNA targeting p53 in my hands vs. shRNA) and plasmid concentrations, I could recapitulate the pro-tumorigenic effect of mutant-*IDH1* in the context of *NOTCH/p53*. However, differing tumor incidence and histopathological results compared to previous published data, highlighted that factors such as mouse strain, DNA vectors or even sex are key in determining variability in tumor latency in HTVi-driven tumor models. Also, my IHC data on HA and mCherry-reporter for *IDH1* and *NOTCH* plasmid respectively, indicated the importance of demonstrating the overexpression of the DNA delivered. Consequently, I determined on a macroscopic level that the tumors present in animals injected with *NOTCH/p53/IDH1 R132C* were driven by *NOTCH*, but mutant-*IDH1*, instead of being the main driver, rather supported the environment that promotes cholangiocarcinogenesis (Figure 14).

Further, the addition of *IDH1* mutations in the *KRAS/p53*-driven iCCA HTVi model revealed a striking dependency of *IDH1 R132C* in accelerating tumorigenesis within a specific oncogenic context This observation was confirmed by both a significantly decreased survival and a higher tumor incidence at an earlier timepoint of 21 days post-HTVi (Figure 15 and 18). The remarkable different phenotype between *IDH1 R132C* and *IDH1 R132H,* specially at the earlier timepoint, highlights once more that different *IDH1* mutations lead to different environmental dynamics, and this may be the reason why R132C substitution is reported as the most common mutation among mutant-*IDH1* iCCAs[157, 158]. Importantly, IHC staining of *IDH1* reporters (expression of HA-tag and

GFP) verified that most of the tumors were driven by the integration of the 4 different vectors (*KRAS*, *IDH1*, *sgTp53* and SB). Moreover, in line with my previous experiments validating the biological functionality of mutant-*IDH1*, measurement of the oncometabolite 2-HG was present not only in the tumor tissue, but also in the non-affected microenvironment, with values reaching up to 1500 pmol/mg tissue. Here, I found similar levels in the tissues of *IDH1 R132C*- and *IDH1 R132H*-injected mice. This could be explained by the fact that the latter animals survive longer, and eventually reach a comparable amount of 2-HG production. Apart from the local tumor development, this model allowed the study on the effects of mutant-*IDH1* in cell migration and tumor invasiveness. Positive IHC staining for the respective vector reporters and the biliary differentiation marker (CK19) indicated that those hepatocytes which integrated mutant-*IDH1* after HTVi, in combination with *KRAS/p53,* are transformed and acquire an aggressive phenotype with the ability to migrate and invade the pancreatic tissue (Figure 16). Similar findings have been shown in published work on the establishment of a GEMM with *KRAS G12D* mutations and *p53* loss[76], as well as the recent publication from Wu and colleagues, showing that 20.4% of *AlbCre;KrasG12D;Idh1*^{R132C} animals with liver tumors, also exhibited an increased metastatic spread to the pancreatic tissue, among other organs such as kidney, lungs and peritoneum[72].

In addition, an important aspect to consider was the translational relevance of such a model and to which extent it can be translated to the human situation. Although *KRAS*, *TP53* and *IDH1* mutation have been identified as one of the most recurrent mutational events in a large cohort of human iCCA, the latter appeared to be mutually exclusive with the first alterations[34, 111]. However, activating mutations in *Kras* combined with loss of *Tp53,* have been considered as a reliable model that recapitulates the histopathological and molecular human iCCA, including tumor initiation and progression. In that GEMM model though, mixed iCC/HCC and HCC features were also found[76]. This was afterwards shown to be to some extent explained by the cell of origin, and the interplay between cellular and oncogenic mechanisms, critical in promoting hepatocyte-derived iCCA in the context of co-mutations in *Kras* and *p53*[78]. In my hands, transfection of hepatocytes with *KRAS/p53* and mutant-*IDH1* by HTVi led to the generation of rapidly growing tumors that exhibited a highly desmoplastic stroma. These tumors resembled adenocarcinoma with poorly differentiated but positive CK19 staining, in accordance with previous studies focusing on the understanding of genetic heterogeneity in iCCA[159]. Therefore, I concluded that delivery of *KRAS/p53* in combination with mutant-*IDH1* by HTVi is a suitable preclinical model to further study the molecular heterogeneity and remodelling effects on the iCCA TIME.

Furthermore, recent studies have identified different immune profiles and microenvironmental cellular composition that are related to defined oncogenic drivers of iCCA[43, 154, 160]. In this regard, I could show that the addition of mutant-*IDH1* generates a molecularly different entity. Pathway analysis of the macroscopically non-affected liver tissue derived from *KRAS/p53/IDH1 R132C*-injected animals at terminal stage, revealed an upregulation of cell proliferation and migration, inflammation and metabolism gene signatures (Figure 17). These observations were intensified at an earlier timepoint (21 days post-HTVi), where the striking differences in tumor incidence between *KRAS/p53/IDH1 R132C*-injected mice compared to the rest of the groups, were in line with the unsupervised clustering results of non-affected liver tissue by RNA-seq analysis (Figure 19).

These results, together with previous literature indicating a remodelling effect of mutant-*IDH1* in the tumor immune landscape, prompted me to further investigate the TIME of mutant-*IDH1* in the context of *KRAS/p53*-driven iCCA. I in collaboration with Dominik Vonficht could indeed determine that *KRAS/p53/IDH1 R132C* cooperate not only in accelerating tumorigenesis, but also impacts the immune microenvironment. Using spectral flow cytometry and IHC staining, I observed that the myeloid-lineage cellular abundance was significantly increased in the *IDH1 R132C*-driven group (Figure 20). Further, IHC staining for immune surface markers revealed an interesting spatial distribution of the cells, which indicated that tumors from the separate experimental groups displayed strong differences in immune cell dynamics. Interestingly, the immune cells in the small tumors found in *Empty*, *IDH1 WT* and *IDH1 R132H* in the context of *KRAS/p53,* were mostly found infiltrating the tumor tissue. In contrast, in the *KRAS/p53/IDH1 R132C* livers, while myeloid-lineage markers (CD11b, CD11c and MHC-II) were located within the tumor tissue, lymphocytes (B cell, T cells) and Kupffer cells and macrophages (F4/80) were rather found in the tumor rim and surrounding non-affected tissue (Figure 21). This could be possibly explained by the concomitant development of an immunosuppressive phenotype that inhibited the infiltration and recruitment of cytotoxic cells to the tumor site once this has already progressed to an advanced stage. This suggests and *IDH1 R132C*-specific modulation of the immune microenvironment.

Considering my previous results, I hypothesized that DCs could be the myeloid cell population contributing to this immunosuppressive environment. Published work indicates that these antigen-presenting cells have the ability to induce anti-tumor immune mechanisms that enhance tumorigenesis, by modulating T cell polarization and T_{reg} differentiation[161, 162]. To address the antigen-presenting capacity of DCs, I made use of an *ex vivo* setting in which I co-cultured the isolated DCs from livers and spleens of *KRAS/p53/IDH1 R132C*- and *KRAS/p53/IDH1 WT*-

injected mice with naïve antigen-specific OT-I and OT-II cells (Figure 22). This analysis revealed that upon OVA administration, there was a significant upregulation of the expression of surface presentation molecules such as CTLA-4, PD-L1 and CD25 specifically in $CD4^+$T cells incubated with *KRAS/p53/IDH1 R132C*-derived DCs (Figure 23). Therefore, my observations further confirm the interplay between the different immune cells in the TIME to shape the tumor development, data that is in accordance to previous publications[129, 163]. Moreover, these results were in line with previous studies showing an increased abundance of these immune checkpoint inhibitor molecules in iCCA patient samples compared to peritumoral tissue, with a correlation of CTLA-4, PD-L1 and $FOXP3^+$ (T_{reg} marker) expression with reduced overall survival[164]. Accordingly, several studies show the association between myeloid cells, specifically TAMs and MDSCs, and the response to PD-1 blockade in iCCA[46, 165, 166]. Nevertheless, Wu and colleagues using the GEMM *AlbCre;KrasG12D;Idh1*^{R132C}, showed that the recruitment of T_{regs} and increased CTLA-4 expression was induced only after inhibiting mutant-*IDH1*, leading to tumor remission after administrating the combination of AG-120 and anti-CTLA-4 antibody[72]. Considering the different molecular heterogeneity and tumor dynamics of the GEMM model and the HTVi model, a possible explanation would be linked to the remodelling effect that *IDH1* mutation plays in a determined oncogenic setting. Correspondingly, recent published work indicates that a defined tumor genotype is able to orchestrate a defined immune response and differently shape the tumor microenvironment[160].

Thus, in my experimental setting I determined that the enrichment of the myeloid cell compartment found in the *IDH1 R132C*-derived microenvironment, promoted the activation of myeloid-derived suppressor cell features, inducing a concomitant immunoregulatory phenotype and therefore compromises an anti-tumor immune response. Taken together, my results indicate the orchestration of a pro-tumorigenic microenvironment, with a cross-talk between *IDH1 R132C* tumor cells, myeloid cells and further T cell polarization, which results in an enhanced tumor progression and invasiveness. To describe more in detail the mechanisms by which *IDH1 R132C* rewires the immune dynamics in this particular oncogenic setting, and to identify potential immune-based therapeutic targets, I in collaboration with Dominik Vonficht characterized in depth the TIME of *KRAS/p53/IDH1 R132C*-driven iCCA. By designing a thorough antibody panel that included up to 27 different surface markers, I was able to better define both lymphoid and myeloid compartments not only in the liver, but also lymphatic organs (dLN and mLN) as well as spleen (Figure 24). Similar observations were found in the four organs, suggesting the orchestration of a systemic response against the tumor. First, in line with published observations, mutant-*IDH1 R132C* led to a decrease in $CD8^+$T cells and $CD4^+$T cells activation state[72, 115, 116]. Moreover, I

could confirm once more the significantly increased abundance of myeloid-lineage markers out of single CD45^{+} living cells in the *KRAS/p53/IDH1 R132C* group (Figure 25). Interestingly, analysis of the relative abundance of surface expression markers to single CD45^{+} living cells indicated that CD172a^{+} (SIRPα) cells were significantly increased in the organs from animals injected with *KRAS/p53/IDH1 R132C*. Furthermore, I found that SIRPα was commonly expressed in those populations previously identified to be significantly increased in this group, that is cDC2, TAM, MDSC and MDSC-like cells, with immunosuppressive properties (Figure 26).

Considering previous published work describing the immune checkpoint properties of SIRPα[153, 167], further experiments focused on exploring the potential of targeting SIRPα in *IDH1*-mutant iCCA. In that regard, scientific studies indicate that SIRPα blockade using monoclonal antibodies (anti-SIRPα) suppressed tumor development by promoting phagocytic activity of macrophages, in turn increasing tumor immune responses in hepatoma and colorectal adenoma cell lines, both *in vitro* and *in vivo*[168]. Mechanistically, Gauttier and colleagues recently showed that SIRPα monotherapy increases CD8+ T cell infiltration and inhibits tumor growth in a syngeneic mouse model based on the subcutaneous injection of colon adenocarcinoma cell lines[169]. Moreover, the combination therapy of anti-PD-L1/anti-SIRPα reduces tumor proliferation and invasion by increasing CD4^{+}T cell activity and blocking the immunosuppressive effect of T_{regs} and MDSCs[169]. In my experience, combination of anti-PD-L1 and anti-SIRPα blockade in *KRAS/p53/IDH1 R132C*-injected animals led to similar results, with a significant reduction in the tumor burden when compared to single treatment controls (Figure 27). In this setting, further experiments will focus on understanding the remodelling effect that this combined treatment exerts in the TIME to delay tumor progression. Due to the fact that I faced technical issues with the intravenous injections of anti-PD-L1 treatment. Some reports indicate that *KRAS* mutant-cancers tend to show higher expression of PD-L1 not only on immune cells, but also on tumor cells[170]. One possible explanation to this type of reaction would be that this antibody leads to a very strong immune response that ends in a cytokine storm. This prompts me to propose that alternative application routes may be used for future experiments.

To sum up, my scientific work indicates that *IDH1 R132C* in the context of *KRAS/p53*-driven iCCA accelerates tumorigenesis by enhancing the upregulation of cell proliferation, migration and invasion pathways. Additional mechanisms that enhance tumor growth comprise the orchestration of an immunosuppressive environment in which myeloid cells are recruited to the tumor site and act as the main drivers or the anti-tumor immune response. In this setting, myeloid cells, through mechanisms to be yet determined (either via direct cell contact and polarization of

T cells or cytokine-release), induce an immunosuppressive response that rewires T cell polarization, and contributes to further enhancing tumor progression. I determined that these myeloid cells with immunosuppressive features (MDSC, TAM and cDC2) are characterized by the immune checkpoint molecule SIRPα, suggesting a new therapeutic target for the treatment of mutant-*IDH1* iCCA (Figure 28).

Following these observations, further research is needed to understand the crosstalk between the *IDH1*-mutant tumor cells and SIRPα^{+} myeloid cells. Here, the use of co-culture systems of tumor cells and myeloid cells are important to define the mechanism by which 2-HG, as the main oncometabolite produced by mutant-*IDH1*, and other environmental factors are promoting the recruitment and differentiation state of these SIRPα^{+} cells. In order to identify the effects that SIRPα^{+} myeloid cells exert in the innate immune response, application of single cell RNA-Seq technologies in CD45^{+} living cells from *KRAS/p53/IDH1 R132C* livers would allow to decipher the transcriptional profile of the myeloid cells of interest. Besides, experiments assessing the ability of these cells to secret cytokines and chemokines that may drive an immunosuppressive phenotype are needed. Further, blockade of this target as a monotherapy or in combination with other immune checkpoints (CTLA-4 and PD-L1) may define the mechanisms by which *IDH1 R132C* remodels the TIME and promotes tumor progression.

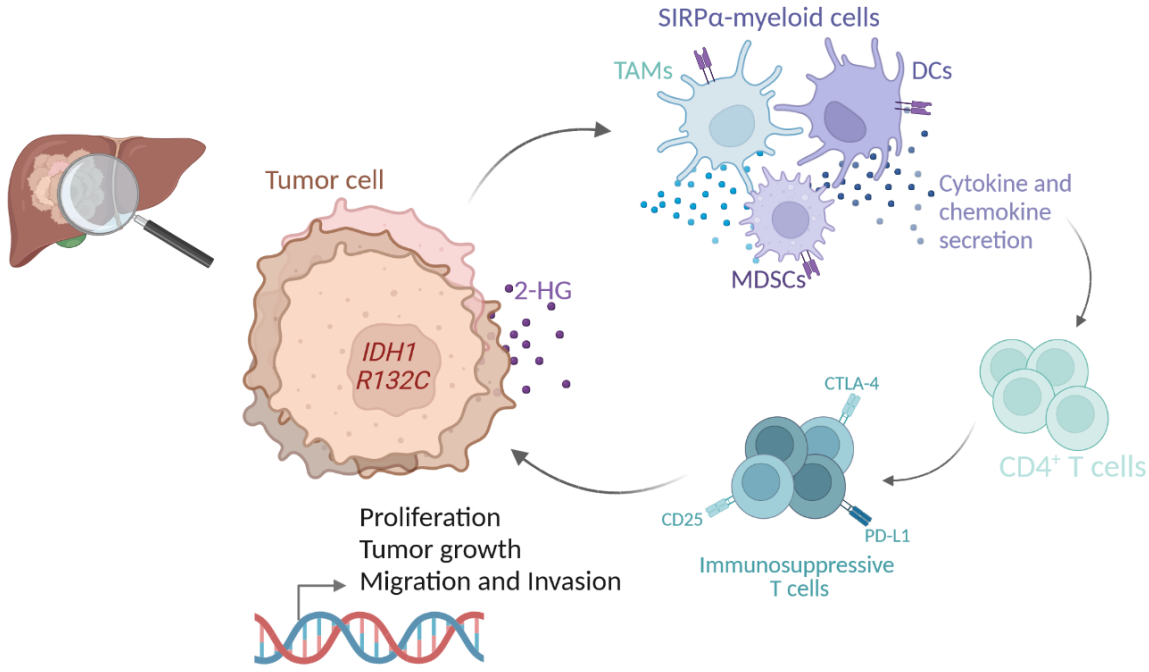

Figure 28. Illustration depicting the proposed mechanisms by which *IDH1 R132C* contributes to remodelling iCCA microenvironment. *IDH1 R132C* activates pathways involved in promoting proliferation, tumor growth, migration and invasiveness resulting in an accelerated tumor development and

decreased survival. Increased infiltration of myeloid cells (TAMs, DCs and MDSCs) characterized by SIRPα affects T cell polarization, leading to a regulatory and immunosuppressive phenotype. This anti-tumor immune response further enhances tumor progression and overall survival.

9 References

1. Sung H, Ferlay J, Siegel RL, et al. Global Cancer Statistics 2020: GLOBOCAN Estimates of Incidence and Mortality Worldwide for 36 Cancers in 185 Countries. *CA Cancer J Clin*. May 2021;71(3):209-249. doi:10.3322/caac.21660
2. Banales JM, Marin JJG, Lamarca A, et al. Cholangiocarcinoma 2020: the next horizon in mechanisms and management. *Nat Rev Gastroenterol Hepatol*. Sep 2020;17(9):557-588. doi:10.1038/s41575-020-0310-z
3. Borger DR, Tanabe KK, Fan KC, et al. Frequent mutation of isocitrate dehydrogenase (IDH)1 and IDH2 in cholangiocarcinoma identified through broad-based tumor genotyping. *Oncologist*. 2012;17(1):72-9. doi:10.1634/theoncologist.2011-0386
4. Arun J. Sanyal TDB, Norah A Terrault, K. D. L. *Zakim and Boyer's Hepatology*. Elsevier; 2017.
5. Lorente S, Hautefeuille M, Sanchez-Cedillo A. The liver, a functionalized vascular structure. *Sci Rep*. Oct 1 2020;10(1):16194. doi:10.1038/s41598-020-73208-8
6. Kietzmann T. Metabolic zonation of the liver: The oxygen gradient revisited. *Redox Biol*. Apr 2017;11:622-630. doi:10.1016/j.redox.2017.01.012
7. Li X, Ramadori P, Pfister D, Seehawer M, Zender L, Heikenwalder M. The immunological and metabolic landscape in primary and metastatic liver cancer. *Nat Rev Cancer*. Sep 2021;21(9):541-557. doi:10.1038/s41568-021-00383-9
8. Gordillo M, Evans T, Gouon-Evans V. Orchestrating liver development. *Development*. Jun 15 2015;142(12):2094-108. doi:10.1242/dev.114215
9. Sahoo S, Mishra A, Diehl AM, Jolly MK. Dynamics of hepatocyte-cholangiocyte cell-fate decisions during liver development and regeneration. *iScience*. Sep 16 2022;25(9):104955. doi:10.1016/j.isci.2022.104955
10. Weiskirchen R, Tacke F. Cellular and molecular functions of hepatic stellate cells in inflammatory responses and liver immunology. *Hepatobiliary Surg Nutr*. Dec 2014;3(6):344-63. doi:10.3978/j.issn.2304-3881.2014.11.03
11. Robinson MW, Harmon C, O'Farrelly C. Liver immunology and its role in inflammation and homeostasis. *Cell Mol Immunol*. May 2016;13(3):267-76. doi:10.1038/cmi.2016.3
12. Rumgay H, Arnold M, Ferlay J, et al. Global burden of primary liver cancer in 2020 and predictions to 2040. *J Hepatol*. Dec 2022;77(6):1598-1606. doi:10.1016/j.jhep.2022.08.021
13. Finn RS, Qin S, Ikeda M, et al. Atezolizumab plus Bevacizumab in Unresectable Hepatocellular Carcinoma. *N Engl J Med*. May 14 2020;382(20):1894-1905. doi:10.1056/NEJMoa1915745
14. Llovet JM, Castet F, Heikenwalder M, et al. Immunotherapies for hepatocellular carcinoma. *Nat Rev Clin Oncol*. Mar 2022;19(3):151-172. doi:10.1038/s41571-021-00573-2
15. Ramai D, Ofosu A, Lai JK, Reddy M, Adler DG. Combined Hepatocellular Cholangiocarcinoma: A Population-Based Retrospective Study. *Am J Gastroenterol*. Sep 2019;114(9):1496-1501. doi:10.14309/ajg.0000000000000326
16. Sia D, Villanueva A, Friedman SL, Llovet JM. Liver Cancer Cell of Origin, Molecular Class, and Effects on Patient Prognosis. *Gastroenterology*. Mar 2017;152(4):745-761. doi:10.1053/j.gastro.2016.11.048
17. Ahn DH, Bekaii-Saab T. Biliary cancer: intrahepatic cholangiocarcinoma vs. extrahepatic cholangiocarcinoma vs. gallbladder cancers: classification and therapeutic implications. *J Gastrointest Oncol*. Apr 2017;8(2):293-301. doi:10.21037/jgo.2016.10.01
18. Nakanuma Y, Kakuda Y. Pathologic classification of cholangiocarcinoma: New concepts. *Best Pract Res Clin Gastroenterol*. Apr 2015;29(2):277-93. doi:10.1016/j.bpg.2015.02.006

19. Carpino G, Cardinale V, Folseraas T, et al. Neoplastic Transformation of the Peribiliary Stem Cell Niche in Cholangiocarcinoma Arisen in Primary Sclerosing Cholangitis. *Hepatology*. Feb 2019;69(2):622-638. doi:10.1002/hep.30210
20. Nagtegaal ID, Odze RD, Klimstra D, et al. The 2019 WHO classification of tumours of the digestive system. *Histopathology*. Jan 2020;76(2):182-188. doi:10.1111/his.13975
21. Khan SA, Tavolari S, Brandi G. Cholangiocarcinoma: Epidemiology and risk factors. *Liver Int*. May 2019;39 Suppl 1:19-31. doi:10.1111/liv.14095
22. Bertuccio P, Malvezzi M, Carioli G, et al. Global trends in mortality from intrahepatic and extrahepatic cholangiocarcinoma. *J Hepatol*. Jul 2019;71(1):104-114. doi:10.1016/j.jhep.2019.03.013
23. Valle J, Wasan H, Palmer DH, et al. Cisplatin plus gemcitabine versus gemcitabine for biliary tract cancer. *N Engl J Med*. Apr 8 2010;362(14):1273-81. doi:10.1056/NEJMoa0908721
24. Vithayathil M, Khan SA. Current epidemiology of cholangiocarcinoma in Western countries. *J Hepatol*. Dec 2022;77(6):1690-1698. doi:10.1016/j.jhep.2022.07.022
25. Kendall T, Verheij J, Gaudio E, et al. Anatomical, histomorphological and molecular classification of cholangiocarcinoma. *Liver Int*. May 2019;39 Suppl 1:7-18. doi:10.1111/liv.14093
26. Lim JH. Cholangiocarcinoma: morphologic classification according to growth pattern and imaging findings. *AJR Am J Roentgenol*. Sep 2003;181(3):819-27. doi:10.2214/ajr.181.3.1810819
27. Moeini A, Haber PK, Sia D. Cell of origin in biliary tract cancers and clinical implications. *JHEP Rep*. Apr 2021;3(2):100226. doi:10.1016/j.jhepr.2021.100226
28. Saha SK, Parachoniak CA, Ghanta KS, et al. Mutant IDH inhibits HNF-4alpha to block hepatocyte differentiation and promote biliary cancer. *Nature*. Sep 4 2014;513(7516):110-4. doi:10.1038/nature13441
29. Zender S, Nickeleit I, Wuestefeld T, et al. A critical role for notch signaling in the formation of cholangiocellular carcinomas. *Cancer Cell*. Jun 10 2013;23(6):784-95. doi:10.1016/j.ccr.2013.04.019
30. Fan B, Malato Y, Calvisi DF, et al. Cholangiocarcinomas can originate from hepatocytes in mice. *J Clin Invest*. Aug 2012;122(8):2911-5. doi:10.1172/JCI63212
31. Churi CR, Shroff R, Wang Y, et al. Mutation profiling in cholangiocarcinoma: prognostic and therapeutic implications. *PLoS One*. 2014;9(12):e115383. doi:10.1371/journal.pone.0115383
32. Yang X, Wang W, Wang C, et al. Characterization of EGFR family gene aberrations in cholangiocarcinoma. *Oncol Rep*. Aug 2014;32(2):700-8. doi:10.3892/or.2014.3261
33. Sia D, Hoshida Y, Villanueva A, et al. Integrative molecular analysis of intrahepatic cholangiocarcinoma reveals 2 classes that have different outcomes. *Gastroenterology*. Apr 2013;144(4):829-40. doi:10.1053/j.gastro.2013.01.001
34. Andersen JB, Thorgeirsson SS. Genetic profiling of intrahepatic cholangiocarcinoma. *Curr Opin Gastroenterol*. May 2012;28(3):266-72. doi:10.1097/MOG.0b013e3283523c7e
35. Ding X, He M, Chan AWH, et al. Genomic and Epigenomic Features of Primary and Recurrent Hepatocellular Carcinomas. *Gastroenterology*. Dec 2019;157(6):1630-1645 e6. doi:10.1053/j.gastro.2019.09.005
36. Carapeto F, Bozorgui B, Shroff RT, et al. The immunogenomic landscape of resected intrahepatic cholangiocarcinoma. *Hepatology*. Feb 2022;75(2):297-308. doi:10.1002/hep.32150
37. Arai Y, Totoki Y, Hosoda F, et al. Fibroblast growth factor receptor 2 tyrosine kinase fusions define a unique molecular subtype of cholangiocarcinoma. *Hepatology*. Apr 2014;59(4):1427-34. doi:10.1002/hep.26890
38. Wang P, Dong Q, Zhang C, et al. Mutations in isocitrate dehydrogenase 1 and 2 occur frequently in intrahepatic cholangiocarcinomas and share hypermethylation targets with glioblastomas. *Oncogene*. Jun 20 2013;32(25):3091-100. doi:10.1038/onc.2012.315

39. Cleary JM, Raghavan S, Wu Q, et al. FGFR2 Extracellular Domain In-Frame Deletions Are Therapeutically Targetable Genomic Alterations That Function as Oncogenic Drivers in Cholangiocarcinoma. *Cancer Discov*. Oct 2021;11(10):2488-2505. doi:10.1158/2159-8290.CD-20-1669
40. Borad MJ, Champion MD, Egan JB, et al. Integrated genomic characterization reveals novel, therapeutically relevant drug targets in FGFR and EGFR pathways in sporadic intrahepatic cholangiocarcinoma. *PLoS Genet*. Feb 2014;10(2):e1004135. doi:10.1371/journal.pgen.1004135
41. Newell-Price J, Clark AJ, King P. DNA methylation and silencing of gene expression. *Trends Endocrinol Metab*. May-Jun 2000;11(4):142-8. doi:10.1016/s1043-2760(00)00248-4
42. Yang YM, Kim SY, Seki E. Inflammation and Liver Cancer: Molecular Mechanisms and Therapeutic Targets. *Semin Liver Dis*. Feb 2019;39(1):26-42. doi:10.1055/s-0038-1676806
43. Affo S, Nair A, Brundu F, et al. Promotion of cholangiocarcinoma growth by diverse cancer-associated fibroblast subpopulations. *Cancer Cell*. Jun 14 2021;39(6):866-882 e11. doi:10.1016/j.ccell.2021.03.012
44. Fabris L, Sato K, Alpini G, Strazzabosco M. The Tumor Microenvironment in Cholangiocarcinoma Progression. *Hepatology*. Jan 2021;73 Suppl 1(Suppl 1):75-85. doi:10.1002/hep.31410
45. Greten TF, Schwabe R, Bardeesy N, et al. Immunology and immunotherapy of cholangiocarcinoma. *Nat Rev Gastroenterol Hepatol*. Jan 25 2023;doi:10.1038/s41575-022-00741-4
46. Loeuillard E, Yang J, Buckarma E, et al. Targeting tumor-associated macrophages and granulocytic myeloid-derived suppressor cells augments PD-1 blockade in cholangiocarcinoma. *J Clin Invest*. Oct 1 2020;130(10):5380-5396. doi:10.1172/JCI137110
47. Ware MB, Zaidi MY, Yang J, et al. Suppressive myeloid cells are expanded by biliary tract cancer-derived cytokines in vitro and associate with aggressive disease. *Br J Cancer*. Oct 2020;123(9):1377-1386. doi:10.1038/s41416-020-1018-0
48. Zhou Z, Wang P, Sun R, et al. Tumor-associated neutrophils and macrophages interaction contributes to intrahepatic cholangiocarcinoma progression by activating STAT3. *J Immunother Cancer*. Mar 2021;9(3)doi:10.1136/jitc-2020-001946
49. Konishi D, Umeda Y, Yoshida K, et al. Regulatory T cells induce a suppressive immune milieu and promote lymph node metastasis in intrahepatic cholangiocarcinoma. *Br J Cancer*. Sep 2022;127(4):757-765. doi:10.1038/s41416-022-01838-y
50. Kitano Y, Okabe H, Yamashita YI, et al. Tumour-infiltrating inflammatory and immune cells in patients with extrahepatic cholangiocarcinoma. *Br J Cancer*. Jan 2018;118(2):171-180. doi:10.1038/bjc.2017.401
51. Guo Y, Feng K, Liu Y, et al. Phase I Study of Chimeric Antigen Receptor-Modified T Cells in Patients with EGFR-Positive Advanced Biliary Tract Cancers. *Clin Cancer Res*. Mar 15 2018;24(6):1277-1286. doi:10.1158/1078-0432.CCR-17-0432
52. Wathikthinnakon M, Luangwattananun P, Sawasdee N, et al. Combination gemcitabine and PD-L1xCD3 bispecific T cell engager (BiTE) enhances T lymphocyte cytotoxicity against cholangiocarcinoma cells. *Sci Rep*. Apr 13 2022;12(1):6154. doi:10.1038/s41598-022-09964-6
53. Piha-Paul SA, Oh DY, Ueno M, et al. Efficacy and safety of pembrolizumab for the treatment of advanced biliary cancer: Results from the KEYNOTE-158 and KEYNOTE-028 studies. *Int J Cancer*. Oct 15 2020;147(8):2190-2198. doi:10.1002/ijc.33013
54. Ueno M, Ikeda M, Morizane C, et al. Nivolumab alone or in combination with cisplatin plus gemcitabine in Japanese patients with unresectable or recurrent biliary tract cancer: a non-randomised, multicentre, open-label, phase 1 study. *Lancet Gastroenterol Hepatol*. Aug 2019;4(8):611-621. doi:10.1016/S2468-1253(19)30086-X

55. Doki Y, Ueno M, Hsu CH, et al. Tolerability and efficacy of durvalumab, either as monotherapy or in combination with tremelimumab, in patients from Asia with advanced biliary tract, esophageal, or head-and-neck cancer. *Cancer Med*. Jul 2022;11(13):2550-2560. doi:10.1002/cam4.4593
56. Oh DY, Lee KH, Lee DW, et al. Gemcitabine and cisplatin plus durvalumab with or without tremelimumab in chemotherapy-naive patients with advanced biliary tract cancer: an open-label, single-centre, phase 2 study. *Lancet Gastroenterol Hepatol*. Jun 2022;7(6):522-532. doi:10.1016/S2468-1253(22)00043-7
57. Calvisi DF, Boulter L, Vaquero J, et al. Criteria for preclinical models of cholangiocarcinoma: scientific and medical relevance. *Nat Rev Gastroenterol Hepatol*. Feb 8 2023;doi:10.1038/s41575-022-00739-y
58. Cekanova M, Rathore K. Animal models and therapeutic molecular targets of cancer: utility and limitations. *Drug Des Devel Ther*. 2014;8:1911-21. doi:10.2147/DDDT.S49584
59. Saito Y, Muramatsu T, Kanai Y, et al. Establishment of Patient-Derived Organoids and Drug Screening for Biliary Tract Carcinoma. *Cell Rep*. Apr 23 2019;27(4):1265-1276 e4. doi:10.1016/j.celrep.2019.03.088
60. Loeuillard E, Fischbach SR, Gores GJ, Rizvi S. Animal models of cholangiocarcinoma. *Biochim Biophys Acta Mol Basis Dis*. May 1 2019;1865(5):982-992. doi:10.1016/j.bbadis.2018.03.026
61. Mohr R, Ozdirik B, Knorr J, et al. In Vivo Models for Cholangiocarcinoma-What Can We Learn for Human Disease? *Int J Mol Sci*. Jul 15 2020;21(14)doi:10.3390/ijms21144993
62. Vallejo A, Erice O, Entrialgo-Cadierno R, et al. FOSL1 promotes cholangiocarcinoma via transcriptional effectors that could be therapeutically targeted. *J Hepatol*. Aug 2021;75(2):363-376. doi:10.1016/j.jhep.2021.03.028
63. Saborowski A, Wolff K, Spielberg S, et al. Murine Liver Organoids as a Genetically Flexible System to Study Liver Cancer In Vivo and In Vitro. *Hepatol Commun*. Mar 2019;3(3):423-436. doi:10.1002/hep4.1312
64. Fitzhugh OG, Nelson AA. Liver Tumors in Rats Fed Thiourea or Thioacetamide. *Science*. Dec 3 1948;108(2814):626-8. doi:10.1126/science.108.2814.626
65. Al-Bader A, Mathew TC, Abul H, Al-Sayer H, Singal PK, Dashti HM. Cholangiocarcinoma and liver cirrhosis in relation to changes due to thioacetamide. *Mol Cell Biochem*. May 2000;208(1-2):1-10. doi:10.1023/a:1007082515548
66. Sekiya S, Suzuki A. Intrahepatic cholangiocarcinoma can arise from Notch-mediated conversion of hepatocytes. *J Clin Invest*. Nov 2012;122(11):3914-8. doi:10.1172/JCI63065
67. Cubero FJ, Mohamed MR, Woitok MM, et al. Loss of c-Jun N-terminal Kinase 1 and 2 Function in Liver Epithelial Cells Triggers Biliary Hyperproliferation Resembling Cholangiocarcinoma. *Hepatol Commun*. Jun 2020;4(6):834-851. doi:10.1002/hep4.1495
68. Walesky C, Edwards G, Borude P, et al. Hepatocyte nuclear factor 4 alpha deletion promotes diethylnitrosamine-induced hepatocellular carcinoma in rodents. *Hepatology*. Jun 2013;57(6):2480-90. doi:10.1002/hep.26251
69. Maronpot RR, Giles HD, Dykes DJ, Irwin RD. Furan-induced hepatic cholangiocarcinomas in Fischer 344 rats. *Toxicol Pathol*. 1991;19(4 Pt 2):561-70. doi:10.1177/019262339101900401
70. Farazi PA, Zeisberg M, Glickman J, Zhang Y, Kalluri R, DePinho RA. Chronic bile duct injury associated with fibrotic matrix microenvironment provokes cholangiocarcinoma in p53-deficient mice. *Cancer Res*. Jul 1 2006;66(13):6622-7. doi:10.1158/0008-5472.CAN-05-4609
71. Katz SF, Lechel A, Obenauf AC, et al. Disruption of Trp53 in livers of mice induces formation of carcinomas with bilineal differentiation. *Gastroenterology*. May 2012;142(5):1229-1239 e3. doi:10.1053/j.gastro.2012.02.009

72. Wu MJ, Shi L, Dubrot J, et al. Mutant IDH Inhibits IFNgamma-TET2 Signaling to Promote Immunoevasion and Tumor Maintenance in Cholangiocarcinoma. *Cancer Discov*. Mar 1 2022;12(3):812-835. doi:10.1158/2159-8290.CD-21-1077
73. Ikenoue T, Terakado Y, Nakagawa H, et al. A novel mouse model of intrahepatic cholangiocarcinoma induced by liver-specific Kras activation and Pten deletion. *Sci Rep*. Apr 1 2016;6:23899. doi:10.1038/srep23899
74. Lin YK, Fang Z, Jiang TY, et al. Combination of Kras activation and PTEN deletion contributes to murine hepatopancreatic ductal malignancy. *Cancer Lett*. May 1 2018;421:161-169. doi:10.1016/j.canlet.2018.02.017
75. Xu X, Kobayashi S, Qiao W, et al. Induction of intrahepatic cholangiocellular carcinoma by liver-specific disruption of Smad4 and Pten in mice. *J Clin Invest*. Jul 2006;116(7):1843-52. doi:10.1172/JCI27282
76. O'Dell MR, Huang JL, Whitney-Miller CL, et al. Kras(G12D) and p53 mutation cause primary intrahepatic cholangiocarcinoma. *Cancer Res*. Mar 15 2012;72(6):1557-67. doi:10.1158/0008-5472.CAN-11-3596
77. El Khatib M, Bozko P, Palagani V, Malek NP, Wilkens L, Plentz RR. Activation of Notch signaling is required for cholangiocarcinoma progression and is enhanced by inactivation of p53 in vivo. *PLoS One*. 2013;8(10):e77433. doi:10.1371/journal.pone.0077433
78. Hill MA, Alexander WB, Guo B, et al. Kras and Tp53 Mutations Cause Cholangiocyte- and Hepatocyte-Derived Cholangiocarcinoma. *Cancer Res*. Aug 15 2018;78(16):4445-4451. doi:10.1158/0008-5472.CAN-17-1123
79. Chen X, Calvisi DF. Hydrodynamic transfection for generation of novel mouse models for liver cancer research. *Am J Pathol*. Apr 2014;184(4):912-923. doi:10.1016/j.ajpath.2013.12.002
80. Zhang S, Song X, Cao D, et al. Pan-mTOR inhibitor MLN0128 is effective against intrahepatic cholangiocarcinoma in mice. *J Hepatol*. Dec 2017;67(6):1194-1203. doi:10.1016/j.jhep.2017.07.006
81. Zhang S, Wang J, Wang H, et al. Hippo Cascade Controls Lineage Commitment of Liver Tumors in Mice and Humans. *Am J Pathol*. Apr 2018;188(4):995-1006. doi:10.1016/j.ajpath.2017.12.017
82. Yuan D, Huang S, Berger E, et al. Kupffer Cell-Derived Tnf Triggers Cholangiocellular Tumorigenesis through JNK due to Chronic Mitochondrial Dysfunction and ROS. *Cancer Cell*. Jun 12 2017;31(6):771-789 e6. doi:10.1016/j.ccell.2017.05.006
83. Salati M, Caputo F, Baldessari C, et al. IDH Signalling Pathway in Cholangiocarcinoma: From Biological Rationale to Therapeutic Targeting. *Cancers (Basel)*. Nov 9 2020;12(11)doi:10.3390/cancers12113310
84. Parker SJ, Metallo CM. Metabolic consequences of oncogenic IDH mutations. *Pharmacol Ther*. Aug 2015;152:54-62. doi:10.1016/j.pharmthera.2015.05.003
85. Reitman ZJ, Yan H. Isocitrate dehydrogenase 1 and 2 mutations in cancer: alterations at a crossroads of cellular metabolism. *J Natl Cancer Inst*. Jul 7 2010;102(13):932-41. doi:10.1093/jnci/djq187
86. Yang H, Ye D, Guan KL, Xiong Y. IDH1 and IDH2 mutations in tumorigenesis: mechanistic insights and clinical perspectives. *Clin Cancer Res*. Oct 15 2012;18(20):5562-71. doi:10.1158/1078-0432.CCR-12-1773
87. Dang L, White DW, Gross S, et al. Cancer-associated IDH1 mutations produce 2-hydroxyglutarate. *Nature*. Dec 10 2009;462(7274):739-44. doi:10.1038/nature08617
88. Molenaar RJ, Maciejewski JP, Wilmink JW, van Noorden CJF. Wild-type and mutated IDH1/2 enzymes and therapy responses. *Oncogene*. Apr 2018;37(15):1949-1960. doi:10.1038/s41388-017-0077-z

89. Figueroa ME, Abdel-Wahab O, Lu C, et al. Leukemic IDH1 and IDH2 mutations result in a hypermethylation phenotype, disrupt TET2 function, and impair hematopoietic differentiation. *Cancer Cell*. Dec 14 2010;18(6):553-67. doi:10.1016/j.ccr.2010.11.015
90. Chowdhury R, Yeoh KK, Tian YM, et al. The oncometabolite 2-hydroxyglutarate inhibits histone lysine demethylases. *EMBO Rep*. May 2011;12(5):463-9. doi:10.1038/embor.2011.43
91. Pirozzi CJ, Yan H. The implications of IDH mutations for cancer development and therapy. *Nat Rev Clin Oncol*. Oct 2021;18(10):645-661. doi:10.1038/s41571-021-00521-0
92. Inoue S, Li WY, Tseng A, et al. Mutant IDH1 Downregulates ATM and Alters DNA Repair and Sensitivity to DNA Damage Independent of TET2. *Cancer Cell*. Aug 8 2016;30(2):337-348. doi:10.1016/j.ccell.2016.05.018
93. Kaminska B, Czapski B, Guzik R, Krol SK, Gielniewski B. Consequences of IDH1/2 Mutations in Gliomas and an Assessment of Inhibitors Targeting Mutated IDH Proteins. *Molecules*. Mar 9 2019;24(5)doi:10.3390/molecules24050968
94. Seok J, Yoon SH, Lee SH, Jung JH, Lee YM. The oncometabolite d-2-hydroxyglutarate induces angiogenic activity through the vascular endothelial growth factor receptor 2 signaling pathway. *Int J Oncol*. Feb 2019;54(2):753-763. doi:10.3892/ijo.2018.4649
95. Avsar T, Kose TB, Oksal MD, Turan G, Kilic T. IDH1 mutation activates mTOR signaling pathway, promotes cell proliferation and invasion in glioma cells. *Mol Biol Rep*. Oct 2022;49(10):9241-9249. doi:10.1007/s11033-022-07750-1
96. Tian W, Zhang W, Wang Y, et al. Recent advances of IDH1 mutant inhibitor in cancer therapy. *Front Pharmacol*. 2022;13:982424. doi:10.3389/fphar.2022.982424
97. Golub D, Iyengar N, Dogra S, et al. Mutant Isocitrate Dehydrogenase Inhibitors as Targeted Cancer Therapeutics. *Front Oncol*. 2019;9:417. doi:10.3389/fonc.2019.00417
98. Montesinos P, Recher C, Vives S, et al. Ivosidenib and Azacitidine in IDH1-Mutated Acute Myeloid Leukemia. *N Engl J Med*. Apr 21 2022;386(16):1519-1531. doi:10.1056/NEJMoa2117344
99. DiNardo CD, Stein EM, de Botton S, et al. Durable Remissions with Ivosidenib in IDH1-Mutated Relapsed or Refractory AML. *N Engl J Med*. Jun 21 2018;378(25):2386-2398. doi:10.1056/NEJMoa1716984
100. Zhu AX, Macarulla T, Javle MM, et al. Final Overall Survival Efficacy Results of Ivosidenib for Patients With Advanced Cholangiocarcinoma With IDH1 Mutation: The Phase 3 Randomized Clinical ClarIDHy Trial. *JAMA Oncol*. Nov 1 2021;7(11):1669-1677. doi:10.1001/jamaoncol.2021.3836
101. Stein EM, Fathi AT, DiNardo CD, et al. Enasidenib in patients with mutant IDH2 myelodysplastic syndromes: a phase 1 subgroup analysis of the multicentre, AG221-C-001 trial. *Lancet Haematol*. Apr 2020;7(4):e309-e319. doi:10.1016/S2352-3026(19)30284-4
102. Zhuang X, Pei HZ, Li T, et al. The Molecular Mechanisms of Resistance to IDH Inhibitors in Acute Myeloid Leukemia. *Front Oncol*. 2022;12:931462. doi:10.3389/fonc.2022.931462
103. Choe S, Wang H, DiNardo CD, et al. Molecular mechanisms mediating relapse following ivosidenib monotherapy in IDH1-mutant relapsed or refractory AML. *Blood Adv*. May 12 2020;4(9):1894-1905. doi:10.1182/bloodadvances.2020001503
104. Intlekofer AM, Shih AH, Wang B, et al. Acquired resistance to IDH inhibition through trans or cis dimer-interface mutations. *Nature*. Jul 2018;559(7712):125-129. doi:10.1038/s41586-018-0251-7
105. Mardis ER, Ding L, Dooling DJ, et al. Recurring mutations found by sequencing an acute myeloid leukemia genome. *N Engl J Med*. Sep 10 2009;361(11):1058-66. doi:10.1056/NEJMoa0903840
106. Kang MR, Kim MS, Oh JE, et al. Mutational analysis of IDH1 codon 132 in glioblastomas and other common cancers. *Int J Cancer*. Jul 15 2009;125(2):353-5. doi:10.1002/ijc.24379

107. Zhang X, Miao R, Liu T, et al. IDH1 as a frequently mutated gene has potential effect on exosomes releasement by epigenetically regulating P2RX7 in intrahepatic cholangiocarcinoma. *Biomed Pharmacother*. May 2019;113:108774. doi:10.1016/j.biopha.2019.108774
108. Wang XY, Zhu WW, Wang Z, et al. Driver mutations of intrahepatic cholangiocarcinoma shape clinically relevant genomic clusters with distinct molecular features and therapeutic vulnerabilities. *Theranostics*. 2022;12(1):260-276. doi:10.7150/thno.63417
109. Voss JS, Holtegaard LM, Kerr SE, et al. Molecular profiling of cholangiocarcinoma shows potential for targeted therapy treatment decisions. *Hum Pathol*. Jul 2013;44(7):1216-22. doi:10.1016/j.humpath.2012.11.006
110. Farshidfar F, Zheng S, Gingras MC, et al. Integrative Genomic Analysis of Cholangiocarcinoma Identifies Distinct IDH-Mutant Molecular Profiles. *Cell Rep*. Mar 14 2017;18(11):2780-2794. doi:10.1016/j.celrep.2017.02.033
111. Nepal C, O'Rourke CJ, Oliveira D, et al. Genomic perturbations reveal distinct regulatory networks in intrahepatic cholangiocarcinoma. *Hepatology*. Sep 2018;68(3):949-963. doi:10.1002/hep.29764
112. Boerner T, Drill E, Pak LM, et al. Genetic Determinants of Outcome in Intrahepatic Cholangiocarcinoma. *Hepatology*. Sep 2021;74(3):1429-1444. doi:10.1002/hep.31829
113. Goeppert B, Toth R, Singer S, et al. Integrative Analysis Defines Distinct Prognostic Subgroups of Intrahepatic Cholangiocarcinoma. *Hepatology*. May 2019;69(5):2091-2106. doi:10.1002/hep.30493
114. Kohanbash G, Carrera DA, Shrivastav S, et al. Isocitrate dehydrogenase mutations suppress STAT1 and CD8+ T cell accumulation in gliomas. *J Clin Invest*. Apr 3 2017;127(4):1425-1437. doi:10.1172/JCI90644
115. Bunse L, Pusch S, Bunse T, et al. Suppression of antitumor T cell immunity by the oncometabolite (R)-2-hydroxyglutarate. *Nat Med*. Aug 2018;24(8):1192-1203. doi:10.1038/s41591-018-0095-6
116. Notarangelo G, Spinelli JB, Perez EM, et al. Oncometabolite d-2HG alters T cell metabolism to impair CD8(+) T cell function. *Science*. Sep 30 2022;377(6614):1519-1529. doi:10.1126/science.abj5104
117. Friedrich M, Sankowski R, Bunse L, et al. Tryptophan metabolism drives dynamic immunosuppressive myeloid states in IDH-mutant gliomas. *Nat Cancer*. Jul 2021;2(7):723-740. doi:10.1038/s43018-021-00201-z
118. Friedrich M, Hahn M, Michel J, et al. Dysfunctional dendritic cells limit antigen-specific T cell response in glioma. *Neuro Oncol*. Feb 14 2023;25(2):263-276. doi:10.1093/neuonc/noac138
119. Xiang X, Liu Z, Zhang C, et al. IDH Mutation Subgroup Status Associates with Intratumor Heterogeneity and the Tumor Microenvironment in Intrahepatic Cholangiocarcinoma. *Adv Sci (Weinh)*. Sep 2021;8(17):e2101230. doi:10.1002/advs.202101230
120. Platten M, Bunse L, Wick A, et al. A vaccine targeting mutant IDH1 in newly diagnosed glioma. *Nature*. Apr 2021;592(7854):463-468. doi:10.1038/s41586-021-03363-z
121. Cao J, Wu L, Zhang SM, et al. An easy and efficient inducible CRISPR/Cas9 platform with improved specificity for multiple gene targeting. *Nucleic Acids Res*. Nov 2 2016;44(19):e149. doi:10.1093/nar/gkw660
122. Labun K, Montague TG, Krause M, Torres Cleuren YN, Tjeldnes H, Valen E. CHOPCHOP v3: expanding the CRISPR web toolbox beyond genome editing. *Nucleic Acids Res*. Jul 2 2019;47(W1):W171-W174. doi:10.1093/nar/gkz365
123. Suda T, Liu D. Hydrodynamic gene delivery: its principles and applications. *Mol Ther*. Dec 2007;15(12):2063-9. doi:10.1038/sj.mt.6300314

124. Ashhurst TM, Marsh-Wakefield F, Putri GH, et al. Integration, exploration, and analysis of high-dimensional single-cell cytometry data using Spectre. *Cytometry A*. Mar 2022;101(3):237-253. doi:10.1002/cyto.a.24350
125. Korsunsky I, Millard N, Fan J, et al. Fast, sensitive and accurate integration of single-cell data with Harmony. *Nat Methods*. Dec 2019;16(12):1289-1296. doi:10.1038/s41592-019-0619-0
126. Van Gassen S, Callebaut B, Van Helden MJ, et al. FlowSOM: Using self-organizing maps for visualization and interpretation of cytometry data. *Cytometry A*. Jul 2015;87(7):636-45. doi:10.1002/cyto.a.22625
127. Bodenheimer T, Halappanavar M, Jefferys S, et al. FastPG: Fast clustering of millions of single cells. *bioRxiv*. 2020:2020.06.19.159749. doi:10.1101/2020.06.19.159749
128. Gayoso A, Steier Z, Lopez R, et al. Joint probabilistic modeling of single-cell multi-omic data with totalVI. *Nat Methods*. Mar 2021;18(3):272-282. doi:10.1038/s41592-020-01050-x
129. Hernandez-Malmierca P, Vonficht D, Schnell A, et al. Antigen presentation safeguards the integrity of the hematopoietic stem cell pool. *Cell Stem Cell*. May 5 2022;29(5):760-775 e10. doi:10.1016/j.stem.2022.04.007
130. Uran S, Landmark KE, Hjellum G, Skotland T. Quantification of 13C pyruvate and 13C lactate in dog blood by reversed-phase liquid chromatography-electrospray ionization mass spectrometry after derivatization with 3-nitrophenylhydrazine. *J Pharm Biomed Anal*. Aug 15 2007;44(4):947-54. doi:10.1016/j.jpba.2007.04.001
131. Sorge S, Theelke J, Altbürger C, Lohmann I. An ATF4-mediated transcriptional adaptation of electron transport chain disturbance primes progenitor cells for proliferation in vivo. *bioRxiv*. 2018:425744. doi:10.1101/425744
132. Delaunay S, Pascual G, Feng B, et al. Mitochondrial RNA modifications shape metabolic plasticity in metastasis. *Nature*. Jul 2022;607(7919):593-603. doi:10.1038/s41586-022-04898-5
133. Ernst P, Glatting KH, Suhai S. A task framework for the web interface W2H. *Bioinformatics*. Jan 22 2003;19(2):278-82. doi:10.1093/bioinformatics/19.2.278
134. Dobin A, Davis CA, Schlesinger F, et al. STAR: ultrafast universal RNA-seq aligner. *Bioinformatics*. Jan 1 2013;29(1):15-21. doi:10.1093/bioinformatics/bts635
135. Anders S, Pyl PT, Huber W. HTSeq – A Python framework to work with high-throughput sequencing data. *bioRxiv*. 2014:002824. doi:10.1101/002824
136. Wu T, Hu E, Xu S, et al. clusterProfiler 4.0: A universal enrichment tool for interpreting omics data. *Innovation (Camb)*. Aug 28 2021;2(3):100141. doi:10.1016/j.xinn.2021.100141
137. Yu G, Wang LG, Han Y, He QY. clusterProfiler: an R package for comparing biological themes among gene clusters. *OMICS*. May 2012;16(5):284-7. doi:10.1089/omi.2011.0118
138. Triana S, Vonficht D, Jopp-Saile L, et al. Single-cell proteo-genomic reference maps of the hematopoietic system enable the purification and massive profiling of precisely defined cell states. *Nat Immunol*. Dec 2021;22(12):1577-1589. doi:10.1038/s41590-021-01059-0
139. Ruiz de Galarreta M, Bresnahan E, Molina-Sanchez P, et al. beta-Catenin Activation Promotes Immune Escape and Resistance to Anti-PD-1 Therapy in Hepatocellular Carcinoma. *Cancer Discov*. Aug 2019;9(8):1124-1141. doi:10.1158/2159-8290.CD-19-0074
140. Chen LL, Kung YA, Weng KF, Lin JY, Horng JT, Shih SR. Enterovirus 71 infection cleaves a negative regulator for viral internal ribosomal entry site-driven translation. *J Virol*. Apr 2013;87(7):3828-38. doi:10.1128/JVI.02278-12
141. Pusch S, Schweizer L, Beck AC, et al. D-2-Hydroxyglutarate producing neo-enzymatic activity inversely correlates with frequency of the type of isocitrate dehydrogenase 1 mutations found in glioma. *Acta Neuropathol Commun*. Feb 14 2014;2:19. doi:10.1186/2051-5960-2-19
142. Kang TW, Yevsa T, Woller N, et al. Senescence surveillance of pre-malignant hepatocytes limits liver cancer development. *Nature*. Nov 9 2011;479(7374):547-51. doi:10.1038/nature10599

143. Skelton D, Satake N, Kohn DB. The enhanced green fluorescent protein (eGFP) is minimally immunogenic in C57BL/6 mice. *Gene Ther*. Dec 2001;8(23):1813-4. doi:10.1038/sj.gt.3301586
144. Calvisi DF, Wang C, Ho C, et al. Increased lipogenesis, induced by AKT-mTORC1-RPS6 signaling, promotes development of human hepatocellular carcinoma. *Gastroenterology*. Mar 2011;140(3):1071-83. doi:10.1053/j.gastro.2010.12.006
145. Cerami E, Gao J, Dogrusoz U, et al. The cBio cancer genomics portal: an open platform for exploring multidimensional cancer genomics data. *Cancer Discov*. May 2012;2(5):401-4. doi:10.1158/2159-8290.CD-12-0095
146. Peraldo-Neia C, Scatolini M, Grosso E, et al. Assessment of a High Sensitivity Method for Identification of IDH1 R132x Mutations in Tumors and Plasma of Intrahepatic Cholangiocarcinoma Patients. *Cancers (Basel)*. Mar 30 2019;11(4)doi:10.3390/cancers11040454
147. Corti F, Nichetti F, Raimondi A, et al. Targeting the PI3K/AKT/mTOR pathway in biliary tract cancers: A review of current evidences and future perspectives. *Cancer Treat Rev*. Jan 2019;72:45-55. doi:10.1016/j.ctrv.2018.11.001
148. Ding N, Che L, Li XL, et al. Oncogenic potential of IDH1R132C mutant in cholangiocarcinoma development in mice. *World J Gastroenterol*. Feb 14 2016;22(6):2071-80. doi:10.3748/wjg.v22.i6.2071
149. Murphy KW, C. *Janeway´s Immunobiology*. 9th Edition ed. Garland Science; 2016.
150. Shurin GV, Ma Y, Shurin MR. Immunosuppressive mechanisms of regulatory dendritic cells in cancer. *Cancer Microenviron*. Aug 2013;6(2):159-67. doi:10.1007/s12307-013-0133-3
151. Dikiy S, Rudensky AY. Principles of regulatory T cell function. *Immunity*. Feb 14 2023;56(2):240-255. doi:10.1016/j.immuni.2023.01.004
152. Lewinsky H, Gunes EG, David K, et al. CD84 is a regulator of the immunosuppressive microenvironment in multiple myeloma. *JCI Insight*. Feb 22 2021;6(4)doi:10.1172/jci.insight.141683
153. Matlung HL, Szilagyi K, Barclay NA, van den Berg TK. The CD47-SIRPalpha signaling axis as an innate immune checkpoint in cancer. *Immunol Rev*. Mar 2017;276(1):145-164. doi:10.1111/imr.12527
154. Molina-Sanchez P, Ruiz de Galarreta M, Yao MA, et al. Cooperation Between Distinct Cancer Driver Genes Underlies Intertumor Heterogeneity in Hepatocellular Carcinoma. *Gastroenterology*. Dec 2020;159(6):2203-2220 e14. doi:10.1053/j.gastro.2020.08.015
155. Mehta A, Merkel OM. Immunogenicity of Cas9 Protein. *J Pharm Sci*. Jan 2020;109(1):62-67. doi:10.1016/j.xphs.2019.10.003
156. He LZ, Bhaumik M, Tribioli C, et al. Two critical hits for promyelocytic leukemia. *Mol Cell*. Nov 2000;6(5):1131-41. doi:10.1016/s1097-2765(00)00111-8
157. Avellaneda Matteo D, Grunseth AJ, Gonzalez ER, et al. Molecular mechanisms of isocitrate dehydrogenase 1 (IDH1) mutations identified in tumors: The role of size and hydrophobicity at residue 132 on catalytic efficiency. *J Biol Chem*. May 12 2017;292(19):7971-7983. doi:10.1074/jbc.M117.776179
158. Saha SK, Parachoniak CA, Bardeesy N. IDH mutations in liver cell plasticity and biliary cancer. *Cell Cycle*. 2014;13(20):3176-82. doi:10.4161/15384101.2014.965054
159. Younger NT, Wilson ML, Martinez Lyons A, et al. In Vivo Modeling of Patient Genetic Heterogeneity Identifies New Ways to Target Cholangiocarcinoma. *Cancer Res*. Apr 15 2022;82(8):1548-1559. doi:10.1158/0008-5472.CAN-21-2556
160. Martin-Serrano MA, Kepecs B, Torres-Martin M, et al. Novel microenvironment-based classification of intrahepatic cholangiocarcinoma with therapeutic implications. *Gut*. Apr 2023;72(4):736-748. doi:10.1136/gutjnl-2021-326514
161. Maldonado RA, von Andrian UH. How tolerogenic dendritic cells induce regulatory T cells. *Adv Immunol*. 2010;108:111-65. doi:10.1016/B978-0-12-380995-7.00004-5

162. Ma Y, Shurin GV, Gutkin DW, Shurin MR. Tumor associated regulatory dendritic cells. *Semin Cancer Biol*. Aug 2012;22(4):298-306. doi:10.1016/j.semcancer.2012.02.010
163. Cohen M, Giladi A, Barboy O, et al. The interaction of CD4(+) helper T cells with dendritic cells shapes the tumor microenvironment and immune checkpoint blockade response. *Nat Cancer*. Mar 2022;3(3):303-317. doi:10.1038/s43018-022-00338-5
164. Guo XJ, Lu JC, Zeng HY, et al. CTLA-4 Synergizes With PD1/PD-L1 in the Inhibitory Tumor Microenvironment of Intrahepatic Cholangiocarcinoma. *Front Immunol*. 2021;12:705378. doi:10.3389/fimmu.2021.705378
165. Diggs LP, Ruf B, Ma C, et al. CD40-mediated immune cell activation enhances response to anti-PD-1 in murine intrahepatic cholangiocarcinoma. *J Hepatol*. May 2021;74(5):1145-1154. doi:10.1016/j.jhep.2020.11.037
166. Togashi Y, Shitara K, Nishikawa H. Regulatory T cells in cancer immunosuppression - implications for anticancer therapy. *Nat Rev Clin Oncol*. Jun 2019;16(6):356-371. doi:10.1038/s41571-019-0175-7
167. Zhou Z, Chen MM, Luo Y, et al. Tumor-intrinsic SIRPA promotes sensitivity to checkpoint inhibition immunotherapy in melanoma. *Cancer Cell*. Nov 14 2022;40(11):1324-1340 e8. doi:10.1016/j.ccell.2022.10.012
168. Abe T, Tanaka Y, Piao J, et al. Signal regulatory protein alpha blockade potentiates tumoricidal effects of macrophages on gastroenterological neoplastic cells in syngeneic immunocompetent mice. *Ann Gastroenterol Surg*. Nov 2018;2(6):451-462. doi:10.1002/ags3.12205
169. Gauttier V, Pengam S, Durand J, et al. Selective SIRPalpha blockade reverses tumor T cell exclusion and overcomes cancer immunotherapy resistance. *J Clin Invest*. Nov 2 2020;130(11):6109-6123. doi:10.1172/JCI135528
170. Song P, Guo L, Li W, Zhang F, Ying J, Gao S. Clinicopathologic Correlation With Expression of PD-L1 on Both Tumor Cells and Tumor-infiltrating Immune Cells in Patients With Non-Small Cell Lung Cancer. *J Immunother*. Jan 2019;42(1):23-28. doi:10.1097/CJI.0000000000000249

10 Acknowledgements

I would like to thank my mentor Prof. Dr. Mathias Heikenwälder, for giving me the opportunity to become a part of his science. Thank you, Mathias, for bringing together great professionals who are also brilliant people, and for creating this stunning scientific environment. I have truly enjoyed these years working together and I would like to deeply thank you for always keeping up your enthusiasm and your passion for our work. Thank you for always seeing the bright and positive side of my data and dealing with my self-criticism, for challenging me and making me realize how much I developed during these years.

I would also like to thank my examiner and TAC member, Prof. Dr. Peter Angel, for his time and valuable feedback during our discussions. Thank you to my additional TAC members, Prof. Dr. med. Michael Platten and Prof. Dr. Kai Breuhahn, for their suggestions and kind support to this project. To my PhD examiners, Prof. Dr. Ralf Bartenschlager and Dr. Guoliang Cui, my grateful thanks for your support and time.

Thanks also to my IDH1 collaborators in Boston, Nabeel Bardeesy, Lei Shi and Meng-Ju Wu - thank you for sharing your expertise with me so kindly, I greatly appreciate your time and help. Thanks to Detian Yuan and team for their great help in this project. To Jesper B. Andersen, thank you Jesper for the enlightening chats that broadened my perspectives. Thanks to Jon and Francesca, for being always available to discuss science and life decisions.

Thanks to my colleagues who have helped me enormously during these years. Michaela and team, thank you for your patience, always kind help and efficient support. I want to thank Sandra, for all the fun, for never saying “no” and always give me a hand in my demanding experiments. To Ulli, thank you for your endless patience, especially when it comes to my obsession with my IDH1 mouse lines and the space in the Satellite Unit. To Danijela and Jenny, thanks to both of you for contributing in great extent to this work. To Anna-Lena, Flo and Tim, for contributing to keep the wheels turning.

To the founders of the Bellini coffee team, thanks María, for welcoming me into the lab and introducing me to the HTVi world, and Marta, for always having a kind smile. Mo, thanks for always being able to help and our hate/love looks. Neda, for life discussions and very nice laughs. To Jan, for always having time to discuss and solve my cloning suggesting the Kozak sequence. To

Suzanne, thank you for listening and our funny times in the Small lab. Suchira, I enjoyed very much our conversations, thank you for listening to me and for your advice, not only in science but also in life, when I needed it the most. To Pierluigi, thank you for the Bamboleo moment and our Small lab chats, for sharing the south European roots which become Germanized, and those jokes that make me laugh so much.

To the F180 PhD students, for being such a particular group of people that fit so good together. Thank you all for dealing with my after-6pm low-glucose mental breakdowns, my “50€ fees” and my “less talky-talky, more worky-worky”. Thank you for the continuous laughs and for our fruitful scientific and life discussions.

First, I would like to thank Jure, my young padawan, for your enthusiasm and jokes, your help and for keeping up with my push. Tabea, thanks for showing up even after careful consideration and my FACS-derived concerts. Charles, I hope you had fun with my particular humor and thanks for your time in proof-reading this story, I owe you 50€. Xin Li! thanks for our nice conversations that made some days lighter, I have truly missed you in the PhD office. Chaofan, thank you for your kindness and your continuous willingness to help. Phil, thank for your support to this thesis, and your always good mood, but please use n≥3, it´s the law! To Enrico, for being the grilling star of the lab, the Pizza organizer and allowing me to develop my Italian skills. Vikas, for greatly contributing to the good mood of the lab, you bring us joy. Thanks to the #1 Racatanga, Tobi, for being always available to help me with cloning, open to discuss my experiment ideas and ready to lose in our teasing battles. Jakob, JJ, you have been giving me anxiety since our shared first day, I know you will miss me -specially my FACS days- as much as I will miss you. Tania, hija, for becoming part of the pusher team, thanks for our talky-talky about the real important things in life.

Special thanks to the coolest row of the PhD office and dream team (1, 2, 3!)- I hope you are “pride” of me! Svenja, for understanding what I think just by looking at each other- with big laughs derived from it. Thank you for listening to me when I am stressed out, for your patience when I continuously forget my keys in the office and for laughing at my bad jokes.
Endless thanks to Jose, my lab buddy and friend. You have truly been a pillar to my PhD time, my daily laugh and companion during our long hours in the lab, and the highlight of most of these days. Se dice que “Qué peligrosa esa gente que te hace reír todo el tiempo, porque después no

están por un rato y como que se te apaga la vida un poco". Hijo, qué suerte compartir con alguien como tú esta experiencia de vida, sin ti no hubiera sido lo mismo.

To those friends who became family, gracias a la Espanish secta: Alber, Ali, Damian, Dani, Maria, Nuria y Paula. Por los cocidos, las croquetas, el equipo mudanza y los abrazos cuando se necesitan. Gracias por ser mi vía de escape, por estar ahí siempre y entenderme como lo hacéis. Amigues, qué suerte formar un grupo tan especial con los que me siento en casa, y compartir estos años tan intensos llenos de momentazos para la memoria de futuros PIs y jefazos- os llevo conmigo.

A mis amigos de siempre, Alba, Marta, Rocío y Xicu, porque aunque pase el tiempo, nosotros seguimos siendo los mismos.

To my best collaborator in science and in life, thank you Domi for being by my side. For your big contribution to my scientific work, for your patience with my lab-life rhythm, but most importantly for your daily love- you have been my rock during this time.

A mi familia, por acompañarme siempre y apoyarme en todas mis aventuras. Por esta década de reencuentros y despedidas entre lágrimas, que cada vez cuestan más. Gracias a mis padres, Marisol y Cundi, por vuestro esfuerzo y trabajo constante, por dame todas las oportunidades y permitirme llegar hasta aquí. A mi hermana Celia, gracias tata por demostrarnos que la vida hay que pelearla siempre, y que tú eres la más valiente. Por convertirte en la persona brillante que eres, somos tus fans número uno, te quiero. A ti mamá, gracias por llevarme siempre de la mano y no soltarme nunca.